Mapping Arctic Surface Water Dynamics from Space

by

Eric Levenson

A dissertation accepted and approved in partial fulfillment of the

requirements for the degree of

Doctor of Philosophy

in Geography

Dissertation Committee:

Dr. Sarah Cooley, Chair

Dr. Mark Fonstad, Core Member

Dr. John Christian, Core Member

Dr. Jonathan Ryan, Core Member

Dr. Leif Karlstrom, Institutional Representative

University of Oregon

Winter 2026

© 2026 Eric Levenson
This work is licensed under a Creative
Commons Attribution License

DISSERTATION ABSTRACT

Eric Levenson

Doctor of Philosophy in Geography

Title: Mapping Arctic Surface Water Dynamics from Space

Geography is concerned with the changing spatial organization and material character of the Earth's surface. This perspective is fundamental to physical hydrology, which aims to understand the occurrence, distribution, and movement of water. Satellite remote sensing has emerged as a critical tool for geographers and hydrologists seeking an understanding of basic hydrologic questions, particularly in remote regions such as the Arctic where water is abundant across the landscape but observations are sparse. In this work, we aim to advance our capabilities to monitor surface water dynamics in the Arctic region and use these approaches to address fundamental questions about Arctic hydrology.

In Chapter II we produce a new state-of-the-art map of lakes and ponds for the state of Alaska. This dataset, termed the Alaska Lake and Pond Dataset (ALPOD) provides a spatially explicit record of the advance and retreat of nearly 1 million water bodies. We use this unique source of information to investigate how lake evolution responds to permafrost thaw. Specifically, we identify that as permafrost thaws, the trajectory of lake development differs according to the particular history of that lake's setting. Specifically, we find that the standard model of lake response to permafrost thaw (expansion followed by drainage) is modified by glacial history. In previously glaciated landscapes, lakes are much more resistant to permafrost thaw and can even exhibit the opposite pattern suggested by the established literature. This demonstrates a core concept of geography as stated by Dr. Alec Murphy: *where* something happens (e.g., permafrost thaw) influences what follows (e.g., lake drainage, expansion, or stability). These findings are uniquely enabled by technological advances in satellite remote sensing and data science. Specifically, the collection of frequent high-resolution imagery, cloud computing, and deep learning algorithms allow us to capture lake distribution in unprecedented detail.

In Chapter III, we expand this approach by measuring lake area weekly across the entire Arctic. By doing so over nine years (2017-2025), we identify remarkable seasonal changes to lakes that were previously only quantified in individual years or over a very small fraction of the region. Through this effort, we see event-scale processes such as catastrophic lake drainage, as well as gradual fine-scale dynamics like lake expansion that indicate significant environmental change such as melting ground ice.

Finally, in Chapter IV, we enter a new era in hydrology remote sensing by incorporating measurements in the vertical dimension. The Surface Water and Ocean Topography (SWOT) satellite can have a potentially transformative impact on our understanding of Arctic environmental change; however, its data is in its infancy and several known issues must be addressed. Therefore, we take our attention to the contiguous United States where we conduct a benchmarking analysis of SWOT capabilities for monitoring water storage change in lakes. We identify key solutions to data quality issues, and significantly improve performance by harmonizing SWOT data with our previous methods for mapping lake area. This effort directly improves our ability to describe the occurrence, distribution, and movement of water in the Arctic.

This dissertation includes previously published and unpublished co-authored material.

ACKNOWLEDGMENTS

I would like to thank my entire committee, and specifically Sarah Cooley for the mentorship throughout my PhD and the bravery to bring me on as her first student. I would also like to thank my parents, Dana and Shaula Levenson, for bringing me outside to experience the world and for fueling my curiosity about anything and everything. I also owe thanks to Mark Fonstad and Patricia McDowell for introducing me to research and encouraging me to pursue a PhD, as well as the rest of the Oregon Geography Department for providing the perspective and skills that define my approach as a scientist. This would not have been possible without the financial support from the NASA FINESST program (Award #80NSSC23K1556) and NASA New Investigator Program (Award #80NSSC21K0920). I am grateful for so many rivers, mountains, stretches of coastline, and even a few lakes for inspiring questions worth pursuing. The list of people who have helped me get here is far too long, but here are a few of those names: Nathaniel Klema, Jamie Wright, John Ditmars, Brooke Hunter, Kira Tenney, Jim Snyder, Anna and Jacob Levenson, Andrew Mullen, Elizabeth Webb, Ian Van Dusen, Addy Pletcher, Austin Hart, Geraldine Walker, and Johnny Ryan. Lastly, thank you to my wife Katie, my daughter Lucy, and our dog Wally for giving me patience, love, support, and an incredible sense of purpose.

DEDICATION

For Katie, Lucy, Wally, and my grandfather Richard Balomenos.

TABLE OF CONTENTS

Mapping Arctic Surface Water Dynamics from Space 1

DISSERTATION ABSTRACT 3

ACKNOWLEDGMENTS 5

DEDICATION 6

LIST OF TABLES 14

CHAPTER I 16

INTRODUCTION 16

References 22

CHAPTER II 25

GLACIAL HISTORY MODIFIES PERMAFROST CONTROLS ON THE DISTRIBUTION OF LAKES AND PONDS 25

1. Introduction 25

2. Materials and Methods 27

2.1 Creation of the ALPOD Dataset 27

2.2 Lake Size Distribution Power-Laws 28

2.3 Statistical Analysis of Lake Distribution across Permafrost Zones 29

2.4 Estimating Future Changes in Lake Area Caused by Permafrost Thaw 29

3. Results 30

3.1 Spatial Patterns in Lake and Pond Distribution 30

3.2 Geomorphic Controls on Lake and Permafrost Distribution 32

4. Discussion 34

4.1 Contextualizing Diverging Lake Area Trends 34

4.2 Implications for Future Lake Area Change 35

5. Conclusions and Bridge 37

References 38

CHAPTER III 45

TRACKING SEASONAL TO INTERANNUAL CHANGES TO PAN-ARCTIC LAKE AREA 45

1. Introduction 45

2. Study Area 47

3. Methods 47

3.1. Data 47

3.2. Lake Water Area Time Series 48

3.3 Ice Tracking and Observation Filtering 49

3.4. Spatial Variability Analysis 50

3.5. Interannual Variability Analysis 51

4. Results 52
4.1. Spatial Patterns 53
4.2. Interannual Lake Area Trends 56
4.3 Lake Extent Responses to Earlier Snowmelt 60
5. Discussion 61
6. Conclusion and Bridge 63
References 64
CHAPTER IV 70
ASSESSING SWOT CAPABILITIES AND LIMITATIONS FOR WATER STORAGE MONITORING IN LAKES 70
1. Introduction 70
2. Methods 72
2.2 Satellite Data 72
2.3 Measurement Error Calculations 74
2.4 SWOT Data Filtering 74
2.5 Water Storage Calculations and Evaluation 75
2.6 Water Storage Uncertainty Decomposition 78
3. Results 79
3.1 Measurement Frequency and Accuracy 79
3.2. SWOT Water Storage Variability Detection 82
3.3 Water Storage Uncertainty Reduction 84
4. Discussion 86
4.1. Contextualizing SWOT Water Storage Monitoring Performance 87
4.2. SWOT's Temporal Sampling 88
4.3. Future Enhancements 90
5. Conclusion 92
References 92
APPENDIX 97
APPENDIX A – CHAPTER II SUPPORTING INFORMATION 97
Text A1. ALPOD Dataset Construction 97
1.1 Motivation and Characteristics of ALPOD 97
1.2 Overarching ALPOD Dataset Engineering Approach 97
1.3 Sentinel-2 Imagery 98
1.4 Maximum Lake Extent Mask Production 98
1.5 Water Classification in Google Earth Engine 99
1.5 Postprocessing and Vectorization 100
1.6 Uncertainty Assessment 100
Text A2. Spatial analysis 101
APPENDIX B – CHAPTER III SUPPORTING INFORMATION 111
APPENDIX C – CHAPTER IV SUPPORTING INFORMATION 117

LIST OF FIGURES

Figure Page

2.1. Maps of ALPOD lakes. Panels (a-d) show ALPOD lake statistics: (a) lake fraction, (b) average lake size within each watershed, (c) lake density, and (d) total shoreline distance. Panel (e) shows the open water occurrence image and polygon boundaries for individual lakes, and (f) displays a detailed example of the vector within the Little Black River floodplain near the Yukon Flats. 31

2.2. Landscape controls on lake distribution. (a) Permafrost extent across Alaska and glacial coverage during the Last Glacial Maximum. Substrate texture is shown in Figure A5. (b) A comparison of lake fractions in watersheds binned by glacial history and substrate texture. The remaining terrain classes are displayed in Figure A7. Lake fraction increases with permafrost extent in unglaciated watersheds with fine geologic substrate ($p < 0.0001$), whereas lake fraction decreases with permafrost extent in postglacial watersheds with coarse substrate ($p < 0.0001$). (c) Comparing lake density (number of lakes per 100 km2) in watersheds binned by substrate texture and permafrost extent. Lake densities are higher in fine substrate and increase with permafrost class (p-value < 0.0001). Watersheds underlain by coarse substrate exhibit lower overall lake density and a negative correlation between permafrost extent and lake density (p-value < 0.0001). (d) Size distribution of ALPOD lakes. 33

2.3. Schematic comparing permafrost controls on lake fraction across physiographic settings. Each panel displays the oblique view of topography and ALPOD lakes from a watershed in our study that represents distinct glacial and permafrost classes. The inset panel shows the number of study sites from Webb and Liljedahl (2023) that exhibited decreasing, increasing, or insignificant decadal-scale lake area trends within the corresponding physiographic settings. The subsurface distribution of permafrost and seasonally freezing active layer are generated to illustrate permafrost hydrology mechanisms. 36

2.4. Estimated lake area loss based on our space-for-time substitution and projected permafrost thaw under RCP 8.5. (a) displays uniform predictions extrapolating negative correlations between lake area and permafrost extent in unglaciated-fine substrate watersheds to the entire study site (b) shows predictions constrained based on physiographic setting. The stable lake area in Northern Alaska reflects minimal projected permafrost thaw in this region (Figure A9). 37

3.1. Example of our water classification in the North Siberian Lowland (67.6° N, 146.5° E) for (a) an early season Sentinel-2 image with a measured lake ice fraction of 43% for the entire basin (not fully pictured), and (b) a mid-summer image. Both images show false color composites to emphasize the contrast between water, ice, and vegetation. Panel a demonstrates how ice and water are both counted as lake area, as well as the importance of including ice-affected dates to understand Arctic lake behavior. The pictured ephemeral lake, measuring an area of 390 ha, fills and drains annually. 50

3.2. Spatiotemporal patterns of pan-Arctic seasonal lake area fluctuations averaged across 2017-2025. 53

3.3. Lake area summary statistics and their spatial distribution. Visualizations and statistics are limited to 44,324 basins meeting analysis criteria. 54

3.4. Results from the unsupervised k-means clustering of baseline seasonal lake area progressions. Time series (a-c) show the center of clusters' lake area anomalies. The names for each cluster are interpretations of the dominant hydrologic processes for each cluster based on the time series progressions and their spatial distribution (d). 56

3.5. Example time series (a) and visual evidence (b) and (c) of lake drainage from the Yamal Peninsula, Russia. Images (b) and (c) display basin subsets to highlight the lake drainage event driving the negative lake area trend. 58

3.6. Diverging lake area trends (a-b) observed under similar climate constraints in thermokarst terrain within the Lena River watershed (c). 59

3.7. Lake area responses to snowmelt timing anomalies for (a) all basins with significant snowmelt timing variability and sufficient observational coverage. The data are then stratified into basins with (b) positive and (c) negative correlations between snowmelt timing and maximum lake area. 61

3.8. Example of 'seasonal drift' through a comparison of a basin's lake area progression (a) and seasonal distribution (b) following the 2021 early (negative) snowmelt timing anomaly and the 2018 late (positive) snowmelt timing anomaly. 63

4.1. Benchmark dataset. (a) Lake size distribution from the SWOT Prior Lake Database (PLD). (b) Distribution of data type available from in situ gauge data. (c) Map of lake and reservoir in situ gauge sites. 73

4.2. Example gauge and WSE anomaly time series using the idealized filter. The discrete evaluation framework is displayed in the top row, and the gap-filled, continuous evaluation is visualized in the bottom row with time-varying uncertainty shown in gray. The lakes show a left-to-right progression of

decreasing NSE scores to demonstrate the influence of a lake's magnitude and frequency of water level fluctuations on the signal-to-noise ratio of SWOT storage anomaly time series. 77

4.3. Idealized frequency and accuracy of SWOT WSE and WSA measurements. (a) CDF of absolute WSE errors for all ice-free SWOT observations, the idealized subset (i.e., observations meeting science accuracy requirements), and interpolated WSE errors. (b) histograms comparing the full distribution vs. idealized subset of signed WSE errors. (c) CDF of WSA absolute errors. (d) histograms comparing the full vs. idealized subset of signed WSA errors. (e) histogram of sampling gap between observations meeting science accuracy requirements. (f) Tradeoff between temporal resolution and WSE error tolerance. 79

4.4. Comparison of WSE error metrics for functional filters. (a-d) show respective WSE error metrics. (e-f) report filter classification performance in identifying WSE measurements passing the idealized filter (absolute error less than 28.3 cm). (g) Temporal resolution of filtered observations. (h) NSE of WSE anomalies, with minimum values truncated for visualization. 81

4.5. SWOT estimates of water storage variability across randomly sampled time series intervals. (a) Heatmap of the SWOT estimated water storage range expressed as a percentage of gauge measured water storage range, as a function of WSE range and time interval length. (b) Percent of the storage range detected by SWOT over varying time scales. (c) Percent of the storage range detected by SWOT as a function of actual WSE variability for samples with at least two SWOT observations. Y-axis is truncated to highlight the 100% threshold between over and underestimated storage variability. 83

4.6. SWOT water storage anomaly estimations in 198 study lakes. (a) and (b) compare idealized and functional (adaptive) filters' RMSE and NSE for water storage anomaly estimates. The daily resolution (interpolated SWOT measurements) are also included. RMSE is expressed as a percentage of the variable water storage. (c) map of the NSE values in lakes and reservoirs using the functional filter and daily (gap-filled) estimates. 84

4.7. The total observed RMSE for each model's functional water storage estimates expressed as a percentage of variable water storage. The errors are decomposed into the relative uncertainty contributions from WSE and WSA measurement errors, data filtering errors, and sampling gaps based on our uncertainty propagation. 85

4.8. Example AE relationships and water storage time series for six lakes and reservoirs in our benchmark dataset. (a-e) show time series for water year 2025 and (f) highlights a six-week period in spring 2025. Each of the four

storage models are presented in comparison to gauge water storage anomalies. Both the SWOTS2 and S2 models are based on the SWOT-S2 (purple) AE curves. 89

A1. Methodological approach to constructing the ALPOD dataset. 102

A2. Dataset construction progression starting with the U-Net predictions. Manual edits to the U-Net outputs produce the maximum possible lake extent mask (upper right). The lower left panel shows the output of the GEE processing that classifies open water in every available image within the maximum lake mask. Lastly, the final lake occurrence image is produced by applying a watershed segmentation algorithm to the GEE outputs. Note the areas within the maximum possible lake extent mask (green) that are excluded from the final lake occurrence dataset. These areas had low open-water occurrence values and were filtered by the watershed segmentation post-processing algorithm. 102

A3. Example of the area measured to calculate errors of omission. 103

A4. Visual comparison of ALPOD lake and ponds and the NHD water bodies. ALPOD boundaries are the result of open water occurrence for images across 6 ice-free seasons, whereas NHD boundaries are from static imagery sources. The timing of the acquisition of these images varies across Alaska, ranging from 2001-2023 and including some ice-covered dates. 104

A5. The map of substrate texture across AK based on Jorgsensen et al., 2008. Coarse substrate is from their 'rocky' classification, and fine substrate is a combination of sandy and silty textures. 105

A6. Lake fraction of watersheds differentiated by permafrost class. 105

A7. Comparison of the relationship between lake fraction and permafrost extent within distinct physiographic settings. 107

A8. Same comparison as Figure A7, but for low-elevation watersheds (<300 m). 108

A9. Projected permafrost coverage by Karjalainen et al., 2019 for RCP 8.5. RCPS 2.6 and 4.5 show very similar patterns but with slightly reduced permafrost in central AK. 110

A10. Interannual trends for basins that meet analysis requirements. Orange indicates declining lake area, while purple indicates increasing lake area. Gray shows basins without significant trends. 112

A11. Example time series of a previously documented 2018 lake drainage event on Seward Peninsula, AK (Nitze et al., 2020). 112

A12. Example time series and imagery of a drained lake basin and nearby ephemeral lakes that can fill and drain seasonally. Winter precipitation values are calculated from ERA5 reanalysis data. 113

A13. Boxplot comparing the distribution of permafrost extent of basins with significantly increasing or decreasing trends. According to our Mann-Whitney U-Test, mean permafrost extent of decreasing trends is lower than the mean permafrost extent of increasing trends ($p < 0.001$). 113

A13. Histograms of WSE errors for each filter. 117

LIST OF TABLES

Table Page

4.1. Four models for calculating active water storage time series from SWOT and Sentinel-2. 76

4.2. Comparison of aggregated WSE errors and temporal resolution across filtering schemes. 80

4.3. Comparison of observed and predicted water storage anomaly errors across water storage model permutations. 86

A1. ALPOD uncertainty assessment results 103

A2: Ancillary datasets 104

A3. Basic lake statistics across our physiographic and permafrost classes. 106

A4. Lake statistics differentiated by permafrost class. 107

A5. Results of Cuzick's Tests for Trend between permafrost extent and lake fraction. The null hypothesis is that there is no significant trend in increasing or decreasing lake fraction across groups ordered by permafrost extent. 108

A6. Results of Cuzick's Tests for Trend between permafrost extent and lake fraction in low elevation watersheds (<300m). The null hypothesis is that there is no significant trend in increasing or decreasing lake fraction across groups ordered by permafrost extent. 109

A7. Results of Cuzick's Tests for Trend between permafrost extent and mean lake size. The null hypothesis is that there is no significant trend in increasing or decreasing mean lake size across groups ordered by permafrost extent. 'pf' refers to permafrost. 109

A8. Lake area time series summary statistics calculated for each individual basin. Overall metrics use the entire filtered nine-year time series. Annual metrics are calculated for individual years (2017-2025). Seasonal metrics are calculated as a basin's average of the annual statistics. 111

A9. Predictors and their coefficients for the LASSO regression modeling basins' lake seasonality index. 115

A10. Annual mean discharge measured at Pilot Station, Yukon River (USGS Site No. 15565447. OLS Linear Regression results show a significant increase in mean discharge over the study period (p-value = 0.016) 116

A11. WSA error metrics by sensor. 117

CHAPTER I
INTRODUCTION

Surface water is a dominant feature of the Arctic landscape (Pekel et al., 2016), and its dynamics reflect and affect the regional water, carbon, and energy cycles. In recent decades, the Arctic has warmed four times faster than the global average (Rantanen et al., 2022). These warming temperatures have led to larger freshwater fluxes between the Arctic's atmosphere, ocean, and land surface (Rawlins et al., 2010). Surface water responses to climate forcing also produce important climate feedbacks that can enhance or dampen further warming. For example, wetting and drying patterns within permafrost regions impact the energy balance as surface water dynamics constrain both greenhouse gas emissions to the atmosphere (Morrissey & Livingston, 1992; Watts et al., 2014) and the amount of solar radiation that is by absorbed the land surface (Webb et al., 2021). Freshwater discharge from Arctic watersheds also has an outsized impact on global climate processes through impacts on ocean circulation (Haine et al., 2015), carbon cycling (Shiklomanov et al., 2021), and sea ice (Yang et al., 2021). The surface water patterns that constrain these climate feedbacks reflect the integrated influence of amplified Arctic warming, an intensifying hydrologic cycle, and shifting hydrologic connectivity in permafrost zones.

The importance of surface water for understanding Arctic environmental change raises the fundamental question: What is the spatial and temporal variability in water storage across the Arctic, and what are the driving factors? Answering this basic question is complicated by the vast and remote landscape, as well as the highly dynamic nature of surface water in the Arctic. Researchers use hydrologic simulations and remote sensing to characterize the hydrologic cycle across the Arctic because a network of in situ gauges that can suitably monitor water storage and fluxes within individual water bodies remains infeasible. Remote sensing provides an essential tool for observing actual hydrologic changes and calibrating physically-based models; however, its contributions have largely focused on interannual changes to the average extent of large water bodies. Therefore, the distribution of smaller water bodies in the Arctic, fine-scale variability, and vertical surface water adjustments all remain as knowledge gaps.

Advances in spaceborne sensors, cloud computing, and computer vision models present opportunities to increase the spatiotemporal resolution of surface water observations across large extents and even observe vertical fluctuations in surface water. For example, CubeSats have provided more frequent high-resolution optical imagery, which has enabled analyses of lake phenology in specific areas of interest within the Arctic (Cooley et al., 2017, 2019; Mullen et al., 2023). Until recently, producing water maps across large regions with high spatiotemporal resolution was limited by computing resources. The development of cloud-based data repositories and computing environments such as Google Earth Engine (GEE) have significantly increased the data volumes that hydrologists can utilize in their analyses. Additionally, advances in computer vision models for tasks such as image classification and segmentation have improved the accuracy of basic remote sensing tasks such as water classification. Lastly, the recently launched Surface Water and Ocean Topography (SWOT) satellite is a radar interferometer designed to observe the water surface elevation (WSE) changes that characterize variations and discharge within main river channels, floodplains, and lakes globally (Biancamaria et al., 2016). Together, these improvements in remote sensing capabilities combine to produce unrealized opportunities to monitor Arctic surface water dynamics from space.

The primary goal of this work is to advance our understanding of surface water dynamics in northern high-latitudes and address the methodological obstacles to monitoring lakes from space. Water storage in Arctic lakes fluctuates across daily to interannual timescales, reflecting the integrated influence of the atmosphere, land surface, and humans on the hydrologic cycle. Extreme seasonality defines the behavior of these water bodies due to seasonal patterns of temperature, precipitation, and insolation. Variability in surface water storage offers insight into only half of most Arctic water bodies' annual activity because ice covers their surface during colder months. The timing of ice breakup and freeze-up is changing in response to warming (Bring et al., 2016), which influences ice-free surface water dynamics through processes such as ice-jam flooding in rivers (e.g., Goulding et al., 2009) and alterations to lake evaporation regimes (Prowse et al., 2011). Additionally, the spring freshet that originates with snow and ice melt provides a pulse of water that recharges lakes, rivers, and wetlands. In fact, melt processes have been shown to control streamflow patterns throughout the year in certain cases (e.g., Pan et al., 2021). The research questions addressed through this proposal are focused on the ice-free months

in the Arctic, however the resulting datasets can be used to assess the relative importance of melt-season processes and warm season meteorology on surface water dynamics.

Warming temperatures and an intensifying hydrologic cycle will surely impact the northern water balance, however, the question of whether the Arctic is becoming wetter or dryer is still outstanding. Characterizing changes to surface water storge will be critical to understanding the water balance response to climate change. Rivers and subsurface processes in permafrost regions can drive surface water variability through alterations to hydrologic connectivity. Permafrost responds to warming trends by decreasing in extent and thickness (Wu et al., 2010), while the more permeable active layer of soil increases in thickness (Bonnaventure & Lamoureux, 2013). Near-surface permafrost thaw increases surface water storage through the production of thermokarst terrain and surface subsidence (Wagner et al., 2018). Ponding and lake expansion following initial permafrost thaw has been widely reported (Smith et al., 2005; Walvoord & Kurylyk, 2016; Webb & Liljedahl, 2023). While increased surface water coverage presents a positive feedback that encourages further localized warming by reducing albedo (Webb et al., 2021), this relationship can eventually reach a threshold as continued thawing increases permeability and new hydrologic pathways allow subsurface drainage. Lake drainage in response to permafrost destabilization has been observed in northern Siberia (Smith et al., 2005), northwestern Alaska (Nitze et al., 2020), the western Alaska coastal plain (Jones et al., 2020), and the western Canadian Arctic (Marsh et al., 2009). The direction of overall lake surface area change varies significantly even within these specific study areas, and western Canada has even exhibited a significant decline in the number of lake drainage events since the 1950s (Marsh et al., 2009). The arrival of CubeSat technology has enabled analyses of sub-seasonal lake dynamics, which has demonstrated in select study sites that fine-scale intra-annual changes to small water bodies provide an important source of overall variability in addition to these longer-term trends driven by permafrost processes (Cooley et al., 2017, 2019; Mullen et al., 2023).

The research objectives in this dissertation reflect the recognition that specific gaps in our understanding of Arctic surface water hydrology can be addressed by leveraging recent and ongoing advances to satellite-based Earth observation capabilities, computing resources, and image processing techniques. The relevant developments include the proliferation of high

spatiotemporal resolution optical imagery from CubeSats, new high-resolution commercial SAR imagery, SWOT, cloud computing resources from GEE, and deep learning models for surface water identification. These technologies are at varying stages of development and adoption from the hydrology research community, which is reflected in the differences in scope of the following chapters.

In Chapter II, we demonstrate that permafrost controls on lake distribution are substantially modified by glacial history and geologic substrate texture. We present the new Alaska Lake and Pond Occurrence Data set (ALPOD), which maps nearly 1 million water bodies and their spatial variability at 10-meter resolution. Using ALPOD, we address key questions regarding the interactions among permafrost and lakes across Alaska. Conceptual models suggest that permafrost thaw causes lake area to briefly increase and then decline over time, representing a major shift in the landscape with consequences for ecosystems, water resources, and carbon cycling. The extent of lake drainage across the northern permafrost zone remains unclear, especially given recent studies that have found both increasing and decreasing lake area. Using ALPOD, we demonstrate that differences in glacial history and geology can explain many of the conflicting trends reported in these previous studies. We show that thawing permafrost tends to reduce lake area in regions without past glaciation. However, in regions shaped by glaciers, lake areas can slightly increase with permafrost thaw. We corroborate these spatial patterns by showing that most documented decadal-scale lake area decreases occurred in unglaciated study sites. These findings provide potential mechanisms to explain previous disagreements in lake area trends and help constrain predictions of surface water change under further warming. This work is previously published in *Geophysical Research Letters* with co-authors Dr. Sarah Cooley, Andrew Mullen, Dr. Jennifer Watts, and Dr Elizabeth Webb.

Chapter III expands the study scope to the pan-Arctic region and by documenting the temporal dimension of lake area variability at sub-seasonal to nearly decadal time scales. This represents the first ever study documenting seasonal lake area variability at the pan-Arctic scale with sufficient observation frequency to capture the timing and magnitude of intra-annual lake area change. We investigate why lake seasonality varies spatially across the region, suggesting that local hydrologic connectivity, human water management, permafrost, and river networks play a crucial role. We observe many regionally important interannual trends, including

catastrophic lake drainage, terrestrialization, thermokarst lake expansion, and seasonal lake filling and drainage. We also identify the dominant control of snowmelt timing on the timing of maximum lake area, which has cascading effects on time-sensitive phenological relationships and lake area into the Arctic summer. Collaborators for this work include Dr. Sarah Cooley and Dr. Elizabeth Webb.

Many hydrological processes and research questions are concerned with water volumes and rates, rather than measures of surface area. Thus far, estimates of water storage from space has been limited by the available sensors. Very coarse, regional scale variability in total terrestrial water storage has been analyzed based on gravity anomalies (Syed et al., 2008). Other researchers have combined water surface area with hypsometry to calculate storage changes in water bodies, such as reservoirs (e.g., Bhagwat et al., 2019), but this approach is generally limited by the resolution of digital elevation models. Lastly, satellite altimeters such as ICESat-2 have been used to monitor vertical changes to the water surface (Chen et al., 2022; Ryan et al., 2020), but its 90-day average repeat and profiler sampling scheme limits its utility for monitoring of water storage. The ability to monitor water surface elevation (WSE) would allow us to estimate water storage and better assess the mechanisms of lake area dynamics, such as differentiating between lake-level water storage decreases or vegetation infilling.

The SWOT mission is a potentially transformative source of information for the hydrology community to transition from water surface area to volumetric units. However, the data is in its infancy and requires robust calibration and validation before it can support hydrologic monitoring and scientific hypothesis testing. In Chapter IV, we assess SWOT's performance for monitoring relative water storage change in lakes by first building a benchmark dataset of 411 gauged water bodies across the United States, with over 21,000 paired SWOT, Sentinel-2 and gauge observations spanning 2+ years. Using this dataset, we evaluate the accuracy of SWOT LakeSP water surface elevation (WSE) and water surface area (WSA) measurements, quantify the tradeoff between data filtering approaches and temporal resolution, and identify key sources of uncertainty in relative water storage time series. We find that, on average, SWOT estimates relative water storage change with an RMSE of 7.4% of variable storage capacity (0.0016 km^3) and a median Nash-Sutcliffe Efficiency of 0.94, capturing 75% of seasonal and 84% of annual storage variability. SWOT achieves these results through with a

functional temporal resolution of 14 days per observation and a WSE measurement precision of 18 cm (MAE) given current filtering best practices; however, the underlying precision is much better (8 cm MAE). Removing outlier SWOT WSE measurements while retaining valid observations remains a significant challenge, suggesting future filtering advances could significantly improve SWOT performance. Aside from filtering, our uncertainty decomposition reveals that SWOT WSA measurements are the next largest contributor to storage uncertainty. We thus find that integrating Sentinel-2 WSA observations with SWOT WSE significantly improves water storage estimates. Overall, we find that SWOT reliably resolves storage fluctuations over seasonal to annual time scales with water level changes exceeding 20 cm, but short-term and small magnitude changes may be undetected due to sampling gaps or measurement noise. Our analysis confirms that SWOT fulfills its core hydrology objective to observe relative water storage change globally, while identifying data filtering and WSA mapping as priorities for continued improvement. This work was completed in collaboration with Dr. Sarah Cooley, Dr. Jida Wang, and Dr. Melanie Trudel. The findings in Chapter IV provide the prerequisite validation to incorporate SWOT altimetry data into Arctic hydrology research.

In total, Chapters II and II establish the capabilities and algorithms for applying Sentinel-2 data to Arctic lake mapping and monitoring. These also present novel findings about permafrost controls over lake evolution and interactions between intra- and interannual lake area variability. A central technological limitation of these works is that lake area is used as a proxy for water storage. In Chapter IV, we demonstrate that SWOT and Sentinel-2 can be integrated to monitor lake level, area, and storage change. Moving forward, this work will serve as a foundation for hydrologic monitoring in the northern high latitudes.

References

Biancamaria, S., Lettenmaier, D. P., & Pavelsky, T. M. (2016). The SWOT Mission and Its Capabilities for Land Hydrology. In A. Cazenave, N. Champollion, J. Benveniste, & J. Chen (Eds.), *Remote Sensing and Water Resources* (pp. 117–147). Springer International Publishing. https://doi.org/10.1007/978-3-319-32449-4_6

Bonnaventure, P. P., & Lamoureux, S. F. (2013). The active layer: A conceptual review of monitoring, modelling techniques and changes in a warming climate. *Progress in Physical Geography: Earth and Environment*, *37*(3), 352–376. https://doi.org/10.1177/0309133313478314

Bring, A., Fedorova, I., Dibike, Y., Hinzman, L., Mård, J., Mernild, S. H., Prowse, T., Semenova, O., Stuefer, S. L., & Woo, M.-K. (2016). Arctic terrestrial hydrology: A synthesis of processes, regional effects, and research challenges. *Journal of Geophysical Research: Biogeosciences*, *121*(3), 621–649. https://doi.org/10.1002/2015JG003131

Cooley, S. W., Smith, L. C., Ryan, J. C., Pitcher, L. H., & Pavelsky, T. M. (2019). Arctic-Boreal Lake Dynamics Revealed Using CubeSat Imagery. *Geophysical Research Letters*, *46*(4), 2111–2120. https://doi.org/10.1029/2018GL081584

Cooley, S. W., Smith, L. C., Stepan, L., & Mascaro, J. (2017). Tracking Dynamic Northern Surface Water Changes with High-Frequency Planet CubeSat Imagery. *Remote Sensing*, *9*(12), Article 12. https://doi.org/10.3390/rs9121306

Goulding, H. L., Prowse, T. D., & Bonsal, B. (2009). Hydroclimatic controls on the occurrence of break-up and ice-jam flooding in the Mackenzie Delta, NWT, Canada. *Journal of Hydrology*, *379*(3), 251–267. https://doi.org/10.1016/j.jhydrol.2009.10.006

Haine, T. W. N., Curry, B., Gerdes, R., Hansen, E., Karcher, M., Lee, C., Rudels, B., Spreen, G., de Steur, L., Stewart, K. D., & Woodgate, R. (2015). Arctic freshwater export: Status, mechanisms, and prospects. *Global and Planetary Change*, *125*, 13–35. https://doi.org/10.1016/j.gloplacha.2014.11.013

Jones, B. M., Arp, C. D., Grosse, G., Nitze, I., Lara, M. J., Whitman, M. S., Farquharson, L. M., Kanevskiy, M., Parsekian, A. D., Breen, A. L., Ohara, N., Rangel, R. C., & Hinkel, K. M. (2020). Identifying historical and future potential lake drainage events on the western Arctic coastal plain of Alaska. *Permafrost and Periglacial Processes*, *31*(1), 110–127. https://doi.org/10.1002/ppp.2038

Marsh, P., Russell, M., Pohl, S., Haywood, H., & Onclin, C. (2009). Changes in thaw lake drainage in the Western Canadian Arctic from 1950 to 2000. *Hydrological Processes*, *23*(1), 145–158. https://doi.org/10.1002/hyp.7179

Morrissey, L. A., & Livingston, G. P. (1992). Methane emissions from Alaska Arctic tundra: An assessment of local spatial variability. *Journal of Geophysical Research: Atmospheres*, *97*(D15), 16661–16670. https://doi.org/10.1029/92JD00063

Mullen, A. L., Watts, J. D., Rogers, B. M., Carroll, M. L., Elder, C. D., Noomah, J., Williams, Z., Caraballo-Vega, J. A., Bredder, A., Rickenbaugh, E., Levenson, E., Cooley, S. W., Hung, J. K. Y., Fiske, G., Potter, S., Yang, Y., Miller, C. E., Natali, S. M., Douglas, T. A., & Kyzivat, E. D. (2023). Using High-Resolution Satellite Imagery and Deep Learning to Track Dynamic Seasonality in Small Water Bodies. *Geophysical Research Letters*, *50*(7), e2022GL102327. https://doi.org/10.1029/2022GL102327

Nitze, I., Cooley, S. W., Duguay, C. R., Jones, B. M., & Grosse, G. (2020). The catastrophic thermokarst lake drainage events of 2018 in northwestern Alaska: Fast-forward into the future. *The Cryosphere*, *14*(12), 4279–4297. https://doi.org/10.5194/tc-14-4279-2020

Pan, C. G., Kirchner, P. B., Kimball, J. S., Du, J., & Rawlins, M. A. (2021). Snow Phenology and Hydrologic Timing in the Yukon River Basin, AK, USA. *Remote Sensing*, *13*(12), Article 12. https://doi.org/10.3390/rs13122284

Pekel, J.-F., Cottam, A., Gorelick, N., & Belward, A. S. (2016). High-resolution mapping of global surface water and its long-term changes. *Nature*, *540*(7633), Article 7633. https://doi.org/10.1038/nature20584

Prowse, T., Alfredsen, K., Beltaos, S., Bonsal, B. R., Bowden, W. B., Duguay, C. R., Korhola, A., McNamara, J., Vincent, W. F., Vuglinsky, V., Walter Anthony, K. M., & Weyhenmeyer, G. A. (2011). Effects of Changes in Arctic Lake and River Ice. *AMBIO*, *40*(1), 63–74. https://doi.org/10.1007/s13280-011-0217-6

Rantanen, M., Karpechko, A. Y., Lipponen, A., Nordling, K., Hyvärinen, O., Ruosteenoja, K., Vihma, T., & Laaksonen, A. (2022). The Arctic has warmed nearly four times faster than the globe since 1979. *Communications Earth & Environment*, *3*(1), Article 1. https://doi.org/10.1038/s43247-022-00498-3

Rawlins, M. A., Steele, M., Holland, M. M., Adam, J. C., Cherry, J. E., Francis, J. A., Groisman, P. Y., Hinzman, L. D., Huntington, T. G., Kane, D. L., Kimball, J. S., Kwok, R., Lammers, R. B., Lee, C. M., Lettenmaier, D. P., McDonald, K. C., Podest, E., Pundsack, J. W., Rudels, B., … Zhang, T. (2010). Analysis of the Arctic System for Freshwater Cycle Intensification: Observations and Expectations. *Journal of Climate*, *23*(21), 5715–5737. https://doi.org/10.1175/2010JCLI3421.1

Shiklomanov, A., Déry, S., Tretiakov, M., Yang, D., Magritsky, D., Georgiadi, A., & Tang, W. (2021). River Freshwater Flux to the Arctic Ocean. In D. Yang & D. L. Kane (Eds.), *Arctic Hydrology, Permafrost and Ecosystems* (pp. 703–738). Springer International Publishing. https://doi.org/10.1007/978-3-030-50930-9_24

Smith, L. C., Sheng, Y., MacDonald, GM., & Hinzman, L. D. (2005). Disappearing Arctic Lakes. *Science*, *308*.

Wagner, A. M., Lindsey, N. J., Dou, S., Gelvin, A., Saari, S., Williams, C., Ekblaw, I., Ulrich, C., Borglin, S., Morales, A., & Ajo-Franklin, J. (2018). Permafrost Degradation and Subsidence Observations during a Controlled Warming Experiment. *Scientific Reports*, *8*(1), Article 1. https://doi.org/10.1038/s41598-018-29292-y

Walvoord, M. A., & Kurylyk, B. L. (2016). Hydrologic Impacts of Thawing Permafrost—A Review. *Vadose Zone Journal*, *15*(6), vzj2016.01.0010. https://doi.org/10.2136/vzj2016.01.0010

Watts, J. D., Kimball, J. S., Bartsch, A., & McDonald, K. C. (2014). Surface water inundation in the boreal-Arctic: Potential impacts on regional methane emissions. *Environmental Research Letters*, *9*(7), 075001. https://doi.org/10.1088/1748-9326/9/7/075001

Webb, E. E., & Liljedahl, A. K. (2023). Diminishing lake area across the northern permafrost zone. *Nature Geoscience*, *16*(3), 202–209. https://doi.org/10.1038/s41561-023-01128-z

Webb, E. E., Loranty, M. M., & Lichstein, J. W. (2021). Surface water, vegetation, and fire as drivers of the terrestrial Arctic-boreal albedo feedback. *Environmental Research Letters*, *16*(8), 084046. https://doi.org/10.1088/1748-9326/ac14ea

Wu, Q., Zhang, T., & Liu, Y. (2010). Permafrost temperatures and thickness on the Qinghai-Tibet Plateau. *Global and Planetary Change*, *72*(1), 32–38. https://doi.org/10.1016/j.gloplacha.2010.03.001

Yang, D., Ge, S., Park, H., & Lammers, R. L. (2021). River Heat Flux into the Arctic Ocean. In D. Yang & D. L. Kane (Eds.), *Arctic Hydrology, Permafrost and Ecosystems* (pp. 739–761). Springer International Publishing. https://doi.org/10.1007/978-3-030-50930-9_25

CHAPTER II
GLACIAL HISTORY MODIFIES PERMAFROST CONTROLS ON THE DISTRIBUTION OF LAKES AND PONDS

From Levenson, E. S., Cooley, S., Mullen, A., Webb, E. E., & Watts, J. (2025). Glacial history modifies permafrost controls on the distribution of lakes and ponds. *Geophysical Research* Letters, 52(4), e2024GL112771.

1. Introduction

The Arctic is warming almost four times faster than the global average (Rantanen et al., 2022). This amplified warming is intensifying the regional water cycle (Rawlins et al., 2010) and thawing permafrost (Osterkamp & Romanovsky, 1999; V. Romanovsky et al., 2002; V. E. Romanovsky et al., 2010), which stores twice as much carbon as the atmosphere and ~50% of the Earth's belowground carbon (Hugelius et al., 2014; Tarnocai et al., 2009). The severity of the permafrost carbon feedback to climate change is determined by local geomorphic and hydrologic properties that regulate carbon decomposition and transport (Schuur et al., 2015). For example, the expansion of lakes caused by thermokarst erosion enhances methane emissions (Walter Anthony et al., 2016), river channel incision promotes carbon transport to the ocean (Koch et al., 2013; Wild et al., 2019), and soil saturation controls overall decomposition rates and emission partitioning between carbon dioxide and methane (Schädel et al., 2016; Treat et al., 2015). Our limited ability to observe permafrost degradation and carbon cycling is a central challenge to understanding Arctic-Boreal feedbacks to climate change.

Since lakes provide readily observable features of the landscape, previous studies have leveraged observations of lake dynamics to infer permafrost conditions (Smith et al., 2005) and scale carbon flux estimates (Kuhn et al., 2021; Olefeldt et al., 2021). Permafrost alters lake distribution and development through its effects on hydraulic conductivity, erosion, and vegetation dynamics. Reduced hydraulic conductivity within frozen ground modifies water storage and movement by limiting water infiltration and subsurface flow paths while increasing surface water storage (Velicogna et al., 2012) and transport (Walvoord et al., 2012; Walvoord & Striegl, 2007). In addition to these hydrologic impacts, permafrost also affects geomorphic

processes by limiting advective sediment transport (Douglas & Lamb, 2024; Lange & Ahrens, 1983) and facilitating thermokarst erosional processes such as surface subsidence and thermo-erosion (Godin et al., 2014). As a result, permafrost landscapes exhibit decreased drainage density (Del Vecchio et al., 2024) while historical and contemporary permafrost thaw emplaces characteristic landforms, including thermokarst lakes, retrogressive thaw slumps, and beaded streams (Arp et al., 2014; Farquharson et al., 2016; Grosse et al., 2013; Jones et al., 2011; Olefeldt et al., 2016; Swanson, 2019). Through these mechanisms, lake locations and evolution can reveal permafrost interactions with sediment, carbon, water, and thermal fluxes.

Both conceptual models and observations of lake evolution hypothesize that initial permafrost thaw leads to stable or expanding lakes, with sustained permafrost thaw resulting in draining, sedimentation, and/or vegetation encroachment (Jones et al., 2011; Riordan et al., 2006; Roach et al., 2011; Schuur et al., 2015; Smith et al., 2005; Walvoord & Kurylyk, 2016). However, observations of lake area trends have been inconsistent across the permafrost zone, with some studies showing increases in lake area and others documenting broad decadal-scale decreases in lake area (Christensen et al., 2004; Pastick et al., 2019; Webb & Liljedahl, 2023). The divergence between models and observations in certain sites complicates our understanding of permafrost degradation's effect on lake development and limits our ability to predict regional and future lake area trends. Given that the direction of temporal lake area trends varies geographically, the extent to which permafrost controls over lake distribution are dependent on local geomorphic conditions warrants further investigation. Whether geomorphic settings constrain permafrost-lake interactions remains unclear in part due to tradeoffs between the spatial resolution and spatial coverage of existing data sources. Previous analyses of decadal-scale lake evolution have either been focused solely within relatively uniform physiographic settings (Cooley et al., 2017, 2019; Jones et al., 2011; Mullen et al., 2023; Nitze et al., 2017, 2020; Smith et al., 2005) or studied large regions using coarse spatial resolution data (e.g., 500 m) that cannot separate the individual water bodies or ponds that are critical to permafrost hydrology processes and carbon cycling (Olefeldt et al., 2021; Watts et al., 2012; Webb et al., 2022).

Here we assess whether permafrost controls over lake distribution are mediated by glacial history and geologic substrate. Although unglaciated areas comprise only 29% of the Arctic

excluding Greenland (Batchelor et al., 2019), the vast majority of lake area change analyses in the permafrost zone have been conducted in unglaciated landscapes (Webb et al., 2023). The topographic effects of glacial retreat could limit the development of new drainage networks that contribute to lake area drainage. Similarly, coarse geologic substrate such as bedrock may dampen the effects of permafrost on erosion and permeability.

For this analysis, we present a new dataset of lakes and ponds larger than 0.001 km2 for the state of Alaska from 10 m spatial and near-daily temporal resolution Sentinel-2 imagery, which we term the Alaska Lake and Pond Occurrence Dataset (ALPOD). To better understand the effect of permafrost thaw on lake evolution, we quantify the spatial relationship between the distribution of permafrost and ALPOD water bodies. Alaska is entirely within the historic permafrost zone (Vandenberghe et al., 2014), so the current permafrost extent can be interpreted as the degree of permafrost thaw since the last permafrost maximum. Given that lake area has declined in response to permafrost thaw during the Holocene (Smith et al., 2005; Webb & Liljedahl, 2023), we hypothesize that the modern spatial distribution of lake area is related to current-day permafrost extent (i.e., historic permafrost thaw), with lower permafrost extent characterized by smaller lake fractions. By testing the significance of the relationship between permafrost extent and lake distribution in regions differentiated by glacial history and surficial geology, we evaluate whether permafrost controls on lake distribution are restricted to specific physiographic settings. We then use these findings to investigate whether differences in physiographic setting can contextualize disagreements in observed lake area trends in previously published decadal-scale lake evolutions. Finally, we conclude by leveraging our results to constrain estimates of potential lake area change across Alaska caused by projected permafrost thaw.

2. Materials and Methods

2.1 Creation of the ALPOD Dataset

ALPOD was constructed using a novel combination of deep learning (Mullen et al., 2023), adaptive NDWI thresholding (Cooley et al., 2017, 2019), and cloud computing (Gorelick et al., 2017) to conduct a satellite-based lake and pond survey across the entire state of Alaska (~1.5 million km2), which contains an abundance of lakes, diverse permafrost conditions, glacial

histories, and depositional settings. We first produced a mask of the maximum potential lake inundation extent that excludes river channels and persistently dry areas. To do this, we accessed 1-2 Sentinel-2 images for every location in the study area, prioritizing cloud-free images captured near the seasonal maximum water extent based on visual inspection. Next, we predicted lake locations in these images using a U-Net lake identifier model (Mullen et al., 2023). The U-Net model is a convolutional neural network that represents features such as edges and frequencies across scales, which is advantageous for separating lakes from components of the landscape with similar reflectance properties, such as rivers. We buffered the predictions by 60 meters and manually edited the results. Within this maximum lake extent mask, we created an open water occurrence product for the 2016-2021 ice-free seasons by clipping every available Sentinel-2 image within the study period to the maximum lake extent mask and classifying water using an adaptive NDWI thresholding algorithm (Cooley et al., 2017). We combined these binary water images into a 10-meter resolution composite, with each pixel recording the percentage of observations classified as water. Using a watershed segmentation postprocessing algorithm, we ensured all pixels were associated with a water body (Figure A2).

Our uncertainty assessment showed that ALPOD's F1 score for classifying lakes and ponds larger than 0.001 km2 was 0.999 (see S1.6). Our analysis of the spatial patterns of lake abundance and size uses a 25% occurrence threshold (i.e., open water in at least 25% of observations) to include intermittently inundated depressions, as these may be useful for understanding the potential mechanisms explaining the distribution of lakes. Although the occurrence dataset includes ponds as small as 0.0001 km2, water bodies smaller than 0.001 km2 were more likely to be omitted or false positives. Therefore, we excluded water bodies smaller than 0.001 km2.

2.2 Lake Size Distribution Power-Laws

Using ALPOD, we first characterized Alaska's lake size distribution by following previous work developing theoretical and empirical expectations for the relationship between lake size and abundance (Cael & Seekell, 2016). Power laws are widely used to describe the Earth's skewed lake size distribution towards many small lakes and fewer large lakes (Cael & Seekell, 2016). We used the powerlaw software package (Alstott et al., 2014) to calculate the

power law function's tail exponent and minimum lake size threshold to compare ALPOD and global lake size distributions and to examine the effect of glacial history on the lake size distribution.

2.3 Statistical Analysis of Lake Distribution across Permafrost Zones

To investigate the relationship between lakes, landscape history, and permafrost extent, we intersected ALPOD with ancillary datasets to classify lakes based on glacial history (Batchelor et al., 2019), substrate texture (Jorgenson et al., 2008), and permafrost extent (Obu et al., 2019). We calculated lake fraction, density, and mean lake size for each terrain classification (Table A3). To test the differences in lake distribution across permafrost zones and terrain classes, we calculated lake fraction (percentage of area covered by open water), lake density (number of lakes per 100 km2), and mean lake size for 14,314 HUC12 watersheds from the National Hydrography Dataset (NHD) covering AK. We classified each watershed based on the above physiographic characteristics. We also masked current glaciers from the lake fraction and density calculations. For each combination of glacial history and substrate textures, we test the null hypothesis that lake fraction, size, and density exhibit similar means across different permafrost extent classes. The alternative hypothesis was that the mean lake fraction was greater in watersheds with more extensive permafrost. To test these hypotheses we used a Cuzick's test (Cuzick, 1985), which is a test for trend across ordered groups.

2.4 Estimating Future Changes in Lake Area Caused by Permafrost Thaw

Detecting the differences in mean lake fraction across distinct permafrost settings allowed us to utilize a space-for-time substitution to estimate changes to the total lake area in response to projected permafrost thaw. First, we identified the physiographic settings with significant relationships between permafrost and lake fraction based on Cuzick's tests. For these terrain classifications – defined as a unique combination of glacial history and substrate texture – we estimated the sensitivity of lake fraction to permafrost extent using a linear regression:

Equation 1: $$\beta_{1\ i,j} = (\text{mean lake area}_{(i,j)} - \beta_0\ )/\text{permafrost extent}_i$$

Where β_0 *= the overall mean lake area for that terrain classification; i = permafrost class; j = terrain classification; Permafrost extenti = the average percent permafrost coverage within each permafrost class, and mean lake areai is the average lake area for that permafrost class;* β_1 *= slope of the line of best fit between permafrost extent and mean lake area.*

Next, we utilized projected decrease in permafrost extent for 2061-2080 (Karjalainen et al., 2019) under RCPs 2.6, 4.5, and 8.5 to estimate the change in lake area for each watershed:

Equation 2: $$\Delta \text{ lake area} = \Delta \text{ permafrost extent} \times \beta_1 \times \text{current lake area}$$

For each RCP, we produced two lake area change estimates. The 'uniform' estimate applies the maximum observed lake sensitivity across the full study area. The 'constrained' estimate uses sensitivity values specific to each physiographic setting to calculate lake area change attributed to permafrost thaw.

3. Results

3.1 Spatial Patterns in Lake and Pond Distribution

ALPOD reveals surface water patterns with 10 m resolution at scales ranging from individual lakes to all of Alaska (Figure 2.1). After excluding water bodies less than 0.001 km2 in surface area, we mapped 802,667 water bodies at a 25% occurrence threshold (meaning water present at least 25% of the time) and 1,209,606 at a 75% occurrence threshold, reflecting increased connections between water bodies with expanded inundation extent (e.g., Figure 2.1f). Using the same thresholds, the total lake area ranges from 39,296 km2 (75% occurrence) to 48,536 km2 (25% occurrence), or 2.63% to 3.24% of the total land area across Alaska. Compared to the Alaskan lakes from the global Landsat-based Prior Lake Database (PLD) (Wang et al., 2023), ALPOD observes 584,281 more lakes and increases the statewide lake area fraction estimate from 2.69% to 3.24%, reflecting an 8,243 km2 increase in lake area. The USGS waterbody dataset (USGS, 2022.) estimates 50,347 km2 of waterbody area in AK, but a visual inspection suggests that this dataset includes more river channels and vegetated areas (Figure A4).

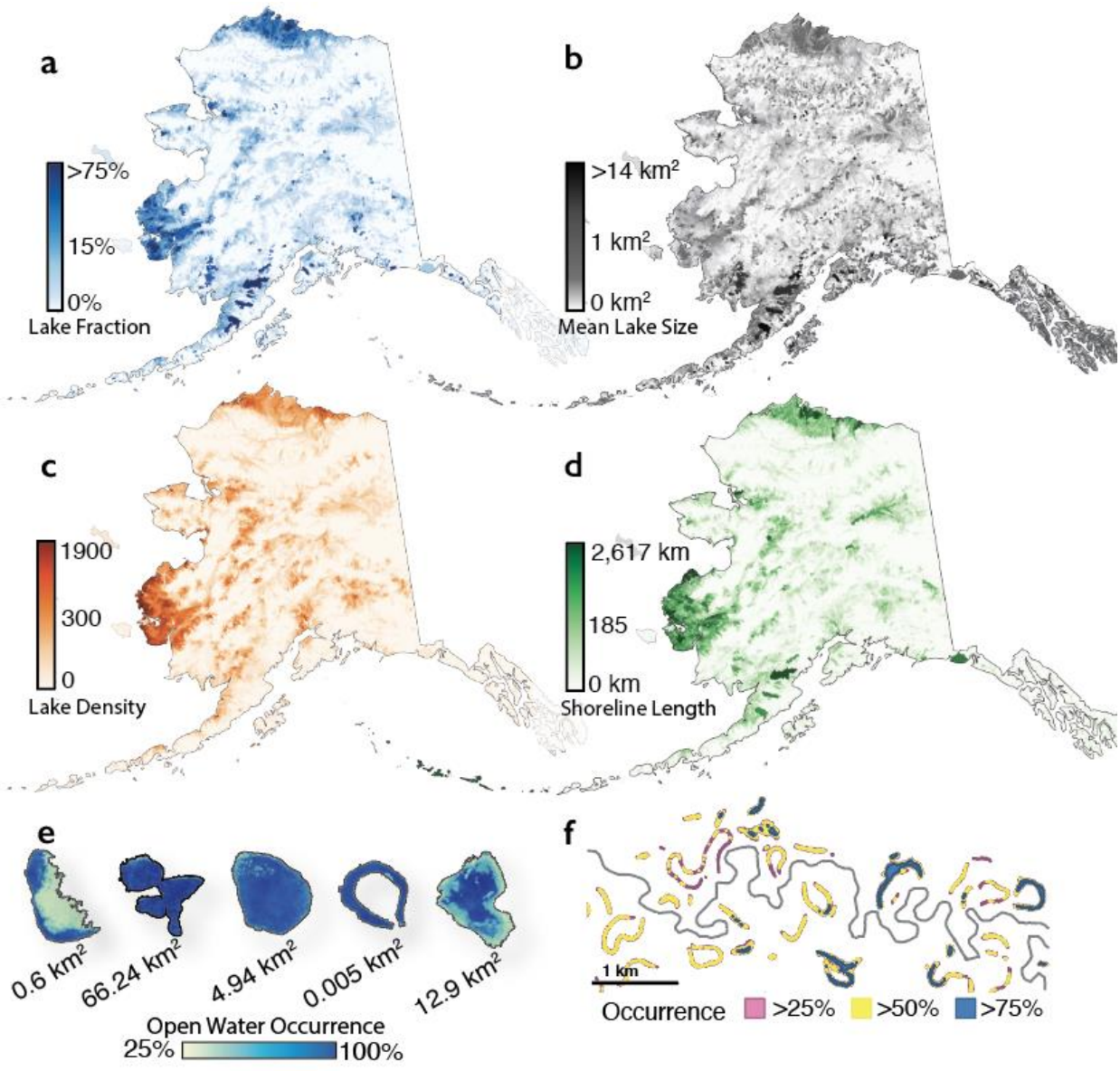

Figure 2.1: Maps of ALPOD lakes. Panels (a-d) show ALPOD lake statistics: (a) lake fraction, (b) average lake size within each watershed, (c) lake density, and (d) total shoreline distance. Panel (e) shows the open water occurrence image and polygon boundaries for individual lakes, and (f) displays a detailed example of the vector within the Little Black River floodplain near the Yukon Flats.

The overall size distribution of ALPOD lakes closely adheres to the global lake size distribution based on a power-law relationship between log-lake area and log-abundance.

Alaskan lakes are power-law distributed for lakes >1.01 km2, which is similar to the 1 km2 minimum threshold calculated for a global lake inventory (GLOWABO) (Cael & Seekell, 2016; Verpoorter et al., 2014). The tail exponents of the Alaska and global lake power-law distribution are also similar, at $\boldsymbol{\tau}$= 2.23 (ALPOD) and $\boldsymbol{\tau}$= 2.14 (GLOWABO). Lakes smaller than the 1.01 km2 threshold comprise the vast majority of lakes, but they are less abundant than expected should the entire ALPOD size distribution conform to a power-law relationship. Deviations from the overall power-law relationship underscore the importance of a lake census approach for describing the abundance of lakes and ponds rather than statistical estimations of small water bodies based on maps of the largest lakes. The median lake size is 0.005 km2, and 93.6% of lakes are smaller than 0.1 km2. Large lakes (>1 km2) contribute 55% of the total lake area despite only representing 0.006% of all water bodies. A spatial intersection between ALPOD and historical glacier coverage during the Last Glacial Maximum (LGM) and late Miocene (Mi6) eras demonstrates that postglacial processes shift the lake distribution towards fewer and larger lakes. Excluding currently glaciated areas, 43.9% of AK was previously glaciated, and these regions contain 34.3% of total lake area and only 18.9% of the lakes. A larger range of the lake size distribution for previously glaciated landscapes (Figure 2.2d) adheres to a power-law relationship (minimum threshold = 0.16 km2, $\boldsymbol{\tau}$ = 2.04), compared to unglaciated lake size distribution (minimum threshold = 1.99 km2, $\boldsymbol{\tau}$ = 2.42).

3.2 Geomorphic Controls on Lake and Permafrost Distribution

ALPOD's detail and high resolution allows us to test whether there is decreased lake area in regions with reduced permafrost extent, as previous studies hypothesize (Smith et al., 2005; Webb & Liljedahl, 2023). We find that the direction and significance of the relationship between permafrost class and lake distribution depends on the geomorphic setting (Figure 2.2, Table A3). Across Alaska, the average lake fraction does not significantly increase with more extensive permafrost; however, after differentiating by glacial history and geologic substrate texture, lake area significantly (and monotonically) increases with permafrost extent in unglaciated watersheds with fine substrate (Figure 2.2b; p-value < 0.0001). The positive relationship between permafrost extent and lake fraction in these unglaciated watersheds with fine substrate texture is significant across the entire study area and lowland landscapes (<300 m). This is the only

geomorphic setting that conforms to our hypothesized relationship between lake and permafrost distribution. The remainder of our terrain classes exhibit either no trend or an opposite (negative) trend between lake fraction and permafrost coverage in the case of postglacial-coarse substrate regions (Figure A7; Table A5).

We find that lake density is primarily influenced by substrate texture (Figure 2.2c). Lake density is significantly higher in fine substrate than coarse substrate, and in fine substrate, we see a statistically significant increase in the number of lakes with permafrost extent. The relationship between lake size and permafrost follows similar patterns to lake fraction, where mean lake size increases with permafrost extent in unglaciated watersheds and decreases with permafrost extent in postglacial settings (Table A7).

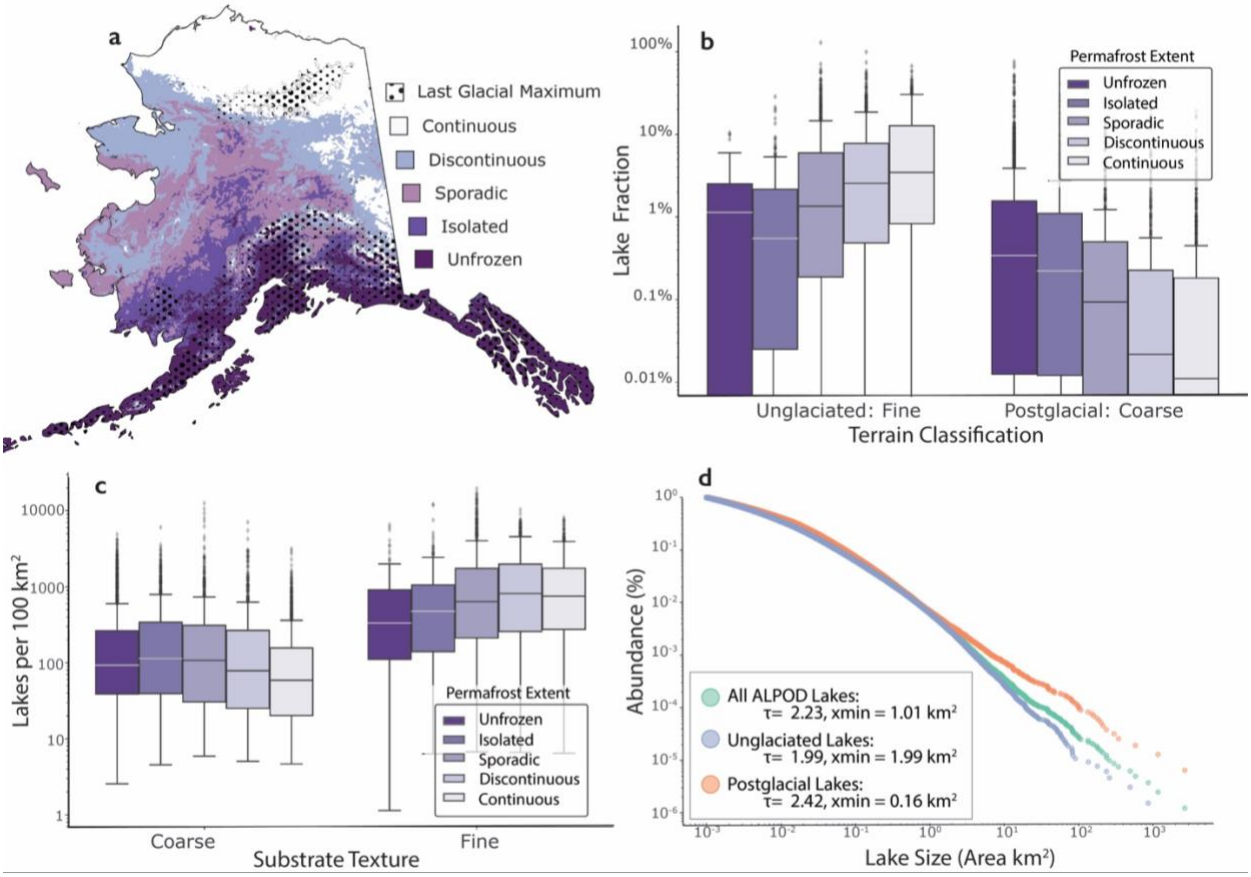

Figure 2.2: Landscape controls on lake distribution. (a) Permafrost extent across Alaska and glacial coverage during the Last Glacial Maximum. Substrate texture is shown in Figure A5. (b)

A comparison of lake fractions in watersheds binned by glacial history and substrate texture. The remaining terrain classes are displayed in Figure A7. Lake fraction increases with permafrost extent in unglaciated watersheds with fine geologic substrate ($p < 0.0001$), whereas lake fraction decreases with permafrost extent in postglacial watersheds with coarse substrate ($p < 0.0001$). (c) Comparing lake density (number of lakes per 100 km2) in watersheds binned by substrate texture and permafrost extent. Lake densities are higher in fine substrate and increase with permafrost class (p-value < 0.0001). Watersheds underlain by coarse substrate exhibit lower overall lake density and a negative correlation between permafrost extent and lake density (p-value < 0.0001). (d) Size distribution of ALPOD lakes.

4. Discussion

4.1 Contextualizing Diverging Lake Area Trends

Our findings demonstrate permafrost controls on lake evolution are mediated by the geomorphic setting produced by long-term landscape evolution processes. A recent meta-analysis of 139 studies tracking lake area change in the northern permafrost zone shows a broad decline in lake area in discontinuous permafrost and variable trends in the continuous permafrost zone (Webb & Liljedahl, 2023). By classifying these studies into unglaciated and postglacial locations, we find that the observed lake area declines that form the basis of our understanding of lake evolution in thawing permafrost are overwhelmingly from unglaciated sites such as Yedoma permafrost in Siberia and Alaska's North Slope (Webb & Liljedahl, 2023). In contrast, only 22% of study sites are located in previously glaciated areas, and these are much more likely to show lake area increases or no trend (Figure 2.3).

Based on these findings, we hypothesize that the processes responsible for thaw-induced lake area decline are only effective at modulating lake evolution within unglaciated, fine substrate regions because of their low relief, permeable and erodible substrate, and their capacity for increased drainage network density. Geomorphic mechanisms such as lateral breaching occur when permafrost thaw increases the rate of erosional processes, including advective sediment transport and surface subsidence, thus expanding lakes and drainage networks (Jones et al., 2011, 2022). In terrain susceptible to these erosional processes – such as lowland historic thermokarst, Eolian deposits, and Yedoma permafrost deposits – permafrost thaw increases lake connectivity

to channel networks through erosional processes, leading to lateral lake drainage and decreased lake fraction. Lateral drainage has been documented as a leading cause of surface water decline in areas such as Alaska's Seward Peninsula (Jones et al., 2011). In addition to lateral lake drainage, vegetation and sediment can fill shallow thermokarst lakes to reduce surface area (Lewkowicz & Way, 2019; Loiko et al., 2020), and increased substrate permeability can increase subsurface hydrologic connectivity and allow vertical lake drainage (Rangel et al., 2021; Wellman et al., 2013). Figure 2.3 illustrates potential mechanisms behind our empirical evidence that lake sensitivity to permafrost thaw is heterogeneous due to landscape history.

The relationship between permafrost and lake fraction we identify in postglacial settings is surprising due to its implication that lake area increases with permafrost thaw. One potential explanation is that permafrost has preserved relict glacial ground ice and delayed postglacial landscape evolution, which has been documented through the recent intensification of thaw-slumping in northwestern Canada caused by permafrost thaw exposing preserved late Pleistocene ground ice (Kokelj et al., 2017). The presence of permafrost could have delayed the formation of kettle lakes, which form in depressions caused by melting ice chunks buried by glacial sediment (Menzies, 2002). Another possible mechanism is that when permafrost is superimposed on rugged postglacial terrain, decreased infiltration erosion may cause water to runoff quickly through drainage networks that were established during glacial retreat. Overall, this finding highlights the need for detailed local analyses of lake evolution in postglacial regions to fully understand the effect of permafrost in these environments.

4.2 Implications for Future Lake Area Change

Our results show that projections of future permafrost thaw-driven lake area changes must consider physiographic heterogeneity. To demonstrate this effect, we used our findings to perform a space-for-time substitution to project potential lake area decreases caused by permafrost thaw (Figure 2.4). Constraining our calculations based on geomorphic setting reduces our estimate of lake area loss across Alaska from 710 km2 to 370 km2 under RCP2.6 and from 815 km2 to 419 km2 under RCP8.5. This analysis indicates that overlooking the importance of glacial history/substrate in projections of lake area change leads to significant overestimation of lake area decline associated with permafrost degradation. We note that this space-for-time

substitution is only meant to be an example of the implications of geomorphically-mediated lake sensitivity to permafrost thaw. These predictions do not include other factors influencing lake distribution, such as changes to water balance and human activities. However, this approach underscores how incorporating geomorphic variability can yield more realistic insights into future surface water dynamics in permafrost regions.

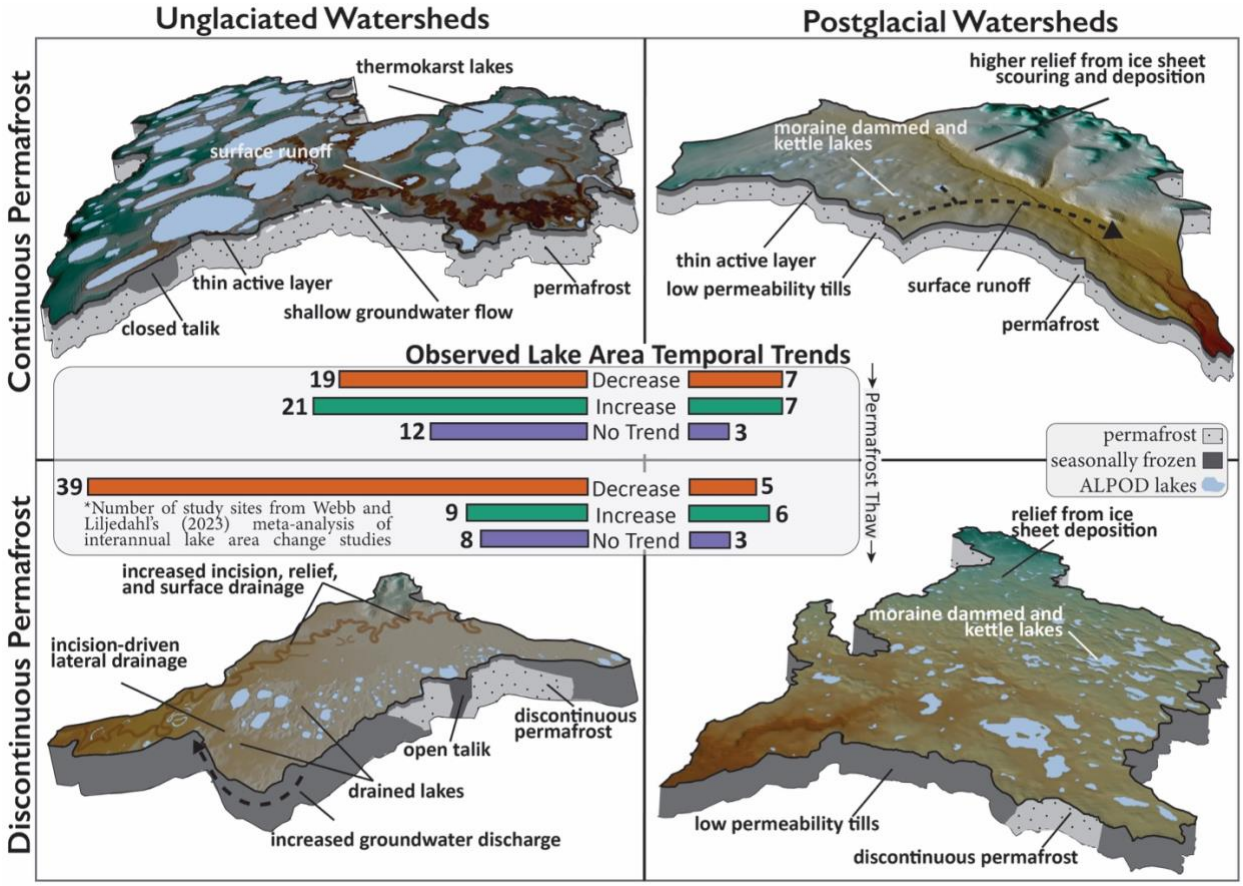

Figure 2.3: Schematic comparing permafrost controls on lake fraction across physiographic settings. Each panel displays the oblique view of topography and ALPOD lakes from a watershed in our study that represents distinct glacial and permafrost classes. The inset panel shows the number of study sites from Webb and Liljedahl (2023) that exhibited decreasing, increasing, or insignificant decadal-scale lake area trends within the corresponding physiographic settings. The subsurface distribution of permafrost and seasonally freezing active layer are generated to illustrate permafrost hydrology mechanisms.

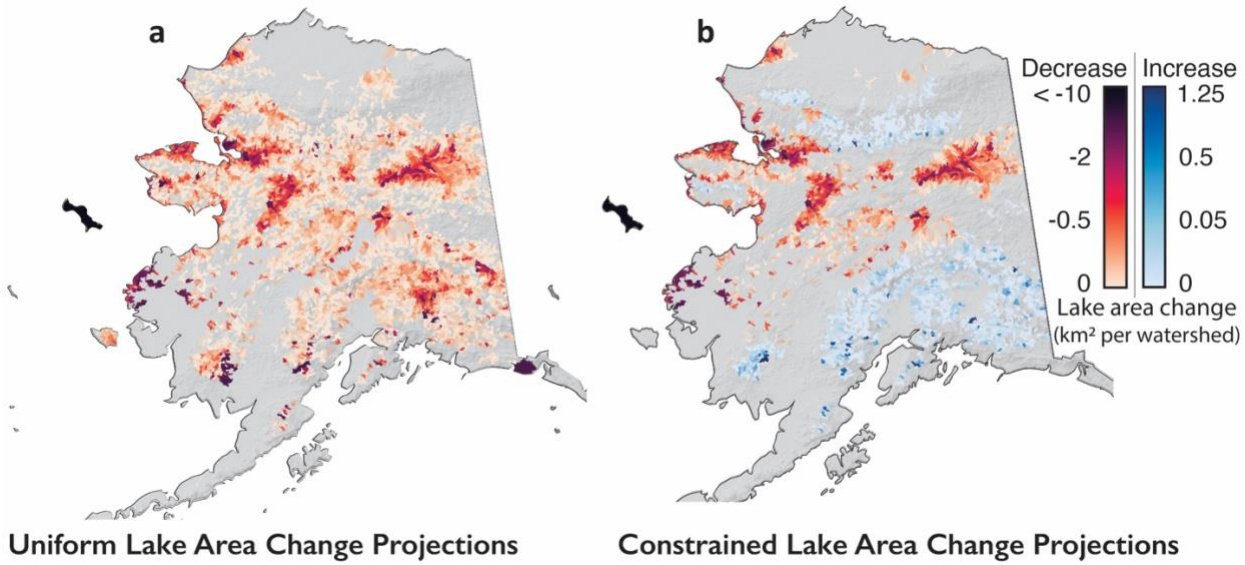

Figure 2.4: Estimated lake area loss based on our space-for-time substitution and projected permafrost thaw under RCP 8.5. (a) displays uniform predictions extrapolating negative correlations between lake area and permafrost extent in unglaciated-fine substrate watersheds to the entire study site (b) shows predictions constrained based on physiographic setting. The stable lake area in Northern Alaska reflects minimal projected permafrost thaw in this region (Figure A9).

5. Conclusions and Bridge

Here we show that lake and pond responses to permafrost degradation differ based on distinct glacial history and substrate textures, which is a critical insight for scaling observations of the hydrologic system, carbon cycling, and ecological disturbances from field studies to a regional scale. Diverging observations of the direction of decadal-scale trends can thus be largely explained by geomorphic setting, with decreasing trends found primarily in unglaciated areas. Our results also indicate that lake area may slightly increase with permafrost thaw in previously glaciated regions, although we suggest further investigation of potential mechanisms controlling this effect. These new insights emphasize that ecological systems' vulnerability to rapid warming will vary spatially across the Arctic according to landscape characteristics such as topography and geology. Overall, our results demonstrate that permafrost-driven lake area declines are highly sensitive to physiographic setting and thus research into permafrost-lake feedbacks must

consider local geomorphic conditions. Finally, these findings are only one application of our new Alaska lake dataset (ALPOD) and we expect its high resolution and detail to be valuable for further research on ecology, lake evolution, and carbon cycling. In Chapter III, we expand our study scope from Alaska to the pan-Arctic region and use our Sentinel-2 lake area mapping methodology to explicitly track temporal changes to lake area in the permafrost zone.

References

Alstott, J., Bullmore, E., & Plenz, D. (2014). powerlaw: A Python Package for Analysis of Heavy-Tailed Distributions. *PLoS ONE*, *9*(1), e85777. https://doi.org/10.1371/journal.pone.0085777

Arp, C. D., Whitman, M. S., Jones, B. M., Grosse, G., Gaglioti, B. V., & Heim, K. C. (2014). *Beaded streams of Arctic permafrost landscapes*. https://doi.org/10.5194/bgd-11-11391-2014

Batchelor, C. L., Margold, M., Krapp, M., Murton, D. K., Dalton, A. S., Gibbard, P. L., Stokes, C. R., Murton, J. B., & Manica, A. (2019). The configuration of Northern Hemisphere ice sheets through the Quaternary. *Nature Communications*, *10*(1), 3713. https://doi.org/10.1038/s41467-019-11601-2

Cael, B. B., & Seekell, D. A. (2016). The size-distribution of Earth's lakes. *Scientific Reports*, *6*(1), 29633. https://doi.org/10.1038/srep29633

Christensen, T. R., Johansson, T., Åkerman, H. J., Mastepanov, M., Malmer, N., Friborg, T., Crill, P., & Svensson, B. H. (2004). Thawing sub-arctic permafrost: Effects on vegetation and methane emissions. *Geophysical Research Letters*, *31*(4), 2003GL018680. https://doi.org/10.1029/2003GL018680

Cooley, S. W., Smith, L. C., Ryan, J. C., Pitcher, L. H., & Pavelsky, T. M. (2019). Arctic-Boreal Lake Dynamics Revealed Using CubeSat Imagery. *Geophysical Research Letters*, *46*(4), 2111–2120. https://doi.org/10.1029/2018GL081584

Cooley, S. W., Smith, L. C., Stepan, L., & Mascaro, J. (2017). Tracking Dynamic Northern Surface Water Changes with High-Frequency Planet CubeSat Imagery. *Remote Sensing*, *9*(12), Article 12. https://doi.org/10.3390/rs9121306

Cuzick, J. (1985). A wilcoxon-type test for trend. *Statistics in Medicine*, *4*(1), 87–90. https://doi.org/10.1002/sim.4780040112.

Del Vecchio, J., Palucis, M. C., & Meyer, C. R. (2024). Permafrost extent sets drainage density in the Arctic. *Proceedings of the National Academy of Sciences*, *121*(6), e2307072120. https://doi.org/10.1073/pnas.2307072120

Douglas, M. M., & Lamb, M. P. (2024). A Model for Thaw and Erosion of Permafrost Riverbanks. *Journal of Geophysical Research: Earth Surface*, *129*(4), e2023JF007452. https://doi.org/10.1029/2023JF007452

Farquharson, L. M., Mann, D. H., Grosse, G., Jones, B. M., & Romanovsky, V. E. (2016). Spatial distribution of thermokarst terrain in Arctic Alaska. *Geomorphology*, *273,* 116–133. https://doi.org/10.1016/j.geomorph.2016.08.007

Godin, E., Fortier, D., & Coulombe, S. (2014). Effects of thermo-erosion gullying on hydrologic flow networks, discharge and soil loss. *Environmental Research Letters*, *9*(10), 105010. https://doi.org/10.1088/1748-9326/9/10/105010

Gorelick, N., Hancher, M., Dixon, M., Ilyushchenko, S., Thau, D., & Moore, R. (2017). Google Earth Engine: Planetary-scale geospatial analysis for everyone. *Remote Sensing of Environment*, *202,* 18–27. https://doi.org/10.1016/j.rse.2017.06.031

Grosse, G., Jones, B., & Arp, C. (2013). 8.21 Thermokarst Lakes, Drainage, and Drained Basins. In *Treatise on Geomorphology* (pp. 325–353). Elsevier. https://doi.org/10.1016/B978-0-12-374739-6.00216-5

Hugelius, G., Strauss, J., Zubrzycki, S., Harden, J. W., Schuur, E. A. G., Ping, C.-L., Schirrmeister, L., Grosse, G., Michaelson, G. J., Koven, C. D., O'Donnell, J. A., Elberling, B., Mishra, U., Camill, P., Yu, Z., Palmtag, J., & Kuhry, P. (2014). Estimated stocks of circumpolar permafrost carbon with quantified uncertainty ranges and identified data gaps. *Biogeosciences*, *11*(23), 6573–6593. https://doi.org/10.5194/bg-11-6573-2014

Jones, B. M., Grosse, G., Arp, C. D., Jones, M. C., Walter Anthony, K. M., & Romanovsky, V. E. (2011). Modern thermokarst lake dynamics in the continuous permafrost zone, northern Seward Peninsula, Alaska. *Journal of Geophysical Research*, *116,* G00M03. https://doi.org/10.1029/2011JG001666

Jones, B. M., Grosse, G., Farquharson, L. M., Roy-Léveillée, P., Veremeeva, A., Kanevskiy, M. Z., Gaglioti, B. V., Breen, A. L., Parsekian, A. D., Ulrich, M., & Hinkel, K. M. (2022). Lake and drained lake basin systems in lowland permafrost regions. *Nature Reviews Earth & Environment*, *3*(1), 85–98. https://doi.org/10.1038/s43017-021-00238-9

Jorgenson, T., Yoshikawa, K., Kanevskiy, M., Shur, Y., Romanovsky, V., Marchenko, S., Grosse, G., Brown, J., & Jones, B. (2008). *Permafrost Characteristics of Alaska*.

Karjalainen, O., Aalto, J., Luoto, M., Westermann, S., Romanovsky, V. E., Nelson, F. E., Etzelmüller, B., & Hjort, J. (2019). Circumpolar permafrost maps and geohazard indices for near-future infrastructure risk assessments. *Scientific Data*, *6*(1), 190037. https://doi.org/10.1038/sdata.2019.37

Koch, J. C., Runkel, R. L., Striegl, R., & McKnight, D. M. (2013). Hydrologic controls on the transport and cycling of carbon and nitrogen in a boreal catchment underlain by continuous

permafrost. *Journal of Geophysical Research: Biogeosciences*, *118*(2), 698–712. https://doi.org/10.1002/jgrg.20058

Kokelj, S. V., Lantz, T. C., Tunnicliffe, J., Segal, R., & Lacelle, D. (2017). Climate-driven thaw of permafrost preserved glacial landscapes, northwestern Canada. *Geology*, *45*(4), 371–374. https://doi.org/10.1130/G38626.1

Kuhn, M. A., Varner, R. K., Bastviken, D., Crill, P., MacIntyre, S., Turetsky, M., Walter Anthony, K., McGuire, A. D., & Olefeldt, D. (2021). BAWLD-CH₄: A comprehensive dataset of methane fluxes from boreal and arctic ecosystems. *Earth System Science Data*, *13*(11), 5151–5189. https://doi.org/10.5194/essd-13-5151-2021

Lange, M. A., & Ahrens, T. J. (1983). The dynamic tensile strength of ice and ice-silicate mixtures. *Journal of Geophysical Research: Solid Earth*, *88*(B2), 1197–1208. https://doi.org/10.1029/JB088iB02p01197

Levenson, E. S., & Cooley, S. W. (2024). *Alaska Lake and Pond Occurrence Dataset* (https://doi.org/10.5281/zenodo.14199365; Version v1) [Dataset].

Lewkowicz, A. G., & Way, R. G. (2019). Extremes of summer climate trigger thousands of thermokarst landslides in a High Arctic environment. *Nature Communications*, *10*(1), 1329. https://doi.org/10.1038/s41467-019-09314-7

Loiko, S., Klimova, N., Kuzmina, D., & Pokrovsky, O. (2020). Lake Drainage in Permafrost Regions Produces Variable Plant Communities of High Biomass and Productivity. *Plants*, *9*(7), 867. https://doi.org/10.3390/plants9070867

Menzies, J. (2002). *Modern and past glacial environments: Revised student edition.* Elsevier.

Mullen, A. L., Watts, J. D., Rogers, B. M., Carroll, M. L., Elder, C. D., Noomah, J., Williams, Z., Caraballo-Vega, J. A., Bredder, A., Rickenbaugh, E., Levenson, E., Cooley, S. W., Hung, J. K. Y., Fiske, G., Potter, S., Yang, Y., Miller, C. E., Natali, S. M., Douglas, T. A., & Kyzivat, E. D. (2023). Using High-Resolution Satellite Imagery and Deep Learning to Track Dynamic Seasonality in Small Water Bodies. *Geophysical Research Letters*, *50*(7), e2022GL102327. https://doi.org/10.1029/2022GL102327

Nitze, I., Cooley, S. W., Duguay, C. R., Jones, B. M., & Grosse, G. (2020). The catastrophic thermokarst lake drainage events of 2018 in northwestern Alaska: Fast-forward into the future. *The Cryosphere*, *14*(12), 4279–4297. https://doi.org/10.5194/tc-14-4279-2020

Nitze, I., Grosse, G., Jones, B., Arp, C., Ulrich, M., Fedorov, A., & Veremeeva, A. (2017). Landsat-Based Trend Analysis of Lake Dynamics across Northern Permafrost Regions. *Remote Sensing*, *9*(7), 640. https://doi.org/10.3390/rs9070640

Obu, J., Westermann, S., Bartsch, A., Berdnikov, N., Christiansen, H. H., Dashtseren, A., Delaloye, R., Elberling, B., Etzelmüller, B., Kholodov, A., Khomutov, A., Kääb, A., Leibman,

M. O., Lewkowicz, A. G., Panda, S. K., Romanovsky, V., Way, R. G., Westergaard-Nielsen, A., Wu, T., … Zou, D. (2019). Northern Hemisphere permafrost map based on TTOP modelling for 2000–2016 at 1 km2 scale. *Earth-Science Reviews*, *193,* 299–316. https://doi.org/10.1016/j.earscirev.2019.04.023

Olefeldt, D., Goswami, S., Grosse, G., Hayes, D., Hugelius, G., Kuhry, P., McGuire, A. D., Romanovsky, V. E., Sannel, A. B. K., Schuur, E. A. G., & Turetsky, M. R. (2016). Circumpolar distribution and carbon storage of thermokarst landscapes. *Nature Communications*, *7*(1), 13043. https://doi.org/10.1038/ncomms13043

Olefeldt, D., Hovemyr, M., Kuhn, M. A., Bastviken, D., Bohn, T. J., Connolly, J., Crill, P., Euskirchen, E. S., Finkelstein, S. A., Genet, H., Grosse, G., Harris, L. I., Heffernan, L., Helbig, M., Hugelius, G., Hutchins, R., Juutinen, S., Lara, M. J., Malhotra, A., … Watts, J. D. (2021). The Boreal–Arctic Wetland and Lake Dataset (BAWLD). *Earth System Science Data*, *13*(11), 5127–5149. https://doi.org/10.5194/essd-13-5127-2021

Osterkamp, T. E., & Romanovsky, V. E. (1999). Evidence for warming and thawing of discontinuous permafrost in Alaska. *Permafrost and Periglacial Processes*, *10*(1), 17–37. https://doi.org/10.1002/(SICI)1099-1530(199901/03)10:1<17::AID-PPP303>3.0.CO;2-4

Pastick, N. J., Jorgenson, M. T., Goetz, S. J., Jones, B. M., Wylie, B. K., Minsley, B. J., Genet, H., Knight, J. F., Swanson, D. K., & Jorgenson, J. C. (2019). Spatiotemporal remote sensing of ecosystem change and causation across Alaska. *Global Change Biology*, *25*(3), 1171–1189. https://doi.org/10.1111/gcb.14279

Rangel, R. C., Parsekian, A. D., Farquharson, L. M., Jones, B. M., Ohara, N., Creighton, A. L., Gaglioti, B. V., Kanevskiy, M., Breen, A. L., Bergstedt, H., Romanovsky, V. E., & Hinkel, K. M. (2021). Geophysical Observations of Taliks Below Drained Lake Basins on the Arctic Coastal Plain of Alaska. *Journal of Geophysical Research: Solid Earth*, *126*(3), e2020JB020889. https://doi.org/10.1029/2020JB020889

Rantanen, M., Karpechko, A. Y., Lipponen, A., Nordling, K., Hyvärinen, O., Ruosteenoja, K., Vihma, T., & Laaksonen, A. (2022). The Arctic has warmed nearly four times faster than the globe since 1979. *Communications Earth & Environment*, *3*(1), Article 1. https://doi.org/10.1038/s43247-022-00498-3

Rawlins, M. A., Steele, M., Holland, M. M., Adam, J. C., Cherry, J. E., Francis, J. A., Groisman, P. Y., Hinzman, L. D., Huntington, T. G., Kane, D. L., Kimball, J. S., Kwok, R., Lammers, R. B., Lee, C. M., Lettenmaier, D. P., McDonald, K. C., Podest, E., Pundsack, J. W., Rudels, B., … Zhang, T. (2010). Analysis of the Arctic System for Freshwater Cycle Intensification: Observations and Expectations. *Journal of Climate*, *23*(21), 5715–5737. https://doi.org/10.1175/2010JCLI3421.1

Riordan, B., Verbyla, D., & McGuire, A. D. (2006). Shrinking ponds in subarctic Alaska based on 1950–2002 remotely sensed images. *Journal of Geophysical Research: Biogeosciences*, *111*(G4), 2005JG000150. https://doi.org/10.1029/2005JG000150

Roach, J., Griffith, B., Verbyla, D., & Jones, J. (2011). Mechanisms influencing changes in lake area in Alaskan boreal forest: MECHANISMS FOR LAKE AREA CHANGE IN ALASKA. *Global Change Biology*, *17*(8), 2567–2583. https://doi.org/10.1111/j.1365-2486.2011.02446.x

Romanovsky, V., Burgess, M., Smith, S., Yoshikawa, K., & Brown, J. (2002). Permafrost temperature records: Indicators of climate change. *Eos, Transactions American Geophysical Union*, *83*(50), 589–594. https://doi.org/10.1029/2002EO000402

Romanovsky, V. E., Drozdov, D. S., Oberman, N. G., Malkova, G. V., Kholodov, A. L., Marchenko, S. S., Moskalenko, N. G., Sergeev, D. O., Ukraintseva, N. G., Abramov, A. A., Gilichinsky, D. A., & Vasiliev, A. A. (2010). Thermal state of permafrost in Russia. *Permafrost and Periglacial Processes*, *21*(2), 136–155. https://doi.org/10.1002/ppp.683

Schädel, C., Bader, M. K.-F., Schuur, E. A. G., Biasi, C., Bracho, R., Čapek, P., De Baets, S., Diáková, K., Ernakovich, J., Estop-Aragones, C., Graham, D. E., Hartley, I. P., Iversen, C. M., Kane, E., Knoblauch, C., Lupascu, M., Martikainen, P. J., Natali, S. M., Norby, R. J., … Wickland, K. P. (2016). Potential carbon emissions dominated by carbon dioxide from thawed permafrost soils. *Nature Climate Change*, *6*(10), 950–953. https://doi.org/10.1038/nclimate3054

Schuur, E. A. G., McGuire, A. D., Schädel, C., Grosse, G., Harden, J. W., Hayes, D. J., Hugelius, G., Koven, C. D., Kuhry, P., Lawrence, D. M., Natali, S. M., Olefeldt, D., Romanovsky, V. E., Schaefer, K., Turetsky, M. R., Treat, C. C., & Vonk, J. E. (2015). Climate change and the permafrost carbon feedback. *Nature*, *520*(7546), 171–179. https://doi.org/10.1038/nature14338

Smith, L. C., Sheng, Y., MacDonald, GM., & Hinzman, L. D. (2005). Disappearing Arctic Lakes. *Science*, *308.* https://www.science.org/doi/full/10.1126/science.1108142?casa_token=d5ccuMO-1s8AAAAA%3ARdITjR7YHWYfpzCo07dLrWtWbnSndF0LpGBPrau-jALGVq7UtQKkreECoV7tbh56llGjm-RtuBwknw

Swanson, D. K. (2019). Thermokarst and precipitation drive changes in the area of lakes and ponds in the National Parks of northwestern Alaska, 1984–2018. *Arctic, Antarctic, and Alpine Research*, *51*(1), 265–279. https://doi.org/10.1080/15230430.2019.1629222

Tarnocai, C., Canadell, J. G., Schuur, E. a. G., Kuhry, P., Mazhitova, G., & Zimov, S. (2009). Soil organic carbon pools in the northern circumpolar permafrost region. *Global Biogeochemical Cycles*, *23*(2). https://doi.org/10.1029/2008GB003327

Treat, C. C., Natali, S. M., Ernakovich, J., Iversen, C. M., Lupascu, M., McGuire, A. D., Norby, R. J., Roy Chowdhury, T., Richter, A., Šantrůčková, H., Schädel, C., Schuur, E. A. G., Sloan, V. L., Turetsky, M. R., & Waldrop, M. P. (2015). A pan-Arctic synthesis of CH_4 and CO_2 production from anoxic soil incubations. *Global Change Biology*, *21*(7), 2787–2803. https://doi.org/10.1111/gcb.12875

USGS. (n.d.). *National Hydrography Dataset Best Resolution for Hydrologic Unit (HU) 12* [Dataset]. https://www.usgs.gov/national-hydrography/access-national-hydrography-products

Vandenberghe, J., French, H. M., Gorbunov, A., Marchenko, S., Velichko, A. A., Jin, H., Cui, Z., Zhang, T., & Wan, X. (2014). The L ast P ermafrost M aximum (LPM) map of the N orthern H emisphere: Permafrost extent and mean annual air temperatures, 25–17 ka BP. *Boreas*, *43*(3), 652–666. https://doi.org/10.1111/bor.12070

Velicogna, I., Tong, J., Zhang, T., & Kimball, J. S. (2012). Increasing subsurface water storage in discontinuous permafrost areas of the Lena River basin, Eurasia, detected from GRACE. *Geophysical Research Letters*, *39*(9), 2012GL051623. https://doi.org/10.1029/2012GL051623

Verpoorter, C., Kutser, T., Seekell, D. A., & Tranvik, L. J. (2014). A global inventory of lakes based on high-resolution satellite imagery. *Geophysical Research Letters*, *41*(18), 6396–6402. https://doi.org/10.1002/2014GL060641

Walter Anthony, K., Daanen, R., Anthony, P., Schneider Von Deimling, T., Ping, C.-L., Chanton, J. P., & Grosse, G. (2016). Methane emissions proportional to permafrost carbon thawed in Arctic lakes since the 1950s. *Nature Geoscience*, *9*(9), 679–682. https://doi.org/10.1038/ngeo2795

Walvoord, M. A., & Kurylyk, B. L. (2016). Hydrologic Impacts of Thawing Permafrost—A Review. *Vadose Zone Journal*, *15*(6), vzj2016.01.0010. https://doi.org/10.2136/vzj2016.01.0010

Walvoord, M. A., & Striegl, R. G. (2007). Increased groundwater to stream discharge from permafrost thawing in the Yukon River basin: Potential impacts on lateral export of carbon and nitrogen. *Geophysical Research Letters*, *34*(12), 2007GL030216. https://doi.org/10.1029/2007GL030216

Walvoord, M. A., Voss, C. I., & Wellman, T. P. (2012). Influence of permafrost distribution on groundwater flow in the context of climate-driven permafrost thaw: Example from Yukon Flats Basin, Alaska, United States. *Water Resources Research*, *48*(7), 2011WR011595. https://doi.org/10.1029/2011WR011595

Wang, J., Pottier, C., Cazals, C., Battude, M., Sheng, Y., Song, C., Sikder, M. S., Yang, X., Ke, L., Gosset, M., Oliveira, R. R. A., Grippa, M., Girard, F., Allen, G. H., Biancamaria, S., Smith, L., Crétaux, J.-F., & Pavelsky, T. M. (2023). *The Surface Water and Ocean Topography Mission (SWOT) Prior Lake Database (PLD): Lake mask and operational auxiliaries*. https://doi.org/10.22541/au.170258987.72387777/v1

Watts, J. D., Kimball, J. S., Jones, L. A., Schroeder, R., & McDonald, K. C. (2012). Satellite Microwave remote sensing of contrasting surface water inundation changes within the Arctic–Boreal Region. *Remote Sensing of Environment*, *127,* 223–236. https://doi.org/10.1016/j.rse.2012.09.003

Webb, E. E., & Liljedahl, A. K. (2023). Diminishing lake area across the northern permafrost zone. *Nature Geoscience*, *16*(3), 202–209. https://doi.org/10.1038/s41561-023-01128-z

Webb, E. E., Liljedahl, A. K., Cordeiro, J. A., Loranty, M. M., Witharana, C., & Lichstein, J. W. (2022). Permafrost thaw drives surface water decline across lake-rich regions of the Arctic. *Nature Climate Change*, *12*(9), Article 9. https://doi.org/10.1038/s41558-022-01455-w

Wellman, T. P., Voss, C. I., & Walvoord, M. A. (2013). Impacts of climate, lake size, and supra- and sub-permafrost groundwater flow on lake-talik evolution, Yukon Flats, Alaska (USA). *Hydrogeology Journal*, *21*(1), 281–298. https://doi.org/10.1007/s10040-012-0941-4

Wild, B., Andersson, A., Bröder, L., Vonk, J., Hugelius, G., McClelland, J. W., Song, W., Raymond, P. A., & Gustafsson, Ö. (2019). Rivers across the Siberian Arctic unearth the patterns of carbon release from thawing permafrost. *Proceedings of the National Academy of Sciences*, *116*(21), 10280–10285. https://doi.org/10.1073/pnas.1811797116

CHAPTER III

TRACKING SEASONAL TO INTERANNUAL CHANGES TO PAN-ARCTIC LAKE AREA

1. Introduction

Lakes serve as both drivers and indicators of environmental change in the Arctic (Adrian et al., 2009; Saros et al., 2023; Schindler, 2009). They regulate biological productivity (Lesack & Marsh, 2010), as well as energy, water, and carbon exchanges between the land and atmosphere (Algesten et al., 2004; Franz et al., 2018; Prowse et al., 2011; Tranvik et al., 2009; Walter Anthony et al., 2016; Webb et al., 2021). In recent decades, lake area has emerged as a key variable for detecting the impacts of amplified Arctic warming (Rantanen et al., 2022) and the intensifying hydrologic cycle (Rawlins et al., 2010) because processes that are otherwise difficult to observe directly, such as permafrost thaw and water storage, can be expressed through lake area change. Decadal-scale, satellite-based lake area trends have revealed the prevalence of processes such as thermokarst lake expansion and catastrophic drainage (Carroll et al., 2011; Nitze et al., 2017; Riordan et al., 2006; Smith et al., 2005; Su et al., 2023; Webb & Liljedahl, 2023), while detailed field studies have emphasized the importance of vegetation encroachment for declining lake area and ground ice contributions for lake expansion (Fedorov et al., 2014; Roach et al., 2011). Seasonality-focused studies demonstrate that fine-scale, intra-annual shoreline fluctuations compound to produce significant regional lake area change with notable consequences for CO_2 and CH_4 emissions (Cooley et al., 2017, 2019; Mullen et al., 2023). Ultimately, our understanding of Arctic lake area dynamics and the mechanisms driving them is fundamentally related to the spatiotemporal resolution of our observations.

Despite the importance of both the seasonal and interannual components of Arctic lake area trends, their interactions are currently unquantified. Seasonality is a defining aspect of Arctic hydrology, as precipitation is stored seasonally as snow before contributing a pulse of freshwater inputs to the landscape following melt (Bring et al., 2016; Rawlins & Karmalkar, 2024). Models suggest that the severity of both warming amplification and water cycle intensification vary across seasons. The largest changes, such as increasing precipitation and temperatures, are occurring in winter (Rantanen et al., 2022; Rawlins et al., 2010; Rawlins & Karmalkar, 2024), while observations show that snowmelt is occurring earlier across the Arctic

region (Foster et al., 2013; Semmens et al., 2013; Tan et al., 2011). Interannual changes to the timing of lake seasonality, however, remain an open question because our observations are limited to either a single season or relatively small study sites (Cooley et al., 2017, 2019; Mullen et al., 2023). Many high-latitude ecological processes are sensitive to the timing of water availability, such as flowering of tundra plants, the production and migratory patterns of terrestrial and aquatic organisms, and host-parasite interactions (Wrona et al., 2016).

Tracking seasonal lake area fluctuations over multiple years can also improve our interpretation of longer-term analyses, which treat seasonality as noise in the context of measuring changes to the typical summer lake area. When time series are sufficiently dense, analysis techniques generally deconstruct temporal patterns into their seasonal and trend components. Due to the sparse temporal sampling from historical satellite imagery, some studies must ignore seasonality and simply use the available data (Riordan et al., 2006). When multiple images per year are available, the most common strategy for removing seasonal contamination of lake area trends is to establish a pre-defined annual sampling window (Carroll et al., 2011; Nitze et al., 2017; Webb et al., 2021). This raises the possibility of false trend detection when mean lake area stays constant while the timing of lake area drawdown shifts earlier or later. Another approach is to explicitly exclude ephemeral or seasonal water bodies (Smith et al., 2005). Ignoring intra-annual lake area dynamics raises several issues for understanding longer-term change. First, seasonality dominates lake extent variability at a global scale (Li et al., 2025), and thus should be accounted for when determining long-term trends. Second, conclusions about the persistence of observed lake area changes are inherently limited by sparse observations. Smith et al. (2005)'s finding that lakes larger than 40 ha are, "stable landscape features that do not disappear or appear in response to short-term seasonal variability," was derived from a handful of overlapping summer scenes. Several drained lake basins larger than 40 ha have since been shown to seasonally refill during the spring freshet, in some cases causing repeated hazardous outburst floods (Arp et al., 2020). Finally, changes to the timing, maximum, minimum, or amplitude of intra-annual lake area variability may provide more meaningful indicators of Arctic climate change.

Here, we map nine years of sub-seasonal lake area dynamics an unprecedented spatiotemporal resolution across the entire pan-Arctic region. This effort is uniquely enabled by

Sentinel-2's 10 m spatial resolution and near-daily revisits in northern latitudes, as well as the new Prior Lake Database (PLD), which maps lakes larger than 1 ha globally (Wang et al., 2025). Using this Sentinel-2 based dataset for the years 2017-2025, we first establish a contemporary baseline for Arctic lake area seasonality to reveal the dominant seasonal patterns, their timing and spatial distribution, and their linkages to early season melt processes. Next, we detect locations exhibiting significant increasing and decreasing lake area trends across the study period and identify potential mechanisms using our dense time series data, the spatial distribution of significant trends, and interpretation of Sentinel-2 imagery. Finally, we investigate how seasonal lake area dynamics respond to earlier snowmelt and discuss how this linkage may influence interannual summer lake area trends.

2. Study Area

This study maps lake area dynamics across the pan-Arctic region, defined as the entire land surface greater than 60˚ N. In total, this study area includes 3,228,001 lakes and 759,546 km^2 of lake area (Wang et al., 2025). The Arctic encompasses distinct hydrophysiographic regions including Arctic tundra, Boreal plains, the Canadian Shield, Mountains, glaciers, and interspersed wetlands (Bring et al., 2016). At a regional scale, the spatial distribution of lakes reflects the influence of prior glaciation, permafrost history, peatlands, river networks, and dams (Levenson et al., 2025; McClelland et al., 2004; Smith et al., 2007). The study region's diversity in characteristics such as drainage area, latitude, geology, permafrost extent, human activity, ecological dynamics, and climate enable us to assess their integrated influence on lakes' temporal dynamics.

3. Methods

3.1. Data

Our study utilizes Sentinel-2 imagery to track water area and ice-off dynamics within PLD lake polygons. We analyze all available Sentinel-2 images between March 1 and October 1 for years 2017-2025 in Google Earth Engine (GEE) (Gorelick et al., 2017). Specifically, we utilize the 10-m resolution red, blue, and near-infrared (NIR) top-of-atmosphere (TOA) bands to produce daily mosaics for water classification, and the green band for ice classification. We also

use the S2 cloud probability product (Schwehr, 2020) to mask clouds before calculating the basin's total lake area observed in each image. We use a strict image filtering approach for our water and ice classifications (Section 3.2.) by removing any observations with less than 100% cloud-free coverage of the lakes. We also remove images with a solar elevation angle less than 45˚ due to the classification errors associated with cloud and topographic shadows.

We use HydroBASINS (Lehner & Grill, 2013) Level 10 sub-basins as our unit of analysis, with a mean area of 151.1 (± 90.6) km^2. We produce 72,645 basin-level lake area time series for 653,805 unique basin-year combinations, representing all basins in our study region that intersect the Surface Water and Ocean Topography (SWOT) Prior Lake Database (PLD) (Wang et al., 2025). Basins provide a hydrologically meaningful boundary to aggregate lakes and may limit intra-basin variability in comparison to grid cells as lakes are topographically associated.

3.2. Lake Water Area Time Series

This study focuses on tracking the extent of open water (i.e., no emergent vegetation) in lakes. We produce lake area time series aggregated to the basin level, which enables our analysis of high spatiotemporal resolution Sentinel-2 imagery across such a large study domain. To produce water area time series in each basin, we first produce a maximum lake extent mask by buffering the PLD lake polygons by 80 m and clipping to the basin of interest. Many boundaries between sub-basins are topographically defined by lakes themselves, and therefore individual water bodies can be split into neighboring basins. For each day within the study period, we produce cloud-masked Sentinel-2 mosaics and convert to Normalized Difference Water Index (NDWI) images (McFEETERS, 1996), and clip to the maximum lake extent mask. We apply an adaptive NDWI thresholding algorithm (Cooley et al., 2017) to each NDWI image to classify water and sum the total open water area within the basin. We apply this protocol to every available image within the study period that passes our cloud, coverage, and solar angle filters and iterate through all 72,645 basins individually.

The lake tracking and adaptive NDWI thresholding open water classification methods have been previously validated to show strong agreement with manually classified lake extents (Cooley et al., 2017, 2019; Levenson et al., 2025) and lake levels measured by pressure

transducers and in situ gauges (Cooley et al., 2019; Levenson et al., in prep). Given the importance of the melt season for characterizing Arctic lake seasonality, we carry out additional manual verification of performance during ice-affected dates (Section 3.3). Lastly, we apply a 5-observation median filter to reduce the impact of water classification errors potentially caused by clouds, shadows, or variable atmospheric conditions.

3.3 Ice Tracking and Observation Filtering

A central challenge to mapping Arctic surface water dynamics is that important water storage fluctuations occur while snow and ice is still present. To help identify and remove invalid water classifications caused by snow and ice contamination, we produce lake ice coverage time series for each basin-year from March 1 – July 15. To do this, we use the original (i.e., unbuffered) PLD lake polygons and a red-band thresholding algorithm (Pletcher et al., 2025) to produce time series of lake ice coverage, expressed as a percentage of the basin's total lake area covered by ice. In addition, we identify the day of snow disappearance across the entire basin using the 500-m resolution MODIS/TERRA Daily Snow Cover dataset (Hall & Riggs, 2021). Our manual assessment of water classification performance under varying snow and ice conditions suggests that the adaptive thresholding completely fails when the landscape is fully covered by snow and ice (i.e., ice coverage = 100% with snow-covered lake margins) due to the unimodal NDWI histogram. However, lakes typically retain snow and ice later than the surrounding land (Cooley et al., in review). During this melt season period when snowmelt has occurred on land while snow and ice persists on lakes, we find that our water classification capably delineates lake area once open water is visible (Figure 3.1). Furthermore, the most significant lake area fluctuations occur during this early period in many basins (Figure 3.1). Therefore, we define the initial observation each year within a basin as the first measurement after the MODIS-observed day of snow disappearance has passed and the lake ice fraction has dropped below 75%.

Our combined lake water area and ice coverage time series support multiple definitions of lake area depending on research objectives. Analyses that require separate treatment of frozen and liquid lake water, such as investigations into albedo, can use the lake ice fraction to partition the total lake area into open and ice-covered water. Our aims here use lake area as a proxy for

water storage to understand hydrologic dynamics and geomorphic drivers of lake area change. Therefore, we use our ice fraction time series strictly to: (a) identify the annual time series starting point, and (b) to investigate how the timing of melt processes interacts with lake area dynamics that propagate into the growing season.

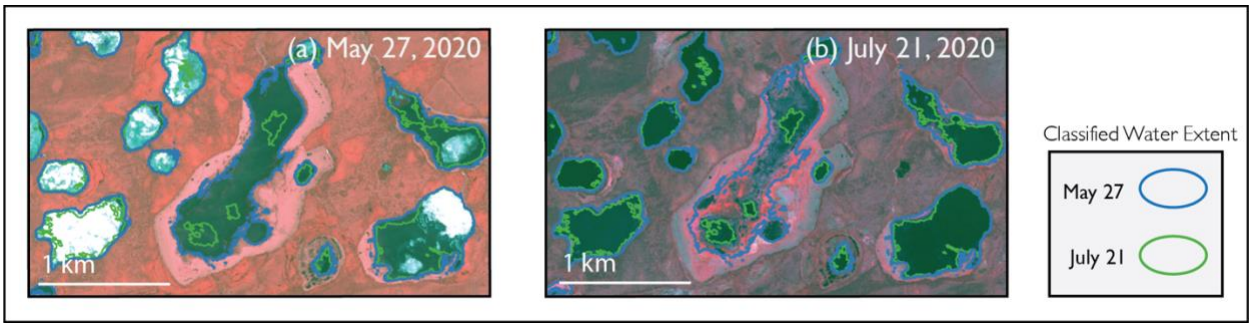

Figure 3.1: Example of our water classification in the North Siberian Lowland (67.6° N, 146.5° E) for (a) an early season Sentinel-2 image with a measured lake ice fraction of 43% for the entire basin (not fully pictured), and (b) a mid-summer image. Both images show false color composites to emphasize the contrast between water, ice, and vegetation. Panel a demonstrates how ice and water are both counted as lake area, as well as the importance of including ice-affected dates to understand Arctic lake behavior. The pictured ephemeral lake, measuring an area of 390 ha, fills and drains annually.

3.4. Spatial Variability Analysis

Using our filtered lake area time series, we calculate a variety of summary statistics to enable comparison of lake seasonality across basins using two approaches (Table A8). To reduce the impact of observation gaps and noisy time series when calculating seasonal amplitude and timing metrics, we remove individual years with less than five valid observations, no valid observations within 1 standard deviation of the average peak day of year, or a negative temporal autocorrelation between observations. After filtering, we first calculate overall metrics across the entire nine-year study period including mean lake area, standard deviation, coefficient of variation, interquartile range, and range. Next, for each individual year we calculate these same metrics as well as the timing of peak lake area, snowmelt disappearance, ice-breakup initiation, and ice-off for each year individually. To understand the spatial variability in average peak lake

area timing, we produce a linear OLS regression between average snowmelt timing and maximum lake area day of year (DOY).

We also characterize the baseline seasonal lake area progression while accounting for interannual variability in observation frequency and lake area dynamics. To do this, we interpolate water area time series that meet our analysis threshold described above, calculate the median lake area on each DOY, and apply a 7-day rolling mean. This produces a baseline lake area time series with daily resolution (Figure 3.2). Using this baseline, we calculate a new metric called the Lake Seasonality Index (LSI) based on the seasonality index as traditionally applied to precipitation (Walsh & Lawler, 1981). LSI is calculated as the cumulative absolute deviation from mean water area, thus accounting for the temporal component of seasonal variability while normalizing for mean water area. To identify distinct seasonal behavior across basins based on the shape of their baseline seasonal time series, we rescale each time series to 100 time steps and perform an unsupervised K-means clustering on the progression of lake area anomalies. We test 2-5 clusters and select the number with the highest silhouette score.

We develop a statistical model to better understand the physical and climate controls over the spatial distribution of LSI across the Arctic. We compile climate predictor variables for each basin by aggregating the monthly precipitation and evapotranspiration values from the climate reanalysis ERA5 Land dataset (Muñoz-Sabater et al., 2021) to average winter, spring, summer, and fall water balance (P-ET). We also use several physical basin attributes from the BasinATLAS dataset, including drainage area, soil and geologic properties, forest cover, permafrost extent (Table A9). Given the high-dimensionality and potential collinearity between the predictor variables, we use a Least Absolute Shrinkage and Selection Operator (LASSO) regression, which automatically performs variable selection by shrinking weak predictor coefficients to zero through L1 regularization. The relative importance of each selected predictor is interpreted through the magnitude and sign of their coefficients.

3.5. Interannual Variability Analysis

We test each basin for monotonic trends in mean ice-free lake area over 2017-2025. We remove basins that have less than 1 km^2 in mean lake area, negative temporal autocorrelation between observations, and less than 7 unique years of data with 5 observations per year. We use

a Mann-Kendall test for trend with a significance threshold of 0.05 and a Theil-Sen slope estimator for percent change calculation. Due to the large sample size (n=28,027), we apply a Benjamini-Hochberg correction for false discovery rate. We recognize that trends over a nine-year study period are susceptible to climate oscillations and coincident short-term trends in the regional water balance. Therefore, we utilize these trends to identify case studies of lake area change mechanisms through combined interpretation of seasonal time series, Sentinel-2 imagery, and ancillary climate and hydrologic data.

Using our lake area time series, we also investigate how the seasonal lake area progression responds to interannual variability in snowmelt timing. Specifically, we test the relationship between snowmelt timing and peak lake area timing, maximum lake area, total seasonal variability, mean summer (ice-free) lake area, minimum lake area, and drawdown duration (number of days from maximum to mean lake area). To do this, we normalize these annual statistics to basin-level anomalies and pool data across basins. We use a strict filtering protocol to limit our analysis to basins with significant variability in snowmelt timing (standard deviation > 7 days) and sufficient lake area observations to quantify the interannual differences in the tested metrics. To account for extended observation gaps, we first remove basin-year combinations with fewer than 5 valid observations or zero observations within one standard deviation of the basin's average peak lake area date. Next, we remove basins with fewer than 6 years of data meeting these criteria. For each response variable, we pool all basin-year anomalies and use a robust linear regression to test the null hypothesis that the slope between snowmelt timing and the lake area response metric is zero.

4. Results

We mapped lake area in 72,593 basins with an average revisit period of 6.7 (± 2.2) days. The total mean lake area for the study region is 790,958.3 km^2, which is a 4.13% increase over the PLD static areas for the region. Across the nine-year period, the total lake area variability was 113,729 km^2 with an annual average seasonal variability of 70,230 km^2, suggesting that seasonal variability contributes 62% of total observed lake area change over the nine-year period. 42,231 basins meet our thresholds for analysis, requiring a mean lake area greater than 1 km^2

(removed 26,613 basins), positive temporal autocorrelation between observations (removed 3,654 basins), and minimum observation requirements (removed 95 basins).

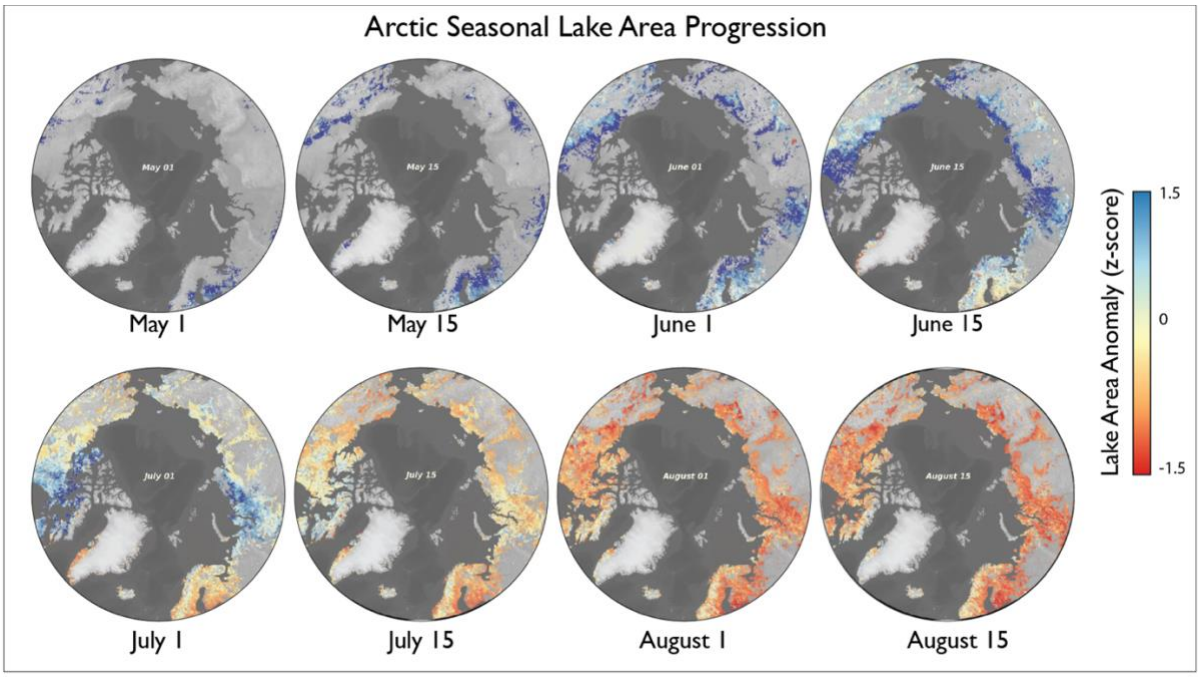

Figure 3.2: Spatiotemporal patterns of pan-Arctic seasonal lake area fluctuations averaged across 2017-2025.

4.1. Spatial Patterns

At the pan-Arctic scale, the spatial distribution of LSI is weakly explained by broad-scale physical and climate variables ($R^2 = 0.14$; Table A9), with the most important predictors and their influence being upstream human population (+), sand (-), silt (+), and permafrost percentage (-), as well as river area (+). Compared to these static basin attributes, water balance predictors had relatively little influence on spatial differences in lake seasonality. Mapping the lake variability metrics (Figure 3.3) reveals significant spatial organization and the influence of river networks and floodplains, suggesting that surface hydrologic connectivity is central to driving lake area fluctuations. Notable rivers and floodplains visible in the maps of seasonal lake area variability (Figure 3.3c and 3.3e) include the Ob River Floodplain, Yukon Flats, Lena River, and Kolyma Lowlands. At finer scales, seasonal patterns can vary over relatively short distances

despite similar climate influences due to local heterogeneity in lake morphology and connectivity. For example, the West Siberian Plain exhibits remarkable contrast between seasonally stable lakes in tundra environments directly adjacent to highly variable fluvially formed lakes within the Ob River floodplain, which respond to water inputs from as far south as the Altai Mountains.

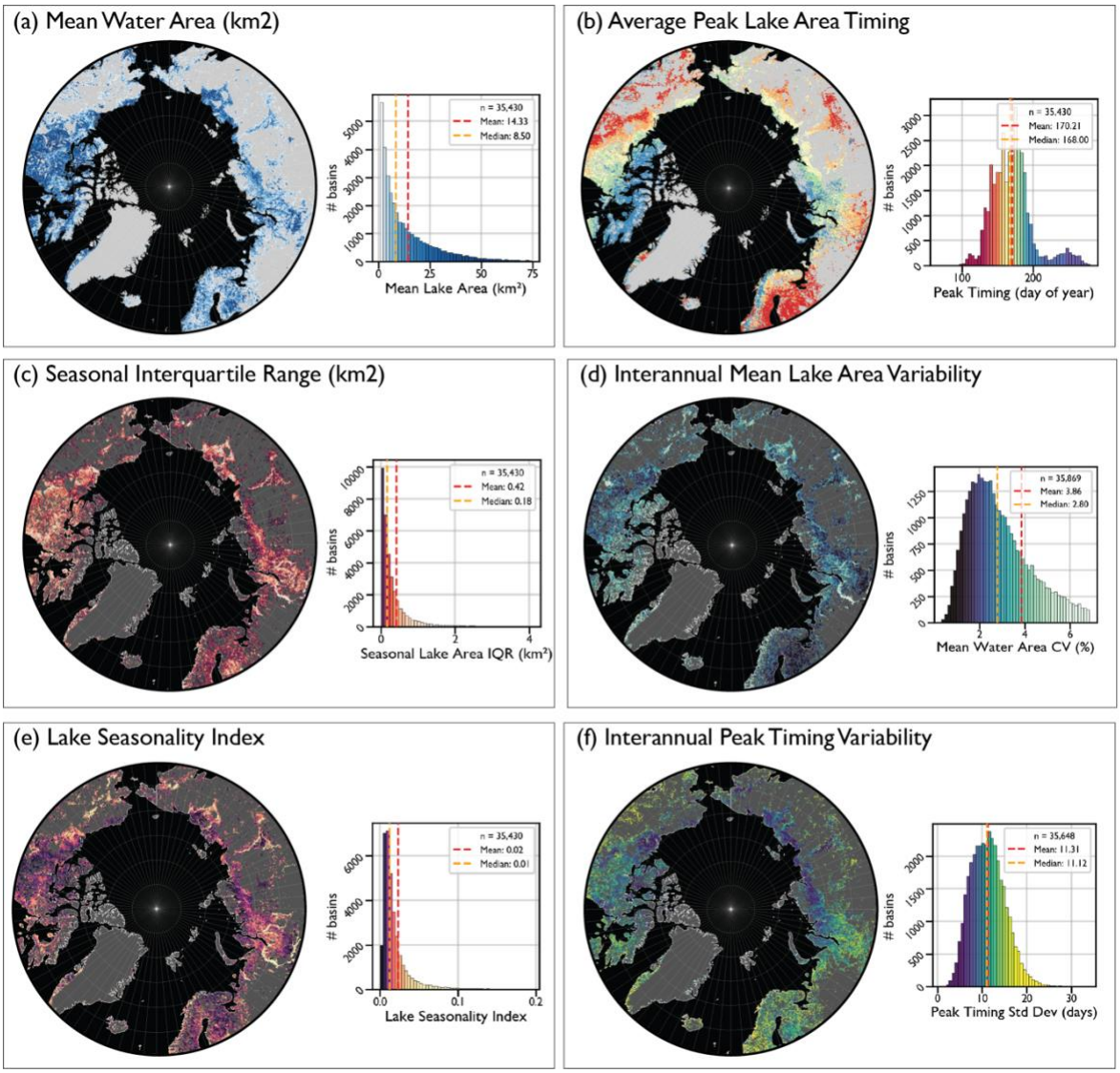

Figure 3.3: Lake area summary statistics and their spatial distribution. Visualizations and statistics are limited to 44,324 basins meeting analysis criteria.

A basin's average peak lake area timing (Figure 3.3b) is strongly correlated with its snow disappearance date ($R^2 = 0.62$; $p < 0.001$; n=42,231). On average, the first valid lake area observation occurs 3.9 (± 9.9) days after snow disappearance; however, this lag has a right-tailed distribution with considerable spatial variability. In many cases, lakes reach their maximum extent while still partially frozen (e.g., Figures 3.2a and 3.4) while others continue to expand following ice-off. Our unsupervised k-means time series clustering of the baseline lake area time series showed that most basins peak in the early season soon after snowmelt while ice is present before a gradual drawdown throughout the summer (Figures 3.4a and 3.4b). In a minority of basins (n=3,888), lakes slowly expand before stabilizing approximately 35% of the way through their open water season (Figure 3.4c). Inspection of the spatial distribution of these various regimes suggests that the gradual seasonal lake expansion is caused by delayed water inputs from glaciers, alpine environments, or human management, while the remaining basins reflect a typical snowmelt regime. Within the snowmelt dominated basins, the k-means clustering separated basins that peak near their first valid observation (n=17,891) from those with a delayed peak (n=9,075), likely due to increased drainage area that increases the lag between local snowmelt and upstream water inputs.

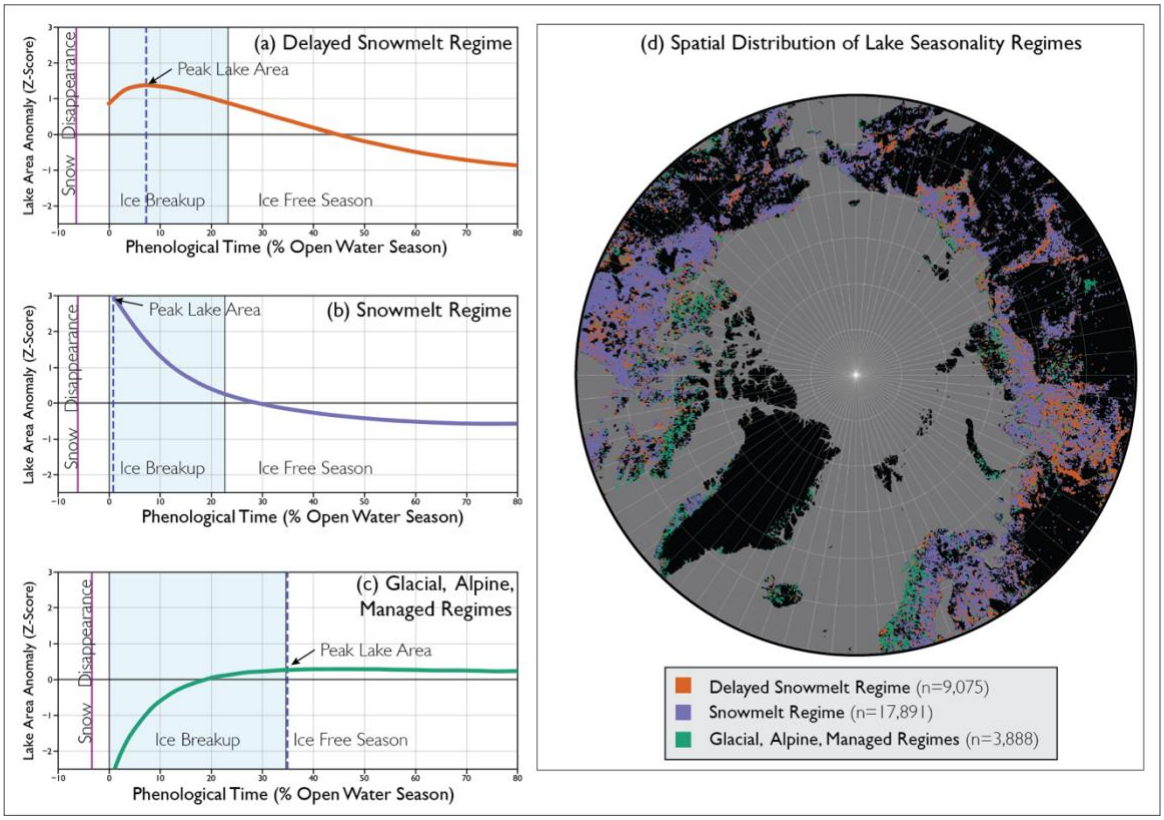

Figure 3.4: Results from the unsupervised k-means clustering of baseline seasonal lake area progressions. Time series (a-c) show the center of clusters' lake area anomalies. The names for each cluster are interpretations of the dominant hydrologic processes for each cluster based on the time series progressions and their spatial distribution (d).

4.2. Interannual Lake Area Trends

We find that 21.0% of analyzed basins have significant ($p_{adj} < 0.05$) monotonic trends in annual ice-free mean lake area over the course of the study period. Of these basins, 76.5% exhibit decreasing lake area. The spatial distribution of significant directional trends (Figure A10) reveals various clusters, such as decreasing lake area in the West Siberian Plain, Kolyma Lowlands, Lena River basin, and the head of the Mackenzie River Delta. These are contrasted by increasing lake area trends in the Northeast Siberian Coastal Tundra and the Yukon River Basin. The relatively short nine-year record must be acknowledged when interpreting these trends. In contrast to multi-decadal Arctic lake area studies that generally attribute trends to evolutionary trajectories (Smith et al., 2005; Webb & Liljedahl, 2023), many basins' trends may result from

our study period coinciding with reversible processes influencing the regional water balance such as the Arctic Oscillation, water management practices, or short-term trends in surface water runoff. For example, the cluster of basins with increasing lake area trends in the Yukon Flats coincides with a period of significant monotonic increases in Yukon River Discharge (p-value = 0.016; Table A10), whereas the 53.1% of the 753 decreasing trends observed in the Canadian Mackenzie River watershed and western Canadian Shield are significantly correlated with precipitation trends ($p < 0.05$). However, we identify several examples of lake area declines that are attributable to permafrost and ecological processes (Figures 3.5 and 3.6).

Through interpretation of our time series data and inspection of Sentinel-2 imagery, we detect several previously observed as well as – to the best of our knowledge – previously undocumented lake drainage events. For example, catastrophic lake drainages caused by permafrost destabilization on the Seward Peninsula, AK in 2018 (Nitze et al., 2020) are clearly reflected in the basin-level time series (Figure A11). Many basins share this lake drainage time series signature wherein stepwise decreases in lake area are followed by years with seasonal maximum lake area that is less than previous mean lake area measurements. This pattern is especially prevalent in the West Siberian Plains and the Yamal Peninsula, where several drainage events are visible in Sentinel-2 imagery (e.g., Figure 3.5). Using our temporally dense time series, we can discriminate persistent or catastrophic lake drainage occurrences from lakes that appear to have drained but still fill seasonally (Figure A12).

Permafrost is more extensive in basins with increasing lake area trends relative to basins with decreasing trends according to a significant Mann-Whitney U-Test (p-value < 0.001; Figure A13), which is in agreement with multi-decadal trends (Webb & Liljedahl, 2023) and conceptual hypotheses that initial permafrost thaw causes lake expansion followed by drainage (Smith et al., 2005). We observe that the directional lake area trend can diverge over very short distances in the discontinuous permafrost zone, such as in the thermokarst terrain in the middle portion of the Lena River watershed (Figure 3.6). Long-term field monitoring of a single thermokarst lake in this region showed steady increases in water surface area that were directly attributable to increased water balance from melting ground ice (Fedorov et al., 2014). We observe similar patterns of continued lake area increases at very fine spatial scales (e.g., < 30 m shoreline fluctuations; Figure 3.6b) that match expectations from Fedorov et al. (2014). In addition, we

identify a cluster of basins that are directly adjacent to these expanding lakes that exhibit consistent year-over-year decreasing lake area (Figure 3.6a). With apparent connections between end-of-season conditions and the following year's initial lake area (e.g., Figure 3.6a), these consistent trends may reflect more gradual processes such as vegetation infilling; however, altimetry or field data may be required to discriminate between lake drainage, terrestrialization, or water balance drivers.

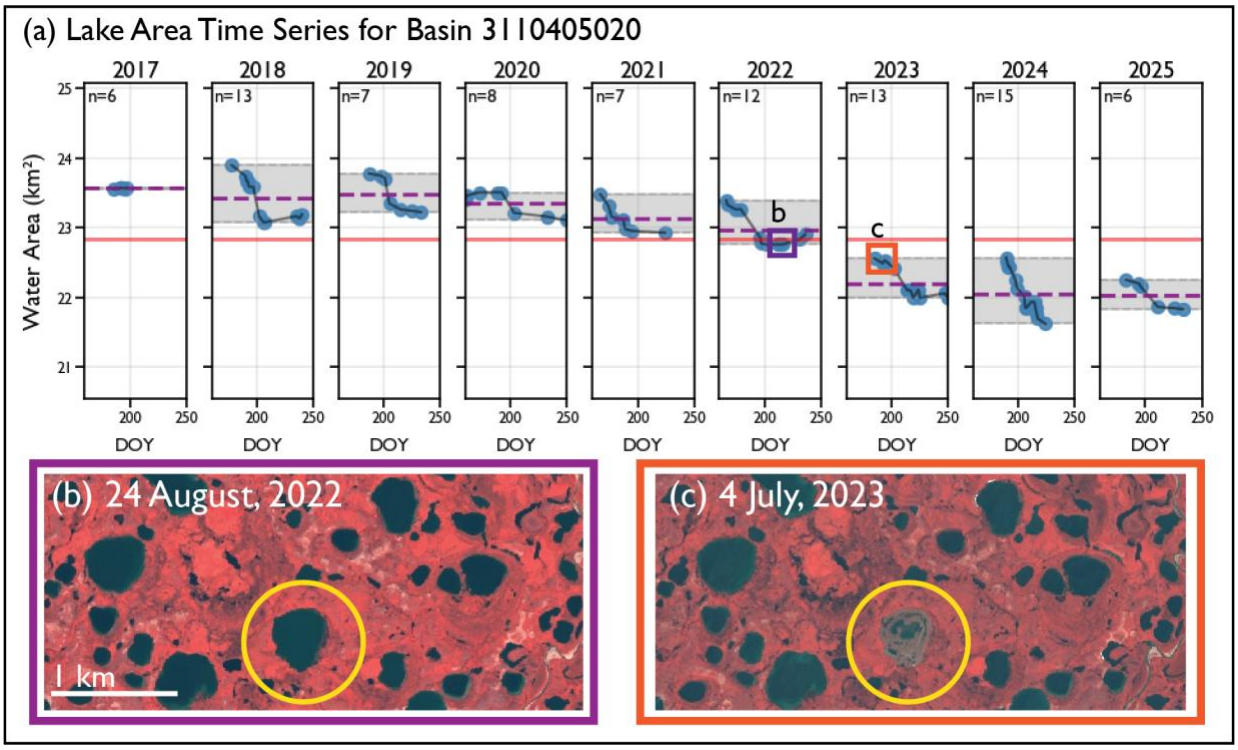

Figure 3.5: Example time series (a) and visual evidence (b) and (c) of lake drainage from the Yamal Peninsula, Russia. Images (b) and (c) display basin subsets to highlight the lake drainage event driving the negative lake area trend.

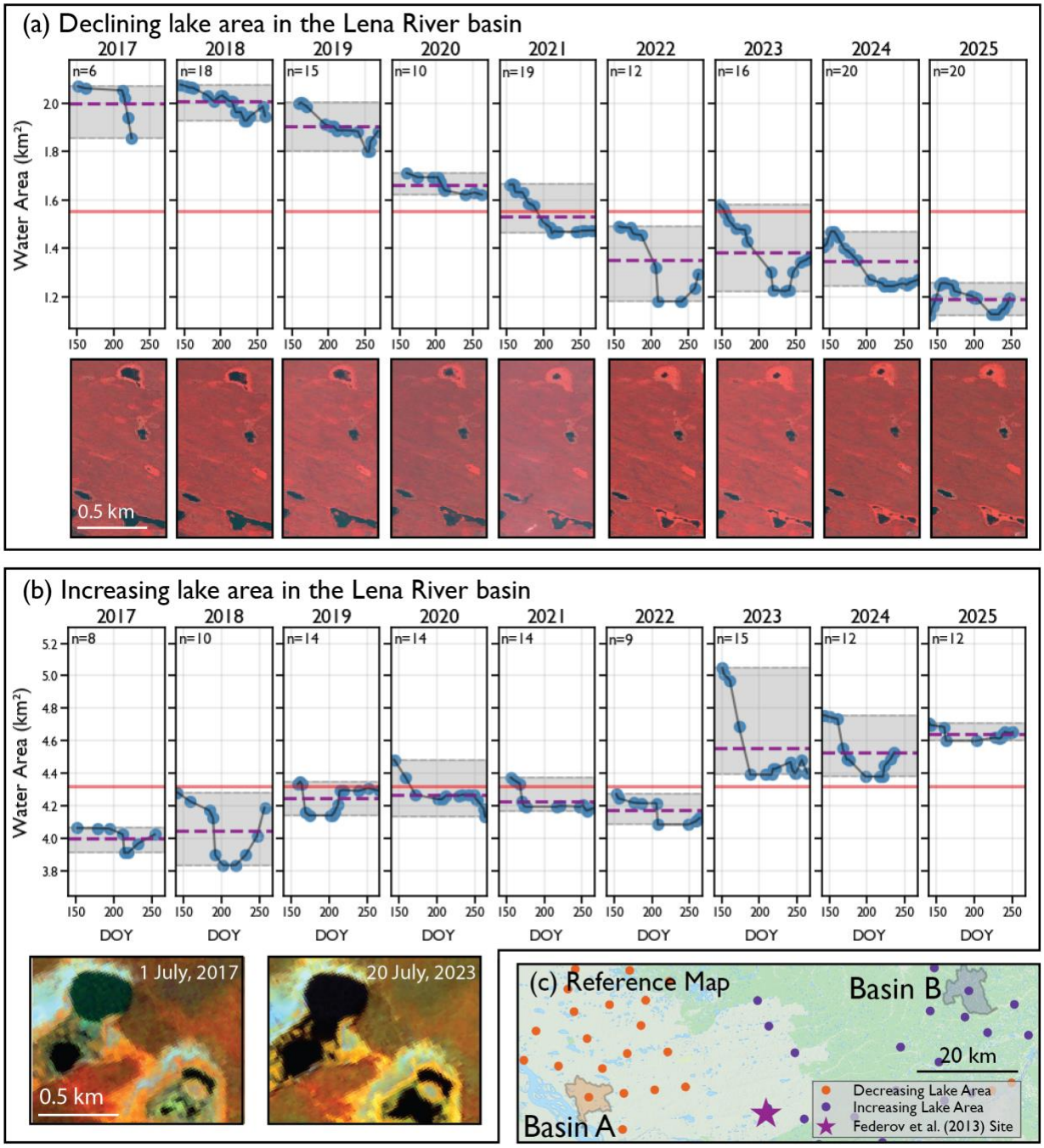

Figure 3.6: Diverging lake area trends (a-b) observed under similar climate constraints in thermokarst terrain within the Lena River watershed (c).

4.3 Lake Extent Responses to Earlier Snowmelt

Our analysis of basins with high interannual variability in snow disappearance date shows that peak lake area timing is coupled to temporal changes in snowmelt timing ($R^2 = 0.58$; $p < 0.001$, Figure 3.7). Surprisingly, maximum lake area and total seasonal variability do not consistently vary with snowmelt timing in the aggregate (Figure 3.7a), although mean ice-free lake area and drawdown duration are both sensitive to snowmelt timing. After stratifying basins into those with positive and negative correlations between snowmelt timing and maximum lake area (Figures 3.7b and 3.7c), we find that the decreased mean lake area response to earlier snowmelt is independent of the effect on maximum lake area. This suggests that snowmelt timing influences summer lake area through multiple mechanisms. Due to the confounding relationship between snowmelt timing and snow water equivalent (SWE), we expected later snowmelt to be associated with increased maximum and mean lake area, which is reflected in Figure 3.7b. However, 58% of basins show the opposite relationship where later snowmelt is associated with decreased maximum lake area (Figure 3.7c). Previous work has demonstrated that early snowmelt can increase the snowpack runoff ratio due to decreased plant available water storage, energy for sublimation, and infiltration into frozen ground (Barnhart et al., 2020). Therefore, we attribute the decreasing mean lake area with earlier snowmelt shown in Figure 3.7c to a shift in timing rather than water inputs. By shifting lake area peak and drawdown earlier into the summer, earlier snowmelt can increase the proportion of the ice-free season that lakes are near their minimum extent (Figure 3.8).

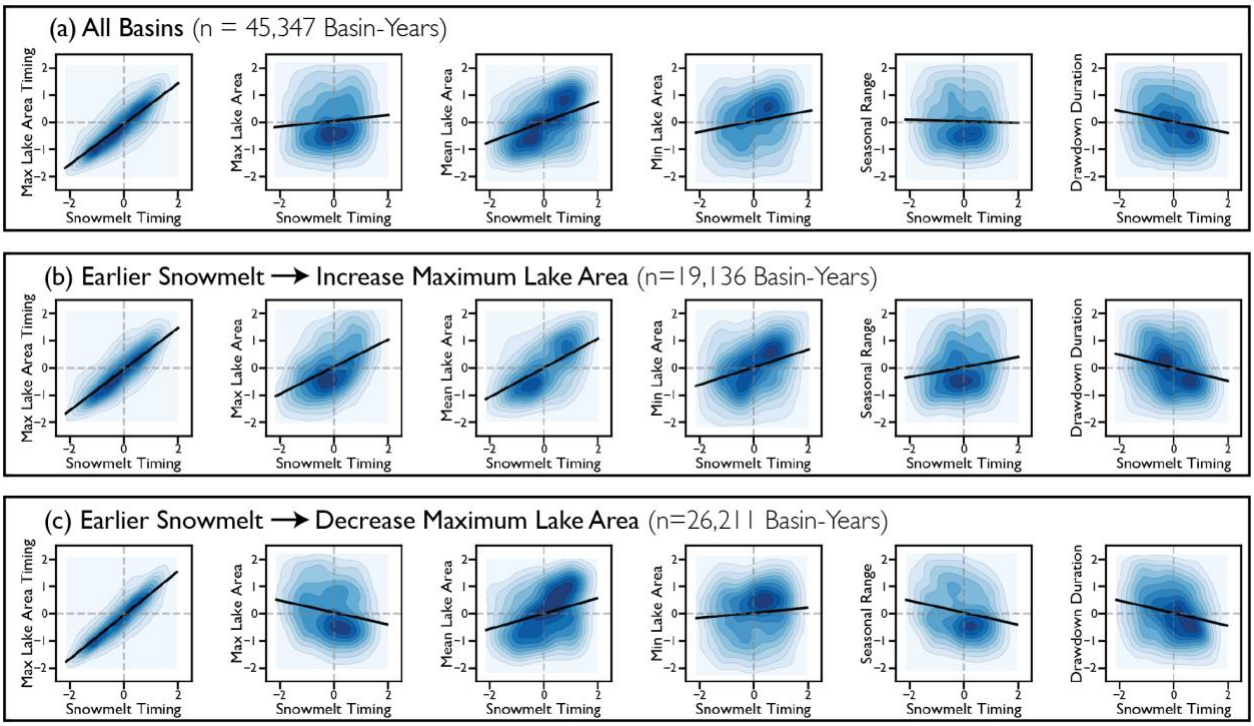

Figure 3.7: Lake area responses to snowmelt timing anomalies for (a) all basins with significant snowmelt timing variability and sufficient observational coverage. The data are then stratified into basins with (b) positive and (c) negative correlations between snowmelt timing and maximum lake area.

5. Discussion

Our Sentinel-2 lake area mapping effort for the pan-Arctic region allows us to identify dynamics spanning sub-seasonal to interannual temporal scales, and watershed to regional spatial scales. We find that Sentinel-2 optimizes the tradeoff between spatial and temporal resolution for this scope of investigation. For example, coarser spatial resolution imagery such as MODIS and Landsat would likely struggle to identify many of the trends we observe in thermokarst terrain where regionally significant changes to permafrost conditions are expressed through very fine-scale shoreline fluctuations (e.g., Figure 3.6; Cooley et al., 2019; Fedorov et al., 2014; Mullen et al., 2023). With 10 m resolution imagery, we are able to observe dynamics previously revealed by focused field and remote sensing studies (Fedorov et al., 2014; Nitze et al., 2020) and contextualize these findings within the entire Arctic.

The sub-seasonal frequency of our observations is also critical for understanding Arctic lake dynamics. Sentinel-2's mean (median) revisit frequency of 6.7 (5.9) days after cloud masking approaches the reported 5-day functional temporal resolution of lake tracking studies using commercial Planet data (Cooley et al., 2019). We find similar patterns of seasonal drawdown as focused seasonality studies owing to the dominance of melt processes in driving lake area change. We also observe spatial differences in the timing, rate, and magnitude of this drawdown, as well as contrasting lake seasonality regimes likely driven by late-season inputs from glaciers, alpine snowmelt, and human management. The spatiotemporal resolution of our approach is able to capture the dominant seasonal lake area progression but struggles to resolve the influence of individual summertime precipitation events. Future work incorporating radar imagery and altimetry, such as Surface Water and Ocean Topography (SWOT) data (Biancamaria et al., 2016), may enhance our ability to detect lake responses to precipitation and a potential regime shift from snowmelt to rainfall-runoff hydrologic behavior.

We observe that the timing of snowmelt has a cascading impact on lake area dynamics well into the summer. First, the timing of maximum lake area is strongly coupled to snowmelt timing. This finding alone has significant implications for time-sensitive phenological relationships and regional ecology (Wrona et al., 2016), particularly given the evidence that snowmelt will occur earlier in the future (Overland et al., 2014). Isolating the influence of snowmelt timing from the magnitude of SWE is difficult without in situ data. However, by deconstructing lake area responses into individual components (i.e., seasonal maximum, minimum, and mean lake area), our results suggest that earlier snowmelt can decrease mean lake area independently of changes to SWE (Figures 3.7 and 3.8). Given an equivalent water supply but earlier melt, maximum and minimum lake area may remain constant. However, an earlier peak and drawdown will cause mean lake area to decrease because a larger fraction of the open water season will be near the minimum lake area (Figure 3.8). That basins with negative correlations between snowmelt timing and maximum lake area anomalies still have positive correlations between snowmelt timing and mean lake area (Figure 3.7c) provides another line of evidence in support of this 'seasonal drift' hypothesis.

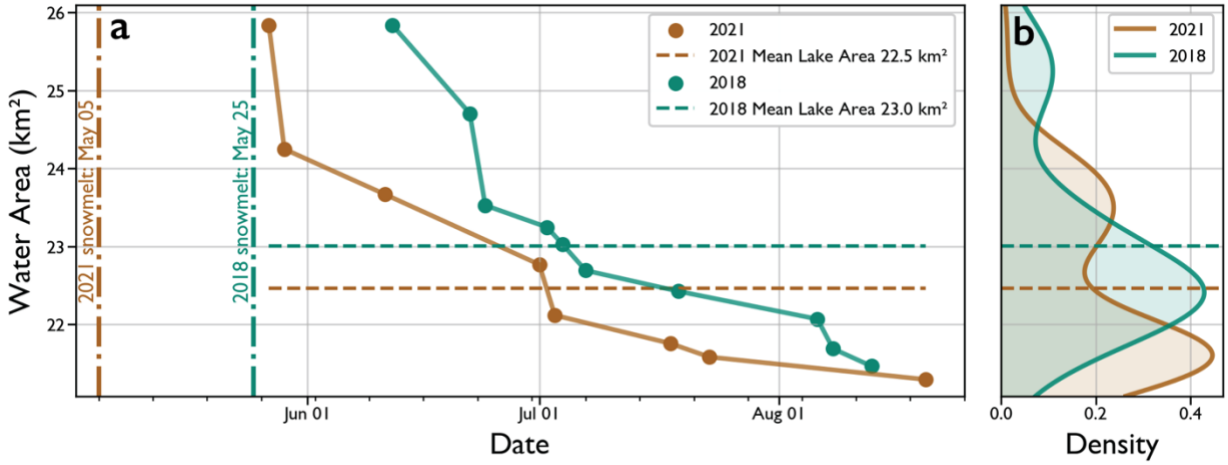

Figure 3.8: Example of 'seasonal drift' through a comparison of a basin's lake area progression (a) and seasonal distribution (b) following the 2021 early (negative) snowmelt timing anomaly and the 2018 late (positive) snowmelt timing anomaly.

Changes to the timing of lake seasonality have significant implications for the practice of using interannual lake area trends to infer permafrost conditions or thermokarst erosion. Gradual decreases in lake area have previously been interpreted as either a hydrologic signal (i.e., decreasing water balance), an ecological signal (e.g., terrestrialization), or increased hydrologic connectivity under permafrost thaw (Walvoord & Kurylyk, 2016). In addition to these potential causes, we suggest that seasonal drift should also be posed as a hypothesis to explain observed lake area decline. If snowmelt timing advances over time, a fixed mid-summer sampling window will progressively capture lakes at a later stage of their seasonal drawdown, thus producing an apparent trend in declining mean lake area even if the total water storage remains unchanged. Our results suggest that the magnitude of this shift is sufficient to produce measurable changes in mean ice-free lake area.

6. Conclusion and Bridge

By mapping pan-Arctic lake extent at sub-seasonal to nearly decadal time scales at 10 m spatial resolution, our analysis represents a significant contribution to our understanding of

Arctic lake dynamics. Typical seasonal variability represents 62% of the total lake area change that occurred over nine years. These intra-annual dynamics are primarily characterized by an initial pulse from the spring freshet followed by a gradual drawdown. The timing of this pulse and drawdown pattern varies spatially and across years due to snowmelt timing, which also influences average lake area during the ice-free summer season. We observe multiple mechanisms driving lake area declines including lake drainage and vegetation infilling, as well as lake area increases including thermokarst lake expansion and seasonal refilling of drained lake basins. Moving forward, high spatiotemporal resolution data should be considered the standard for tracking lake area dynamics in the Arctic region given its compressed seasonal timeline and the interactions between intra- and interannual variability. In Chapter IV, we incorporate satellite altimetry data from the SWOT mission to advance analyses from tracking lake area to lake water storage, thus significantly improving our ability to monitor hydrologic change and discriminate between potential mechanisms.

References

Adrian, R., O'Reilly, C. M., Zagarese, H., Baines, S. B., Hessen, D. O., Keller, W., Livingstone, D. M., Sommaruga, R., Straile, D., Van Donk, E., Weyhenmeyer, G. A., & Winder, M. (2009). Lakes as sentinels of climate change. *Limnology and Oceanography*, *54*(6part2), 2283–2297. https://doi.org/10.4319/lo.2009.54.6_part_2.2283

Algesten, G., Sobek, S., Bergström, A., Ågren, A., Tranvik, L. J., & Jansson, M. (2004). Role of lakes for organic carbon cycling in the boreal zone. *Global Change Biology*, *10*(1), 141–147. https://doi.org/10.1111/j.1365-2486.2003.00721.x

Arp, C. D., Jones, B. M., Hinkel, K. M., Kane, D. L., Whitman, M. S., & Kemnitz, R. (2020). Recurring outburst floods from drained lakes: An emerging Arctic hazard. *Frontiers in Ecology and the Environment*, *18*(7), 384–390. https://doi.org/10.1002/fee.2175

Barnhart, T. B., Tague, C. L., & Molotch, N. P. (2020). The Counteracting Effects of Snowmelt Rate and Timing on Runoff. *Water Resources Research*, *56*(8), e2019WR026634. https://doi.org/10.1029/2019WR026634

Biancamaria, S., Lettenmaier, D. P., & Pavelsky, T. M. (2016). The SWOT Mission and Its Capabilities for Land Hydrology. In A. Cazenave, N. Champollion, J. Benveniste, & J. Chen (Eds.), *Remote Sensing and Water Resources* (pp. 117–147). Springer International Publishing. https://doi.org/10.1007/978-3-319-32449-4_6

Bring, A., Fedorova, I., Dibike, Y., Hinzman, L., Mård, J., Mernild, S. H., Prowse, T., Semenova, O., Stuefer, S. L., & Woo, M.-K. (2016). Arctic terrestrial hydrology: A synthesis of processes, regional effects, and research challenges. *Journal of Geophysical Research: Biogeosciences*, *121*(3), 621–649. https://doi.org/10.1002/2015JG003131

Carroll, M. L., Townshend, J. R. G., DiMiceli, C. M., Loboda, T., & Sohlberg, R. A. (2011). Shrinking lakes of the Arctic: Spatial relationships and trajectory of change: SHRINKING LAKES OF THE ARCTIC. *Geophysical Research Letters*, *38*(20), n/a-n/a. https://doi.org/10.1029/2011GL049427

Cooley, S. W., Smith, L. C., Ryan, J. C., Pitcher, L. H., & Pavelsky, T. M. (2019). Arctic-Boreal Lake Dynamics Revealed Using CubeSat Imagery. *Geophysical Research Letters*, *46*(4), 2111–2120. https://doi.org/10.1029/2018GL081584

Cooley, S. W., Smith, L. C., Stepan, L., & Mascaro, J. (2017). Tracking Dynamic Northern Surface Water Changes with High-Frequency Planet CubeSat Imagery. *Remote Sensing*, *9*(12), Article 12. https://doi.org/10.3390/rs9121306

Cooley, S.W., Webb, E.E., Levenson, E.S., Ryan, J.C. (in review). Lakes modify the magnitude and timing of the Northern Hemisphere Terrestrial Cryosphere Radiative Effect.

Fedorov, A. N., Gavriliev, P. P., Konstantinov, P. Y., Hiyama, T., Iijima, Y., & Iwahana, G. (2014). Estimating the water balance of a thermokarst lake in the middle of the Lena River basin, eastern Siberia. *Ecohydrology*, *7*(2), 188–196. https://doi.org/10.1002/eco.1378

Foster, J. L., Cohen, J., Robinson, D. A., & Estilow, T. W. (2013). A look at the date of snowmelt and correlations with the Arctic Oscillation. *Annals of Glaciology*, *54*(62), 196–204. https://doi.org/10.3189/2013AoG62A090

Franz, D., Mammarella, I., Boike, J., Kirillin, G., Vesala, T., Bornemann, N., Larmanou, E., Langer, M., & Sachs, T. (2018). Lake-Atmosphere Heat Flux Dynamics of a Thermokarst Lake in Arctic Siberia. *Journal of Geophysical Research: Atmospheres*, *123*(10), 5222–5239. https://doi.org/10.1029/2017JD027751

Gorelick, N., Hancher, M., Dixon, M., Ilyushchenko, S., Thau, D., & Moore, R. (2017). Google Earth Engine: Planetary-scale geospatial analysis for everyone. *Remote Sensing of Environment*, *202*, 18–27. https://doi.org/10.1016/j.rse.2017.06.031

Hall, D. K., & Riggs, G. A. (2021). *MODIS/Terra Snow Cover Daily L3 Global 500m SIN Grid, Version 61* [Dataset]. NASA National Snow and Ice Data Center Distributed Active Archive Center. https://doi.org/10.5067/MODIS/MOD10A1.061

Lehner, B., & Grill, G. (2013). Global river hydrography and network routing: Baseline data and new approaches to study the world's large river systems. *Hydrological Processes*, *27*(15), 2171–2186. https://doi.org/10.1002/hyp.9740

Lesack, L. F. W., & Marsh, P. (2010). River-to-lake connectivities, water renewal, and aquatic habitat diversity in the Mackenzie River Delta. *Water Resources Research*, *46*(12), 2010WR009607. https://doi.org/10.1029/2010WR009607

Levenson, E. S., Cooley, S., Mullen, A., Webb, E. E., & Watts, J. (2025). Glacial History Modifies Permafrost Controls on the Distribution of Lakes and Ponds. *Geophysical Research Letters*, *52*(4), e2024GL112771. https://doi.org/10.1029/2024GL112771

Levenson, E.S., Cooley, S., Wang, J., Trudel, M. (In Prep). Assessing SWOT capabilities and limitations for water storage monitoring in lakes.

Li, L., Long, D., Wang, Y., & Woolway, R. I. (2025). Global dominance of seasonality in shaping lake-surface-extent dynamics. *Nature*, *642*(8067), 361–368. https://doi.org/10.1038/s41586-025-09046-3

McClelland, J. W., Holmes, R. M., Peterson, B. J., & Stieglitz, M. (2004). Increasing river discharge in the Eurasian Arctic: Consideration of dams, permafrost thaw, and fires as potential agents of change. *Journal of Geophysical Research: Atmospheres*, *109*(D18), 2004JD004583. https://doi.org/10.1029/2004JD004583

McFEETERS, S. K. (1996). The use of the Normalized Difference Water Index (NDWI) in the delineation of open water features. *International Journal of Remote Sensing*, *17*(7), 1425–1432. https://doi.org/10.1080/01431169608948714

Mullen, A. L., Watts, J. D., Rogers, B. M., Carroll, M. L., Elder, C. D., Noomah, J., Williams, Z., Caraballo-Vega, J. A., Bredder, A., Rickenbaugh, E., Levenson, E., Cooley, S. W., Hung, J. K. Y., Fiske, G., Potter, S., Yang, Y., Miller, C. E., Natali, S. M., Douglas, T. A., & Kyzivat, E. D. (2023). Using High-Resolution Satellite Imagery and Deep Learning to Track Dynamic Seasonality in Small Water Bodies. *Geophysical Research Letters*, *50*(7), e2022GL102327. https://doi.org/10.1029/2022GL102327

Muñoz-Sabater, J., Dutra, E., Agustí-Panareda, A., Albergel, C., Arduini, G., Balsamo, G., Boussetta, S., Choulga, M., Harrigan, S., Hersbach, H., Martens, B., Miralles, D. G., Piles, M., Rodríguez-Fernández, N. J., Zsoter, E., Buontempo, C., & Thépaut, J.-N. (2021). ERA5-Land: A state-of-the-art global reanalysis dataset for land applications. *Earth System Science Data*, *13*(9), 4349–4383. https://doi.org/10.5194/essd-13-4349-2021

Nitze, I., Cooley, S. W., Duguay, C. R., Jones, B. M., & Grosse, G. (2020). The catastrophic thermokarst lake drainage events of 2018 in northwestern Alaska: Fast-forward into the future. *The Cryosphere*, *14*(12), 4279–4297. https://doi.org/10.5194/tc-14-4279-2020

Nitze, I., Grosse, G., Jones, B., Arp, C., Ulrich, M., Fedorov, A., & Veremeeva, A. (2017). Landsat-Based Trend Analysis of Lake Dynamics across Northern Permafrost Regions. *Remote Sensing*, *9*(7), 640. https://doi.org/10.3390/rs9070640

Overland, J. E., Wang, M., Walsh, J. E., & Stroeve, J. C. (2014). Future Arctic climate changes: Adaptation and mitigation time scales. *Earth's Future*, *2*(2), 68–74. https://doi.org/10.1002/2013EF000162

Pletcher, A., Cooley, S. W., & Levenson, E. (2025). Observing Fine-Scale Lake Ice-Out Dynamics in the Lower Kuskokwim River Basin, Alaska. *Hydrological Processes*, *39*(11), e70309. https://doi.org/10.1002/hyp.70309

Prowse, T., Alfredsen, K., Beltaos, S., Bonsal, B. R., Bowden, W. B., Duguay, C. R., Korhola, A., McNamara, J., Vincent, W. F., Vuglinsky, V., Walter Anthony, K. M., & Weyhenmeyer, G. A. (2011). Effects of Changes in Arctic Lake and River Ice. *AMBIO*, *40*(1), 63–74. https://doi.org/10.1007/s13280-011-0217-6

Rantanen, M., Karpechko, A. Y., Lipponen, A., Nordling, K., Hyvärinen, O., Ruosteenoja, K., Vihma, T., & Laaksonen, A. (2022). The Arctic has warmed nearly four times faster than the globe since 1979. *Communications Earth & Environment*, *3*(1), Article 1. https://doi.org/10.1038/s43247-022-00498-3

Rawlins, M. A., & Karmalkar, A. V. (2024). Regime shifts in Arctic terrestrial hydrology manifested from impacts of climate warming. *The Cryosphere*, *18*(3), 1033–1052. https://doi.org/10.5194/tc-18-1033-2024

Rawlins, M. A., Steele, M., Holland, M. M., Adam, J. C., Cherry, J. E., Francis, J. A., Groisman, P. Y., Hinzman, L. D., Huntington, T. G., Kane, D. L., Kimball, J. S., Kwok, R., Lammers, R. B., Lee, C. M., Lettenmaier, D. P., McDonald, K. C., Podest, E., Pundsack, J. W., Rudels, B., … Zhang, T. (2010). Analysis of the Arctic System for Freshwater Cycle Intensification: Observations and Expectations. *Journal of Climate*, *23*(21), 5715–5737. https://doi.org/10.1175/2010JCLI3421.1

Riordan, B., Verbyla, D., & McGuire, A. D. (2006). Shrinking ponds in subarctic Alaska based on 1950–2002 remotely sensed images. *Journal of Geophysical Research: Biogeosciences*, *111*(G4), 2005JG000150. https://doi.org/10.1029/2005JG000150

Roach, J., Griffith, B., Verbyla, D., & Jones, J. (2011). Mechanisms influencing changes in lake area in Alaskan boreal forest: MECHANISMS FOR LAKE AREA CHANGE IN ALASKA. *Global Change Biology*, *17*(8), 2567–2583. https://doi.org/10.1111/j.1365-2486.2011.02446.x

Saros, J. E., Arp, C. D., Bouchard, F., Comte, J., Couture, R.-M., Dean, J. F., Lafrenière, M., MacIntyre, S., McGowan, S., Rautio, M., Prater, C., Tank, S. E., Walvoord, M., Wickland, K. P., Antoniades, D., Ayala-Borda, P., Canario, J., Drake, T. W., Folhas, D., … Vincent, W. F. (2023). Sentinel responses of Arctic freshwater systems to climate: Linkages, evidence, and a roadmap for future research. *Arctic Science*, *9*(2), 356–392. https://doi.org/10.1139/as-2022-0021

Schindler, D. W. (2009). Lakes as sentinels and integrators for the effects of climate change on watersheds, airsheds, and landscapes. *Limnology and Oceanography*, *54*(6part2), 2349–2358. https://doi.org/10.4319/lo.2009.54.6_part_2.2349

Schwehr, K. (2020). *Sentinel-2: Cloud Probability in Earth Engine* (Version 1) [Dataset]. Zenodo. https://doi.org/10.5281/ZENODO.7411046

Semmens, K. A., Ramage, J., Bartsch, A., & Liston, G. E. (2013). Early snowmelt events: Detection, distribution, and significance in a major sub-arctic watershed. *Environmental Research Letters*, *8*(1), 014020. https://doi.org/10.1088/1748-9326/8/1/014020

Smith, L. C., Sheng, Y., & MacDonald, G. M. (2007). A first pan-Arctic assessment of the influence of glaciation, permafrost, topography and peatlands on northern hemisphere lake distribution. *Permafrost and Periglacial Processes*, *18*(2), 201–208. https://doi.org/10.1002/ppp.581

Smith, L. C., Sheng, Y., MacDonald, GM., & Hinzman, L. D. (2005). Disappearing Arctic Lakes. *Science*, *308*. https://www.science.org/doi/full/10.1126/science.1108142?casa_token=d5ccuMO-1s8AAAAA%3ARdITjR7YHWYfpzCo07dLrWtWbnSndF0LpGBPrau-jALGVq7UtQKkreECoV7tbh56llGjm-RtuBwknw

Su, Y., Ran, Y., Zhang, G., & Li, X. (2023). Remotely sensed lake area changes in permafrost regions of the Arctic and the Tibetan Plateau between 1987 and 2017. *Science of The Total Environment*, *880*, 163355. https://doi.org/10.1016/j.scitotenv.2023.163355

Tan, A., Adam, J. C., & Lettenmaier, D. P. (2011). Change in spring snowmelt timing in Eurasian Arctic rivers. *Journal of Geophysical Research*, *116*(D3), D03101. https://doi.org/10.1029/2010JD014337

Tranvik, L. J., Downing, J. A., Cotner, J. B., Loiselle, S. A., Striegl, R. G., Ballatore, T. J., Dillon, P., Finlay, K., Fortino, K., Knoll, L. B., Kortelainen, P. L., Kutser, T., Larsen, Soren., Laurion, I., Leech, D. M., McCallister, S. L., McKnight, D. M., Melack, J. M., Overholt, E., … Weyhenmeyer, G. A. (2009). Lakes and reservoirs as regulators of carbon cycling and climate. *Limnology and Oceanography*, *54*(6part2), 2298–2314. https://doi.org/10.4319/lo.2009.54.6_part_2.2298

Walsh, R. P. D., & Lawler, D. M. (1981). RAINFALL SEASONALITY: DESCRIPTION, SPATIAL PATTERNS AND CHANGE THROUGH TIME. *Weather*, *36*(7), 201–208. https://doi.org/10.1002/j.1477-8696.1981.tb05400.x

Walter Anthony, K., Daanen, R., Anthony, P., Schneider Von Deimling, T., Ping, C.-L., Chanton, J. P., & Grosse, G. (2016). Methane emissions proportional to permafrost carbon thawed in Arctic lakes since the 1950s. *Nature Geoscience*, *9*(9), 679–682. https://doi.org/10.1038/ngeo2795

Walvoord, M. A., & Kurylyk, B. L. (2016). Hydrologic Impacts of Thawing Permafrost—A Review. *Vadose Zone Journal*, *15*(6), vzj2016.01.0010. https://doi.org/10.2136/vzj2016.01.0010

Wang, J., Pottier, C., Cazals, C., Battude, M., Sheng, Y., Song, C., Sikder, M. S., Yang, X., Ke, L., Delhoume, M., Gosset, M., Oliveira, R. R. A., Grippa, M., Girard, F., Allen, G. H., Xu, X., Zhu, X., Biancamaria, S., Smith, L. C., … Pavelsky, T. M. (2025). The Surface Water and Ocean Topography Mission (SWOT) Prior Lake Database (PLD): Lake Mask and Operational Auxiliaries. *Water Resources Research*, *61*(3), e2023WR036896. https://doi.org/10.1029/2023WR036896

Webb, E. E., & Liljedahl, A. K. (2023). Diminishing lake area across the northern permafrost zone. *Nature Geoscience*, *16*(3), 202–209. https://doi.org/10.1038/s41561-023-01128-z

Webb, E. E., Loranty, M. M., & Lichstein, J. W. (2021). Surface water, vegetation, and fire as drivers of the terrestrial Arctic-boreal albedo feedback. *Environmental Research Letters*, *16*(8), 084046. https://doi.org/10.1088/1748-9326/ac14ea

Wrona, F. J., Johansson, M., Culp, J. M., Jenkins, A., Mård, J., Myers-Smith, I. H., Prowse, T. D., Vincent, W. F., & Wookey, P. A. (2016). Transitions in Arctic ecosystems: Ecological implications of a changing hydrological regime. *Journal of Geophysical Research: Biogeosciences*, *121*(3), 650–674. https://doi.org/10.1002/2015JG003133

CHAPTER IV
ASSESSING SWOT CAPABILITIES AND LIMITATIONS FOR WATER STORAGE MONITORING IN LAKES

1. Introduction

The amount of water stored in lakes and reservoirs fluctuates in response to anthropogenic and hydroclimatic processes, generating profound consequences for human communities, ecosystems, and climate feedbacks (Cooley et al., 2021; Fergus et al., 2022; Tranvik et al., 2009). Understanding and predicting these dynamics is highly dependent on observing water storage change in sufficient detail. Given the limited availability of in situ storage data, satellite-based water storage observations are widely recognized as essential to advancing hydrologic sciences, closing the terrestrial water budget, and supporting water management decisions (Alsdorf et al., 2007). After decades of effort to develop this capability, the Surface Water and Ocean Topography (SWOT) mission launched in December 2022 with an explicit objective to measure water storage change globally (Biancamaria et al., 2016).

SWOT is specifically designed to address key technical challenges of water storage remote sensing. Observing storage from space fundamentally depends on establishing each lake's water surface Area-Elevation (AE) relationship to measure volumetric changes. Previous satellite-based approaches have quantified storage trends in large lakes (Yao et al., 2023) and identified management characteristics in reservoirs (Li et al., 2023), among many other notable contributions (Birkett et al., 2018; Bonnema et al., 2016; Gao et al., 2012; Tortini et al., 2020; Zhong et al., 2020). However, the characteristics of conventional satellite imagery and altimetry produce a tradeoff between the accuracy, frequency, and spatial coverage of water volume measurements that limits both their global-scale applicability and utility (Alsdorf et al., 2007; Cooley et al., 2025). By necessity, these existing approaches merge asynchronous observations from multiple sensors and generally use WSA measurements to estimate storage, whereas SWOT directly measures surface water in three-dimensions. This technical breakthrough is made possible by a Ka-band radar interferometer (KaRIn) onboard SWOT, which is the first wide-swath altimeter in space. From KaRIn, SWOT provides simultaneous measurements of water surface elevation (WSE) and area (WSA) in lakes globally with an average revisit time of 11

days (Peral & Esteban-Fernandez, 2018). Using this data, it is now possible to produce AE relationships from a single sensor and use its time series to estimate relative water storage in most lakes globally moving forward. SWOT has already been used to map water level and extent in lakes as small as 250 m^2 (Fu et al., 2024), observe flood waves (Thurman et al., 2025), and measure the slope of rivers and large lakes (Dhote et al., 2025).

While SWOT provides a potentially transformative new source of information to test scientific hypotheses or support water management (Vinogradova et al., 2025), several outstanding issues related to SWOT data processing and measurement accuracy must be resolved to fully understand its water storage monitoring capabilities and support widespread adoption. First, there is no consensus on how to filter SWOT data to balance accuracy against temporal resolution. Due to data quality issues, each preliminary SWOT study has developed an ad hoc data filtering technique prior to calculating measurement error metrics, including manually selecting high-quality observations (Fu et al., 2024), masking at the pixel level using varying criteria (Das & Hossain, 2025; Girard et al., 2025; Maubant et al., 2025; Ming et al., 2025), and discarding observations based on outlier rejection (Bazzi et al., 2025; Hamoudzadeh et al., 2024), SWOT's quality flags (Bazzi et al., 2025; Girard et al., 2025) or the spread of intra-lake WSE measurements (Das & Hossain, 2025; Maubant et al., 2025).The impact of these filtering choices on measurement accuracy and temporal resolution has not been systematically evaluated, obscuring SWOT's true performance and potentially leaving data underexploited. Second, SWOT's accuracy in measuring WSA remains poorly characterized relative to the stated science requirements. Girard et al. (2025) found significant WSA overestimations in 16 small and medium-sized lakes in West Africa, which prevented the construction of SWOT-based AE curves. Finally, SWOT's effective observation frequency, itself dependent on the filtering approach, is not spatially or temporally consistent. Therefore, full characterization of SWOT's water management and science capabilities also requires assessing how SWOT's irregular, discrete sampling scheme affects SWOT's ability to observe storage fluctuations.

Here, we address fundamental questions regarding SWOT lake observations in order to better understand SWOT's utility for water storage monitoring. To do this, we present a dataset of 411 gauged lakes and reservoirs with over 21,000 paired SWOT, Sentinel-2, and gauge observations from July 2023 to October 2025. Using this benchmark dataset, we are able to (a)

quantify the temporal resolution and accuracy of SWOT water level and area measurements in lakes; (b) estimate water storage changes and evaluate SWOT's ability to detect fluctuations of varying time-scales and magnitudes; (c) identify the sources of uncertainty in SWOT-based estimates of lake water storage change; and (d) integrate Sentinel-2 WSA measurements and evaluate the impact on water storage monitoring. Together, these insights enable us to identify opportunities to improve SWOT water storage monitoring performance and contextualize these results relative to gauges and existing remote sensing capabilities.

2. Methods

2.1 Study Site and Gauge Data

The benchmark dataset consists of 411 lakes and reservoirs that represent a range of morphological characteristics, physiographic settings, and hydrologic regimes. These water bodies were chosen for their diversity and associated publicly available water data from USGS, US Bureau of Reclamation, and the California Data Exchange. In situ water level data were downloaded from the start of the SWOT science orbit (July 21, 2023) until October 15, 2025 using the NWIS API, RISE API, and a custom web scraping script to access data from the California Data Exchange. We manually inspected time series and removed spurious observations and water bodies with data gaps exceeding 50% of the study period. We mapped gauge locations to the SWOT Prior Lake Database (PLD) using spatial intersection followed by manual confirmation. PLD provides static characteristics, such as lake size, ice climatology, and a unique identifier that is required to access SWOT data (Wang et al., 2025). We removed any water bodies exhibiting disagreement between PLD and gauges, such as gauged reservoirs that are split into multiple PLD lakes (e.g., Lake Shasta and Salt Lake). Our criteria reduced the overall dataset from 464 to 411 benchmark lakes.

2.2 Satellite Data

We focus our analysis on the SWOT LakeSP product given its optimization for hydrology objectives to monitor water storage globally at sub-monthly time scales. For each SWOT pass over a given lake, the LakeSP product provides observations of WSE and WSA by aggregating the SWOT pixel cloud (PIXC) data to polygons of known and observed lakes. We

downloaded each benchmark lake's LakeSP record for the science orbit from July 21, 2023 – October 12, 2025 using the Hydrocron API (Greguska et al., 2025), which delivers LakeSP time series for individual lakes. Each timestep includes SWOT measurements of lake elevation and extent, as well as ancillary quality flags and uncertainty estimates derived from the science data algorithms. We prioritized the most recent data version available for a given day, as analyzing the full SWOT data record of the science orbit currently requires the use of multiple data versions.

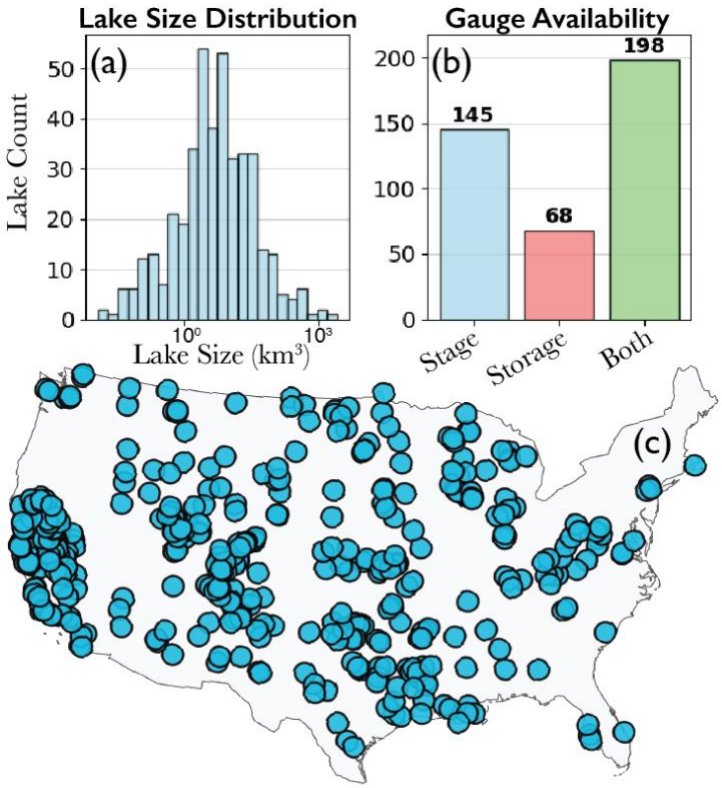

Figure 4.1: Benchmark dataset. (a) Lake size distribution from the SWOT Prior Lake Database (PLD). (b) Distribution of data type available from in situ gauge data. (c) Map of lake and reservoir in situ gauge sites.

Given known challenges with using SWOT WSA to estimate water storage (Girard et al., 2025), we also produced water surface area time series from Sentinel-2 optical satellite imagery to test whether the imagery's 10 m spatial resolution and nominal 5-day revisit can improve

water storage monitoring performance. After masking clouds and filtering images for full lake coverage, we classified water using an adaptive NDWI thresholding algorithm and calculated the water area on each date (Cooley et al., 2017; Levenson, et al., 2025). Previously, this method was shown to classify water with an F1 score of 0.999 (Levenson et al., 2025).

2.3 Measurement Error Calculations

We temporally matched each lake's gauge, SWOT, and Sentinel-2 measurements to calculate SWOT and Sentinel-2 WSE and WSA measurement errors against gauge observations. For monitoring water storage anomalies, the WSE uncertainty component is not affected by any temporally static offset. Therefore, we used SWOT and gauge WSE anomalies from their median observation based on dates with coincident gauge and SWOT observations. To remove the impact from differences in the median observation, we applied a bias correction using a systematic search for the constant bias within 2 m that maximizes the number of observations within 10 cm. WSE error is calculated as the residual between the bias-corrected SWOT LakeSP WSE anomalies (hereafter, SWOT WSE) and the gauge WSE anomaly.

We derived in situ daily water surface areas for the 198 in-situ gauges with both water level and storage data by fitting a unique stage – storage curve to each water body. We tested a linear and quadratic fit and selected the curve with the higher r^2:

$$\mathrm{V(wse)} = \mathrm{a_0} + \mathrm{a_1 wse} + \mathrm{a_2 wse^2}$$

Where *V* = storage volume, *wse* = water level.

Water surface area (WSA) was then calculated as the derivative of storage with respect to elevation:

$$\mathrm{WSA} = \frac{\mathrm{dV}}{\mathrm{dwse}} = \mathrm{a_1} + 2\mathrm{a_2 wse}$$

2.4 SWOT Data Filtering

To assess the impact of SWOT data filtering on measurement accuracy and temporal resolution, we first created an idealized filter based on the pre-launch SWOT science accuracy requirements (Peral & Esteban-Fernandez, 2018). This idealized filter allows us to assess SWOT performance if we had a 'perfect' method for removing poor-quality observations.

The filter uses actual SWOT observations and prior knowledge of measurement errors to extract the largest possible subset of observations that meets the requirement of 10 cm precision ($1\boldsymbol{\sigma}$). We used a basic search algorithm to find the maximum absolute WSE error threshold for the full sample of signed errors across all lakes. The idealized filter optimizes the tradeoff between accuracy and revisit frequency for our actual SWOT data, providing a reference to evaluate the retention rate, temporal resolution, and measurement uncertainty of functional filtering schemes.

To determine functional performance, we applied three SWOT data filtering approaches to the benchmark dataset and compared to the idealized filter. The first filter was the 'SWOT quality flag', which is the standard mission-provided filtering approach that has been used in numerous assessment studies. The threshold was defined as 'quality_f = 0'. The second 'simple' filter used thresholds applied to ancillary LakeSP quality flags and uncertainty fields based on descriptions within the SWOT user handbook. The 'simple' filter used the following thresholds: xovr_cal_q < 2; wse_std < 0.4; wse_u < .1; absolute WSE anomaly < 50. The last functional method was the 'adaptive' filter that used lake-specific calibrated quality thresholds and temporal smoothing (cite melanie trudel). To evaluate WSA measurements for each filter, we removed all partial observations (partial_f=0).

Using our benchmark gauge observations, we calculated WSE and WSA measurement error metrics such as RMSE, MAE, and $1\boldsymbol{\sigma}$ error for each of our filters. We also calculated each functional filter's precision and recall for classifying observations that pass the idealized filter as well as the temporal resolution (days per observation) of the filtered datasets.

2.5 Water Storage Calculations and Evaluation

To produce relative water storage time series for each lake, we built the AE curves with paired satellite-based observations of WSA and WSE. We fit linear and quadratic curves to the hypsometric relationship and selected the function with the higher R^2. Water storage anomalies were estimated for each WSE observation by incrementally evaluating the AE function in cross-sections spanning the range from the minimum to current water level. Next, we used a trapezoidal integration of area with respect to elevation to estimate water volume between cross-sections:

$$S(h) = \int_{wse_min}^{wse} A(z)dz$$

To test potential enhancements to SWOT water storage monitoring performance, we constructed AE curves between SWOT WSE and three different WSA data sources: SWOT, Sentinel-2 (S2), and static areas from PLD (Table 4.1). SWOT and S2 observations were temporally matched within a 3-day tolerance. Using the SWOT – S2 relationship, we created a fourth WSA-based water storage model that first estimated WSE from the S2 WSA time series by inverting the SWOT – S2 AE curve, before performing the same integration procedure to estimate volume. We converted each time series to storage anomalies from the median and compared to gauge-measured anomalies to calculate errors expressed in km^3 and percentage of variable storage capacity, defined as the range of gauge-measured storage during the study period.

Model	Time-Varying Input	Water Surface Area Source
SWOT	WSE (SWOT)	SWOT
SWOTS2	WSE (SWOT)	Sentinel-2
STATIC	WSE (SWOT)	PLD (Static Area)
S2	WSA (S2)	Sentinel-2

Table 4.1: Four models for calculating active water storage time series from SWOT and Sentinel-2.

We evaluated water storage monitoring performance in multiple ways. First, we simply computed the RMSE, MAE, and the Nash-Sutcliffe Efficiency (NSE) from the storage anomaly estimate residuals compared to in situ observations. The NSE is sensitive to signal variability, meaning the score captures when lake dynamics fall below SWOT's measurement noise (Figure 4.2). These metrics are oriented to SWOT's irregular, discrete sampling scheme rather than the underlying continuous hydrologic signal (Figure 4.2), reflecting WSE and WSA measurement uncertainty in isolation.

We extended our analysis to assess how temporal sampling influences the signal to noise ratio of SWOT water storage monitoring. First, we quantified SWOT's ability to detect water storage variability as a function of both time scale and magnitude of water level fluctuations. For

each lake, we randomly sampled 50 intervals ranging from 3 to 730 days. Within each interval, we extracted the range of WSE and storage anomalies observed by SWOT and the gauge. We then computed the ratio of SWOT-estimated water storage variability to the gauge-measured water storage variability. Second, we conducted a gap-filled analysis by interpolating the filtered SWOT-derived storage anomaly time series to daily resolution (Figure 4.2) and calculated the RMSE, MAE, and NSE against daily gauge observations. By introducing interpolation errors, this approach quantifies the information lost due to sampling gaps. The gap-filled analysis also provides a naïve baseline enabling comparison with daily water storage estimates from hydrologic models.

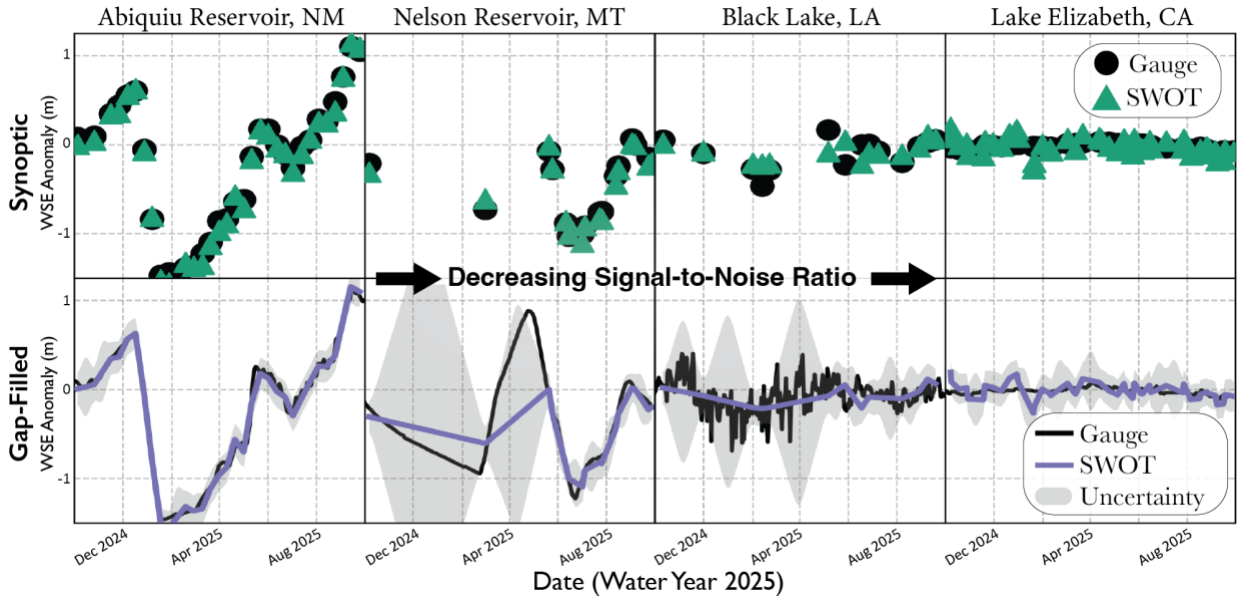

Figure 4.2: Example gauge and WSE anomaly time series using the idealized filter. The discrete evaluation framework is displayed in the top row, and the gap-filled, continuous evaluation is visualized in the bottom row with time-varying uncertainty shown in gray. The lakes show a left-to-right progression of decreasing NSE scores to demonstrate the influence of a lake's magnitude and frequency of water level fluctuations on the signal-to-noise ratio of SWOT storage anomaly time series.

2.6 Water Storage Uncertainty Decomposition

We used analytical, first-order error propagation to decompose total water storage estimate uncertainty (σ_S) into contributions from WSE measurement uncertainty (σ_{wse}) and WSA measurement uncertainty (σ_{wsa}). To define the sensitivity of storage to these uncertainty terms for each lake, we calculated analytical partial derivatives of the storage integral (Equation 2) with respect to each component. We defined WSE uncertainty using the prescribed σ_{wse} = 10 cm, and σ_{wsa} as the WSA RMSE after applying the idealized filter in Section 2.4. These terms were propagated to total storage uncertainty using:

$$\sigma^2{}_S = \left(\frac{\partial S}{\partial wse}\right)^2 \sigma^2{}_{wse} + \left(\frac{\partial S}{\partial wsa}\right)^2 \sigma^2{}_{wsa}$$

We extended the error propagation to include uncertainty due to temporal sampling (σ_t) and data filtering (σ_f):

$$\sigma^2{}_S = \left(\frac{\partial S}{\partial wse}\right)^2 (\sigma^2{}_{wse} + \sigma^2{}_t + \sigma^2{}_f) + \left(\frac{\partial S}{\partial wsa}\right)^2 (\sigma^2{}_{wsa} + \sigma^2{}_f)$$

Data filtering uncertainty (σ_f) represents the precision loss when using functional rather than idealized filters. The values were calculated by subtracting σ_{wse} and σ_{wsa} from the σ of signed errors for the functional filter calculated in section 2.4.

For discrete analyses, the temporal sampling uncertainty (σ_t) = 0. For daily, gap-filled time series, σ_t represents the interpolation error from sparse SWOT observations. To isolate interpolation errors, we masked the gauge-measured WSE time series to match the filtered SWOT observation timing. We then interpolated the sparse gauge time series back to daily resolution and analyzed the change in WSE uncertainty with distance from the nearest SWOT observation date. Sampling uncertainty increases with distance from SWOT observations, producing temporally variable WSE uncertainty (Figure 4.2). For the error propagation analysis, we parameterized σ_t as using a constant value calculated as the standard deviation of all interpolation errors. Each component's uncertainty contribution was calculated as the ratio of the component variance to the total predicted variance of storage estimates. We compared our total predicted uncertainty to observed water storage anomaly errors described in Section 2.5.

3. Results

3.1 Measurement Frequency and Accuracy

We find that SWOT's WSE and WSA measurement accuracy and temporal resolution vary significantly according to data filtering method. The idealized filter uses an absolute WSE error threshold of 28.4 cm to achieve the pre-defined WSE uncertainty of σ_{wse} = 10 cm, retaining 80.1% of observations and producing an average temporal resolution of 15.1 days per observation. By comparison, the temporal resolution of the unfiltered SWOT dataset matches the nominal revisit frequency of 11 days per observation with an RMSE of 19.46 meters due to the presence of outliers, introducing a tradeoff between revisit frequency and error tolerance (Figure 4.3f, Table 4.2). These temporal resolutions represent averages across revisit periods, but the actual sampling gap durations are irregular due to the SWOT orbit configuration (Figure 4.3e).

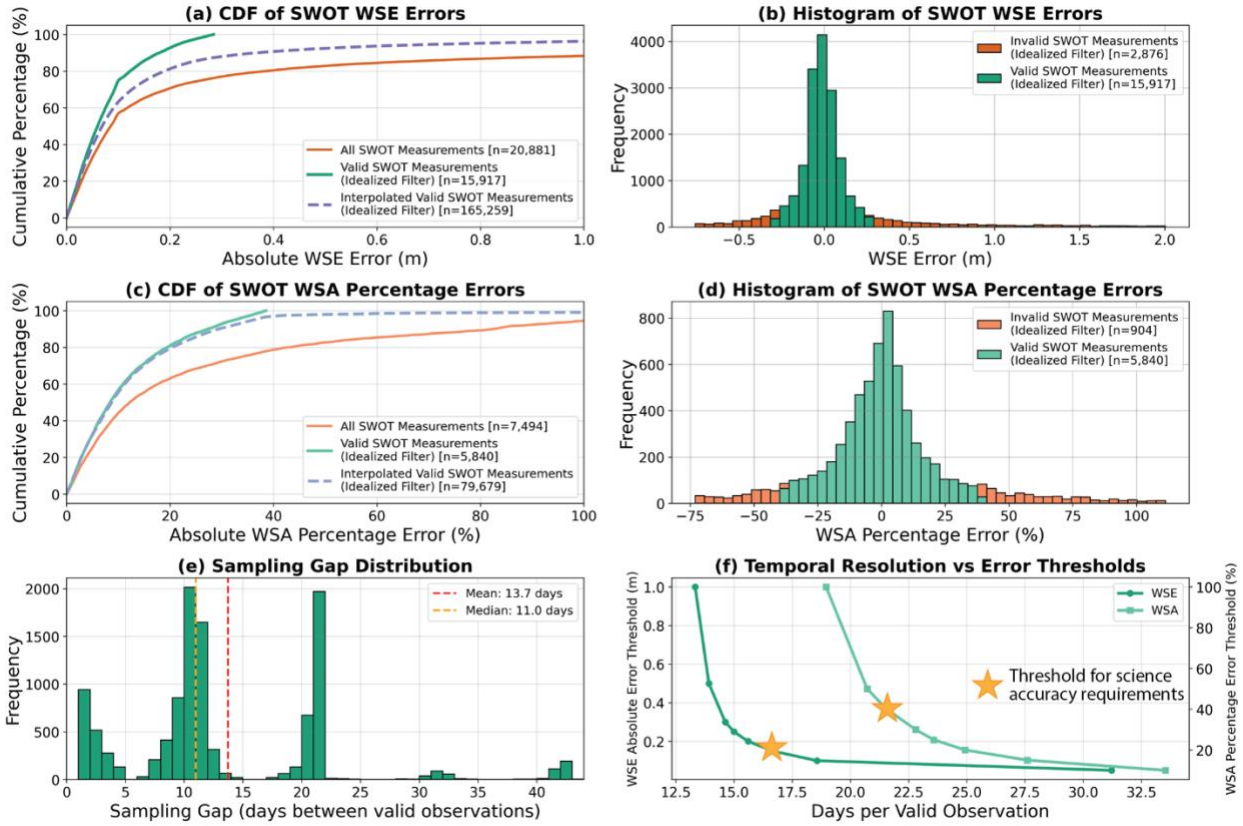

Figure 4.3: Idealized frequency and accuracy of SWOT WSE and WSA measurements. (a) CDF of absolute WSE errors for all ice-free SWOT observations, the idealized subset (i.e., observations meeting science accuracy requirements), and interpolated WSE errors. (b)

histograms comparing the full distribution vs. idealized subset of signed WSE errors. (c) CDF of WSA absolute errors. (d) histograms comparing the full vs. idealized subset of signed WSA errors. (e) histogram of sampling gap between observations meeting science accuracy requirements. (f) Tradeoff between temporal resolution and WSE error tolerance.

None of the functional filters achieved the science accuracy requirement of 1$\boldsymbol{\sigma}$ error = 10 cm due to the metric's sensitivity to outliers, with values ranging from 100 cm for 'Simple' to 372 cm for 'Quality_Flag' (Table 4.2). The 68th percentile of absolute errors (P68) are in much closer agreement to the 10 cm requirement with values ranging from 9 to 11 cm. Many SWOT analyses have used P68 as a proxy for the science requirement, but the order of magnitude difference between these error metrics indicates that the residuals are not normally distributed due to large outliers passing the functional filters (Extended Figure 1).

The adaptive and simple filters perform favorably compared to the SWOT quality flag in terms of both accuracy and data retention. The Adaptive filter has the highest data retention rate and is least likely to discard a valid observation, but the higher precision of the Simple filter results in a 12 cm reduction in the MAE (Table 4.2). Despite the tradeoff between uncertainty and frequency, both the Adaptive and Simple filters clearly track discrete WSE variability in most lakes, with median NSE scores of 0.93 and 0.94, respectively (Figure 5h). Hereafter, we use the Adaptive filter to compare SWOT's functional and idealized measurements for water storage monitoring performance due to its slightly higher median NSE score (0.64) for tracking daily WSE fluctuations compared to the Simple filter (0.61).

Filter	MAE (cm)	RMSE (cm)	68% |error| (cm)	1$\boldsymbol{\sigma}$ error (cm)	Precision	Recall	Retention Rate	Days per Observation	Median NSE
No Filter	211	1946	17	1935	0.75	1.00	1.00	11.7	-0.75
Idealized	8	10	9	10	1.00	1.00	0.76	15.1	0.99
Quality Flag	39	374	10	372	0.86	0.53	0.47	22.1	0.84
Simple	18	102	9	100	0.91	0.83	0.68	16.4	0.94
Adaptive	30	179	11	177	0.86	0.94	0.83	13.9	0.94

Table 4.2: Comparison of aggregated WSE errors and temporal resolution across filtering schemes.

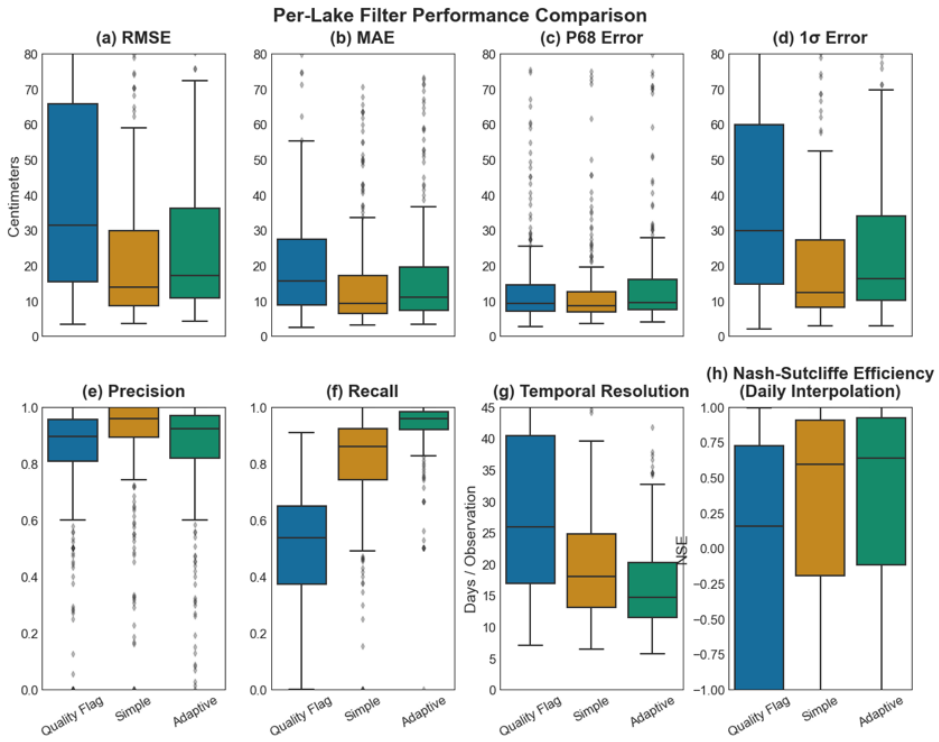

Figure 4.4: Comparison of WSE error metrics for functional filters. (a-d) show respective WSE error metrics. (e-f) report filter classification performance in identifying WSE measurements passing the idealized filter (absolute error less than 28.3 cm). (g) Temporal resolution of filtered observations. (h) NSE of WSE anomalies, with minimum values truncated for visualization.

As expected, SWOT provides notably fewer and less accurate WSA observations relative to WSE. The need to remove partial measurements reduces the average temporal resolution from 15 to 22 days per observation for the idealized filter. Independent of filter, SWOT WSA is more accurate relative to gauge data than a static area from PLD, primarily due to a significant negative bias in the PLD areas (Table A11). However, the relative errors ranging from 17% to 26% (MAE) and 31% to 63% (RMSE) generally exceed lakes' actual water area variability, leading to a positive NSE value in only 25% of our study lakes. By comparison, Sentinel-2 WSA measurements are significantly more frequent and accurate, producing a MAE of 3.6%, RMSE of 6.1%, and positive NSE values in 68% of lakes and an average temporal resolution of 6 days per observation. Compared to SWOT AE relationships, SWOT-S2 integration increases the

percentage of lakes with significant AE relationships from 52% to 79%, and the average r^2 from 0.29 to 0.51.

We used these error metrics to define input uncertainties for our error propagation procedure (Section 2.6). We defined the inherent WSE measurement uncertainty (σ_{wse}) as 10 cm, and additional WSE filtering uncertainty (σ_f) as 20 cm, reflecting the increase in WSE MAE between the idealized and adaptive filters. We isolated temporal sampling uncertainty (σ_t) by resampling gauge water levels to SWOT's schedule, interpolating to daily resolution, and calculating errors. This analysis indicates that WSE errors increase with distance from the nearest measurement at an approximate rate of 3 cm per day, with an overall MAE of 17 cm and RMSE of 40 cm. For each sensor, WSA measurement uncertainty (σ_{wsa}) is defined as the MAE for relative error (%) listed above, which we convert to km^2 for each lake's error propagation.

3.2. SWOT Water Storage Variability Detection

SWOT performance for detecting water storage variability is strongly dependent on time scale and the magnitude of water level fluctuations (Figure 4.5). Due to sampling gaps, SWOT underestimates storage change over sub-seasonal time scales. The probability of obtaining at least two valid SWOT observations increases with interval duration such that storage variability is completely undetected in 82% of 14-day intervals, 47% in 30-day intervals, 21% in 60-day intervals, and 14% in 90-day intervals. Over longer time periods and any intervals when SWOT does capture at least two valid observations, sampling gaps still introduce a negative bias in SWOT storage variability estimates due to unobserved local minimums and maximums. In contrast, random errors associated with measurement noise artificially increase estimates of water storage change over a given period, leading to overestimates of storage variability when the water level fluctuates less than 20 cm (Figure 4.5). On average, SWOT detects 75% of seasonal water storage variability and 84% of annual water storage variability.

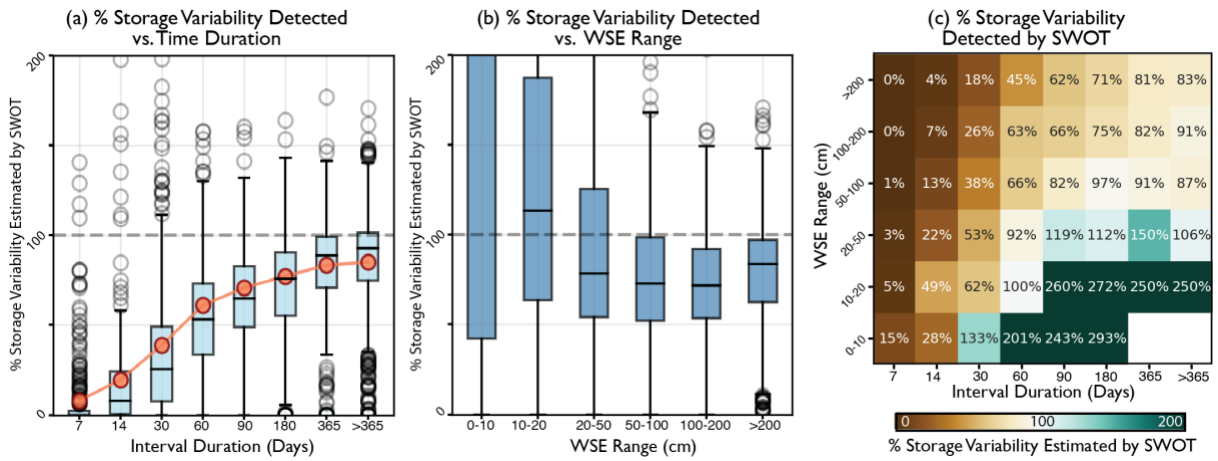

Figure 4.5: SWOT estimates of water storage variability across randomly sampled time series intervals. (a) Heatmap of the SWOT estimated water storage range expressed as a percentage of gauge measured water storage range, as a function of WSE range and time interval length. (b) Percent of the storage range detected by SWOT over varying time scales. (c) Percent of the storage range detected by SWOT as a function of actual WSE variability for samples with at least two SWOT observations. Y-axis is truncated to highlight the 100% threshold between over and underestimated storage variability.

Across the full study period for all lakes, we find that SWOT estimates discrete water storage anomalies with a RMSE of 0.0016 km^3 (7.4% of variable capacity), and a median NSE of 0.94 (Figure 6). Our uncertainty decomposition reveals that WSA measurement errors contribute 32% of uncertainty while WSE errors contribute 68%. Critically, only 21% of uncertainty is attributed to the inherent WSE measurement noise (σ_{wse} = 10 cm), with the remaining WSE contributions coming from outliers that pass the functional filters. The idealized filter therefore provides a 38% reduction in RMSE over the functional results. Interpolating SWOT storage estimates to daily resolution increases the overall RMSE to 0.0020 km^3 (8% of variable capacity), with sampling gaps contributing 33% of uncertainty for estimating the water storage anomaly on any given day.

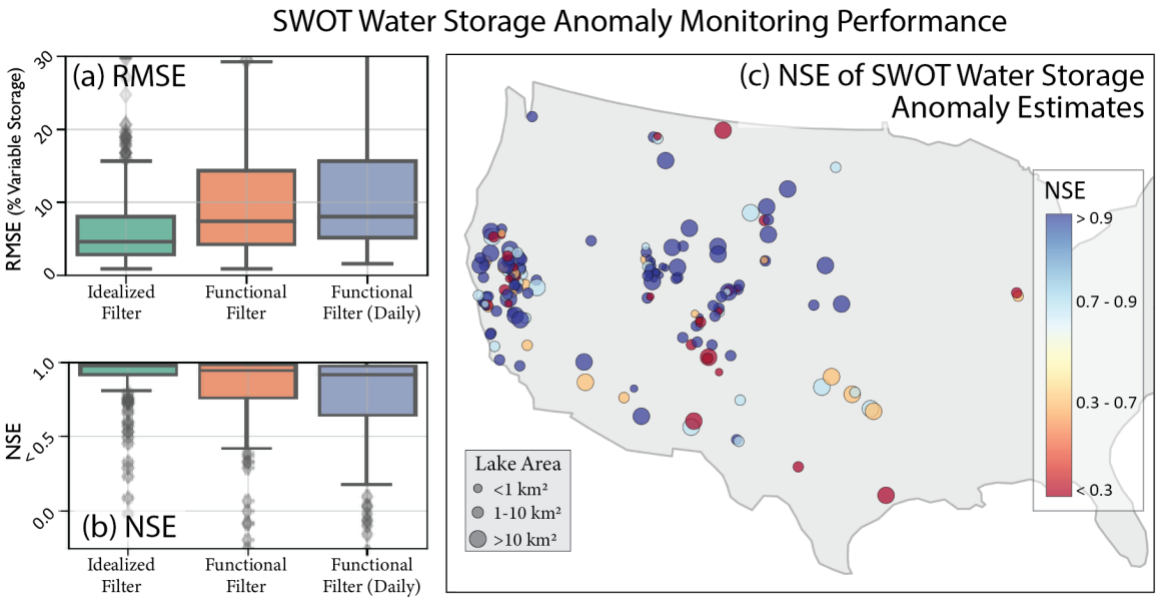

Figure 4.6: SWOT water storage anomaly estimations in 198 study lakes. (a) and (b) compare idealized and functional (adaptive) filters' RMSE and NSE for water storage anomaly estimates. The daily resolution (interpolated SWOT measurements) are also included. RMSE is expressed as a percentage of the variable water storage. (c) map of the NSE values in lakes and reservoirs using the functional filter and daily (gap-filled) estimates.

3.3 Water Storage Uncertainty Reduction

Integrating Sentinel-2 area observations improves SWOT water storage anomaly monitoring regardless of data filtering approach or temporal resolution, while the use of static areas significantly degrade performance (Figure 4.7, Table 4.3). The SWOT-S2 improvements to error metrics and NSE scores are particularly pronounced when using the idealized filter, as WSE outliers introduced through functional filtering and interpolation diminish the impact of enhanced WSA accuracy. The correlation coefficients between estimated and gauge-measured storage anomalies are nearly identical across the Static, SWOT, and SWOT-S2 models, as each approach uses common SWOT WSE time series to estimate storage. Differences among model performance are largely due to WSA bias, which has an outsized influence on storage estimates for large WSE anomalies leading to large errors near each lake's maximum and minimum water level. The S2 model's estimate errors are nearly an order of magnitude larger than the three models producing estimates for each SWOT WSE observation, but unlike the other models, its

performance is similar across discrete and daily temporal resolutions due to Sentinel-2's higher sampling rate.

Our uncertainty decomposition highlights the contrast between SWOT's idealized and functional performance, as filtering errors and sampling gaps contribute 40% to 64% of total uncertainty. As expected, the relative contribution of WSA measurement errors varies significantly according to the WSA data source. On average, our uncertainty attribution method predicts the observed RMSE within 10.9%, suggesting that the first-order analytical error propagation reasonably captures the relative importance of storage calculation inputs. The propagation method tends to overpredict the MAE by a factor of 1.2 to 1.8, suggesting that our constant uncertainty parameters capture the full distribution of errors including outlier predictions, while providing a conservative uncertainty estimate for most observations.

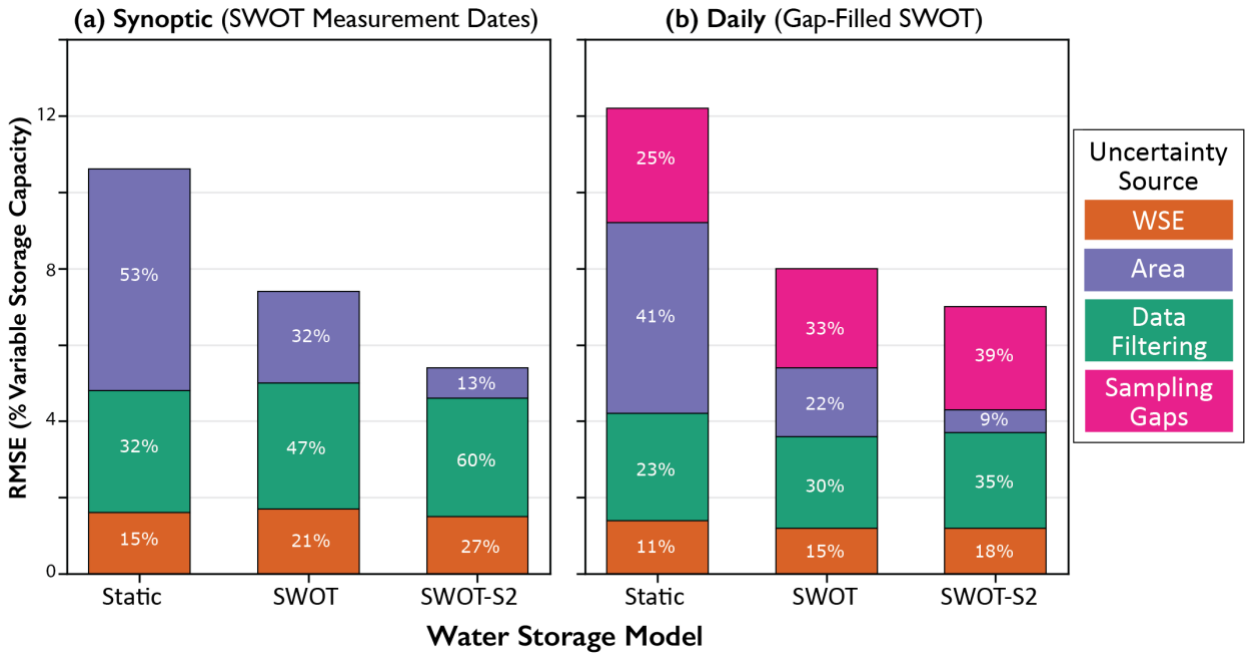

Figure 4.7: The total observed RMSE for each model's functional water storage estimates expressed as a percentage of variable water storage. The errors are decomposed into the relative uncertainty contributions from WSE and WSA measurement errors, data filtering errors, and sampling gaps based on our uncertainty propagation.

		Model	WSE σ (%)	Filtering σ (%)	Sampling σ (%)	WSA σ (%)	Propagated Uncertainty (% | km3)	Observed MAE (% | km^3)	Observed RMSE (% | km^3)	Median NSE
Idealized	Discrete	Static	21.5	0	0	78.5	8.4 | 0.0021	6.1 | 0.0013	7.9 | 0.0017	0.93
		SWOT	40.4	0	0	59.6	4.3 | 0.0011	3.6 | 0.0007	4.6 | 0.0010	0.97
		SWOT-S2	66.9	0	0	33.1	2.4 | 0.0007	2.0 | 0.0005	2.5 | 0.0007	0.99
		S2						16.2 | 0.0040	21.3 | 0.0056	0.37
Functional	Discrete	Static	14.6	32.1	0	53.2	11.5 | 0.0030	7.7 | 0.005	10.6 | 0.012	0.85
		SWOT	21.4	47.0	0	31.6	7.1 | 0.0020	5.0 | 0.0012	7.4 | 0.0016	0.94
		SWOT-S2	27.1	59.6	0	13.3	5.0 | 0.0016	3.3 | 0.0008	5.4 | 0.0013	0.97
		S2						17.3 | 0.0045	21.6 | 0.0060	0.32
	Daily	Static	11.3	22.6	24.8	41.2	14.6 | 0.0040	8.6 | 0.0016	12.2 | 0.0023	0.79
		SWOT	15.0	29.9	32.9	22.1	9.8 | 0.0031	5.5 | 0.0014	8.0 | 0.0020	0.92
		SWOT-S2	17.6	35.1	38.6	8.6	8.4 | 0.0028	4.5 | 0.0012	7.1 | 0.0056	0.94
		S2						17.1 | 0.0044	22.3 | 0.025	0.31

Table 4.3: Comparison of observed and predicted water storage anomaly errors across water storage model permutations.

4. Discussion

Our analysis of SWOT LakeSP's idealized and functional performance has significant implications for potential SWOT applications to water storage monitoring and historical water level reconstruction. By comparing a large sample of SWOT observations against in situ gauges, we verify that SWOT fulfills one of its core hydrology objectives to observe sub-monthly water storage anomalies in lakes, capturing seasonal to annual storage dynamics with a median NSE of 0.94 and RMSE of 7.4% of variable storage capacity. Here, we discuss how SWOT's functional 14-day temporal resolution and WSE measurement precision advances the practice of water storage remote sensing and illustrate its capabilities and caveats through example water storage time series. We also describe opportunities to enhance SWOT water storage monitoring performance through improved observation filtering and water surface area mapping.

4.1. Contextualizing SWOT Water Storage Monitoring Performance

In the context of water storage remote sensing, SWOT's most significant contribution is the new ability to estimate water storage volume directly from water level time series at temporal and spatial resolutions comparable to optical satellites like Landsat. Existing profiling satellite altimeters such as ICESat-2 have similar WSE accuracy to SWOT (Bazzi et al., 2025; Birkett et al., 2018; Cooley et al., 2021; Ryan et al., 2020; Yuan et al., 2020), but very few examples directly estimate water storage from pre-SWOT altimetry due to their long revisit period and poor spatial coverage (Bonnema et al., 2016). Therefore, most existing water storage remote sensing approaches use surface area time series as a proxy for water levels (Hou et al., 2024; Li et al., 2023; Schwatke et al., 2020; Yao et al., 2023). We tested an analogous area-based approach using Sentinel-2 WSA time series and our SWOT – S2 AE curves (S2 model, Table 4.1). In lakes with gradual bathymetry where area is highly variable, the S2 model successfully tracks relative water storage variability (e.g., Figure 8a, 8c, and 8e). In cloud-free conditions, Sentinel-2 provides more frequent observations and a longer historical record, and can therefore support attempts to reduce latency, increase observation density, and reconstruct historical fluctuations.

However, the S2 model exhibits an overall 716% increase in median RMSE for water storage estimates compared to the SWOT-S2 model, despite utilizing the same underlying AE relationships (Table 4.3). This finding reflects the fundamental limitation of area-based storage estimation in lakes with stable areas, such as Figure 8b. In lakes with steep bathymetry or overhanging vegetation, volumetric fluctuations do not produce measurable surface area changes from satellite imagery. Our S2 model completely failed (NSE < 0) in 32.5% of lakes, partially due to 21% of lakes having insignificant AE relationships. This physical constraint has biased our pre-SWOT observations towards specific environments and helps explain why existing global water storage datasets include < 1% of the lakes observed by SWOT (Hou et al., 2024; Li et al., 2023; Schwatke et al., 2020; Wang et al., 2025; Yao et al., 2023).

Given SWOT's recent launch, future work will likely integrate SWOT with Landsat and MODIS to take advantage of their longer historical record. These sensors introduce additional concerns over Sentinel-2. First, multi-decadal Landsat lake area trends have been shown to introduce a bias towards increasing water area associated with increasing observation frequency

(Webb et al., in review). Second, Landsat and MODIS' coarser spatiotemporal resolution decreases sensitivity to water surface area changes and reduces the number of paired observations with SWOT for building AE curves. Visual inspection of the AE curves in Figure 4.8 suggests that inverting these relationships to evaluate WSE as a function of WSA generally increases the slope such that small area measurement errors produce large errors in WSE estimates. As a result, our area-based estimates were notably noisier compared to WSE-based estimates even in lakes with significant AE relationships. State-of-the-art Landsat-based methods for estimating water aim for sub-meter water level accuracy (Tortini et al., 2020; Yao et al., 2024), which is significantly higher than SWOT'S 10 cm measurement precision (Table 4.2). Compared to these methods, SWOT provides an order of magnitude improvement to WSE and relative water storage accuracy.

Direct estimation of storage from WSE time series rather than WSA is now possible using SWOT's frequent, spatially distributed altimetry information. Our SWOT water storage anomaly estimates are accurate within 7.4% of variable capacity, or 0.0016 km^3. This degree of accuracy represents a significant improvement over previous relative storage datasets with errors equivalent to 10.8% to 15.6% of *total* reservoir capacity (Cooley et al., 2025), or 0.87 km^3 (Tortini et al., 2020). As expected, our relative storage estimates are also more accurate than SWOT-based estimates of total storage due to added uncertainty for estimating bathymetry below the minimum SWOT observation (Das & Hossain, 2025). As WSE is much more sensitive to storage changes in many lakes, SWOT will likely redefine the meaning of 'global' water storage monitoring from sampling hundreds to thousands of carefully selected lakes stratified by continent (Cooley et al., 2025), to full spatiotemporal dynamics. The impacts for local scale studies may be even more substantial, as SWOT will provide the first source of storage time series for most lakes.

4.2. SWOT's Temporal Sampling

Our analysis reveals that sampling gaps caused by SWOT's orbit represent a substantial source of uncertainty for applications demanding continuous data such as operational monitoring or event-scale investigations (e.g., flood mapping). Multiple distinct storage signals can produce identical sequences of SWOT observations. Therefore, we must be careful when assuming a

trend of storage change between discrete observations, as we cannot distinguish true hydrologic behavior from sampling artifacts below certain time scales (Figure 4.5). To borrow from the field of signal processing, sampling rates impose a fundamental limit on the temporal resolution of water storage variability that can be reliably detected. The Nyquist-Shannon sampling theorem states that a signal must be sampled at least twice per cycle to be accurately reconstructed or else high-frequency variations are aliased into lower frequencies or lost entirely (Shannon, 1948). For example, Figure 4.8f demonstrates the concept of aliasing, where sparse sampling of high-frequency fluctuations produces a false seasonal-scale trend.

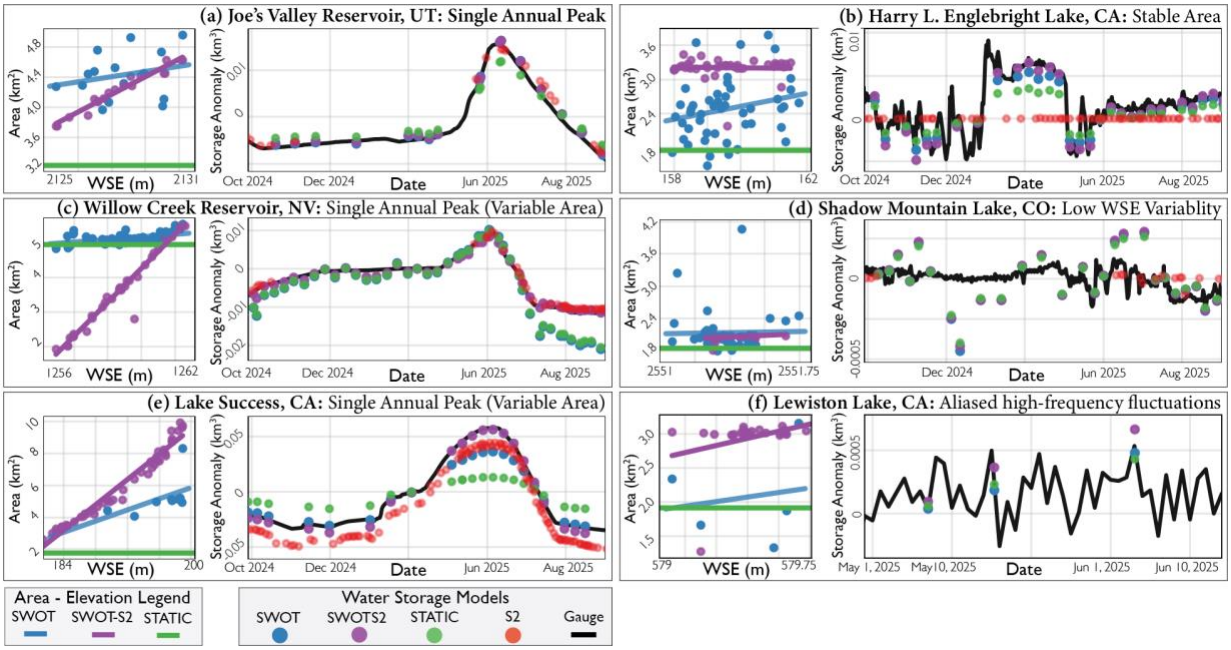

Figure 4.8: Example AE relationships and water storage time series for six lakes and reservoirs in our benchmark dataset. (a-e) show time series for water year 2025 and (f) highlights a six-week period in spring 2025. Each of the four storage models are presented in comparison to gauge water storage anomalies. Both the SWOTS2 and S2 models are based on the SWOT-S2 (purple) AE curves.

With a functional temporal resolution of approximately 14 days, SWOT can theoretically resolve storage fluctuations with periods longer than 28 days, but sub-monthly dynamics including flood pulses, rapid drawdowns, and event-scale responses to precipitation, may be

aliased or entirely undetected. Our empirical findings support these theoretical constraints as SWOT only detects 35% of storage variability over 30-day time windows. SWOT cannot reliably capture a lake's sub-seasonal dynamics, but detection is possible when overpasses and hydrologic events align. Therefore, SWOT performs best in lakes with longer duration fluctuations, such as the snowmelt and water supply regimes shown in Figure 8a, 8c, and 8e. SWOT performance also depends on the magnitude of WSE variability. In lakes where WSE variations are below SWOT's measurement precision (e.g., Figure 8d), SWOT is likely to overestimate storage variability.

Despite limitations for event-scale hydrology, SWOT's bi-weekly observations will significantly improve our characterization of seasonal patterns, annual storage exceedance probabilities, and interannual trends moving forward, particularly in lakes with WSE variability larger than 20 cm. Sparser time series, such as ICESat-2 or cloud-affected monthly Landsat observations, are vulnerable to aliasing over longer time scales. Interannual trends derived from a handful of observations per year are highly sensitive to the timing of observations relative to seasonal fluctuations, potentially confounding interannual signals with sampling artifacts. As SWOT's revisit time, even after filtering, leads to it capturing an average of 84% of annual storage capacity variability, SWOT should enable reliable decomposition of intra-annual variability and interannual trends.

4.3. Future Enhancements

Our results suggest that advances in data filtering and water surface area mapping can yield substantial progress towards optimizing SWOT's accuracy and impact for water storage applications. Current observation filtering best practices still struggle with outlier removal, increasing relative storage RMSE by 61% relative to idealized performance. At this stage, WSE performance improvements are possible at two levels: pixel masking and aggregations that would be incorporated in science data algorithms, and LakeSP post-processing to filter and smooth time series. Outlier retention also produces a discrepancy in SWOT performance as reported by outlier-sensitive error metrics (e.g., RMSE and 1$\boldsymbol{\sigma}$) versus outlier resistant metrics such as MAE or the 68th percentile of absolute errors (Table 4.2). Therefore, we highly recommend that future SWOT assessments report multiple error metrics rather than assume that

errors are normally distributed. This will be particularly important for applications requiring datum-referenced elevations, such as flood mapping or explicitly linking lakes to river networks.

Water surface area measurements remain a significant source of uncertainty for water storage monitoring with SWOT, which is optimized for altimetry purposes. The high uncertainty attributions to SWOT WSA measurements (Figure 4.7) likely result from water storage calculations sensitivity to both bias and random WSA errors, whereas WSE bias does not influence relative storage errors. We identify a solution that significantly reduces storage uncertainty, which is to produce hypsometric curves using paired SWOT WSE and Sentinel-2 WSA observations. The improved slope of the SWOT-S2 AE relationships generates more accurate estimates of the maximum and minimum storage anomalies in the time series, as shown in Figures 4.8c and 4.9e. In cases where SWOT does not capture area variability, such as Figure 4.8c, the lake bathymetry is essentially treated as a cylinder, causing exaggerated negative water storage anomalies. By measuring the reduced WSA at lower water levels, Sentinel-2 more accurately represents the lake bathymetry as a truncated cone, thus improving water storage estimates. In Figure 4.8f, in particular, bias in SWOT WSA in storage calculations produces underestimated water storage variability. Overall, the use of SWOT WSA represents a significant improvement over static area models, and Sentinel-2 areas represent a significant improvement over SWOT areas.

A critical future direction will be integrating SWOT with ancillary in situ and satellite observations, weather data, and hydrologic models to fill sampling gaps. The RMSE of daily estimates was 44% higher than discrete SWOT measurements alone, indicating that SWOT's revisit frequency is the primary limiting factor for continuous monitoring over its measurement precision. Interpolating SWOT measurements to daily resolution is an admittedly naïve approach to estimating storage conditions at any given timestep, but its purpose here is to quantify the information lost by SWOT's sampling gaps and more directly compare to daily estimations produced by hydrologic models. Understanding the uncertainty caused by sampling gaps also supports future wide-swath altimetry missions, such as Sentinel Next Generation Topography Mission, which plans to reduce the revisit period and continue the record of surface water topography data globally (Egido, 2023).

5. Conclusion

Our benchmarking analysis of SWOT water storage performance in 411 lakes confirms its role as a breakthrough technology for measuring surface water from space. SWOT was designed to overcome the fundamental tradeoff between accuracy, temporal resolution, and spatial coverage of existing sensors, but until now incomplete characterization of its capabilities and limitations has limited adoption. We urge careful consideration of SWOT's fundamental constraints when interpreting storage time series, namely the revisit frequency and WSE measurement precision. Using a simple filtering scheme, we identified a functional average temporal resolution of 14 days and WSE precision of 18 cm. Short-term dynamics such as precipitation responses, hydropower releases, or tidal patterns are thus only observed when the timing coincides with SWOT overpasses. When water level variability is below 20 cm, meaningful hydrologic behavior cannot be distinguished from SWOT measurement noise. These constraints nonetheless represent a substantial improvement over previous approaches, enabling reliable reconstruction of seasonal to interannual water storage dynamics in lakes globally. To improve accuracy, we recommend prioritizing enhancements to observation filtering and water surface area mapping. Filtering progress will most likely occur through updates to science data algorithms and continued LakeSP post-processing development and testing. Water classification and area measurements remain a challenge given inherent sensor characteristics, but we show that building hypsometric curves by pairing SWOT WSE with high-resolution Sentinel-2 measurements can significantly reduce storage uncertainty.

References

Alsdorf, D. E., Rodríguez, E., & Lettenmaier, D. P. (2007). Measuring surface water from space. *Reviews of Geophysics*, *45*(2), 2006RG000197. https://doi.org/10.1029/2006RG000197

Bazzi, H., Baghdadi, N., Ngo, Y.-N., Normandin, C., Frappart, F., & Cazals, C. (2025). Assessing SWOT interferometric SAR altimetry for inland water monitoring: Insights from Lake Léman. *Frontiers in Remote Sensing*, *6*, 1572114. https://doi.org/10.3389/frsen.2025.1572114

Biancamaria, S., Lettenmaier, D. P., & Pavelsky, T. M. (2016). The SWOT Mission and Its Capabilities for Land Hydrology. In A. Cazenave, N. Champollion, J. Benveniste, & J. Chen (Eds.), *Remote Sensing and Water Resources* (pp. 117–147). Springer International Publishing. https://doi.org/10.1007/978-3-319-32449-4_6

Birkett, C. M., Reynolds, C. A., Deeb, E. J., Ricko, M., Beckley, B. D., & Yang, X. (2018). *G-REALM: A Lake/Reservoir Monitoring tool for Water Resources and Regional Security assessment*. *2018*, H51S-1570. https://ui.adsabs.harvard.edu/abs/2018AGUFM.H51S1570B

Bonnema, M., Sikder, S., Miao, Y., Chen, X., Hossain, F., Ara Pervin, I., Mahbubur Rahman, S. M., & Lee, H. (2016). Understanding satellite-based monthly-to-seasonal reservoir outflow estimation as a function of hydrologic controls. *Water Resources Research*, *52*(5), 4095–4115. https://doi.org/10.1002/2015WR017830

Cooley, S. W., Ryan, J. C., & Smith, L. C. (2021). Human alteration of global surface water storage variability. *Nature*, *591*(7848), 78–81. https://doi.org/10.1038/s41586-021-03262-3

Cooley, S. W., Smith, L. C., Stepan, L., & Mascaro, J. (2017). Tracking Dynamic Northern Surface Water Changes with High-Frequency Planet CubeSat Imagery. *Remote Sensing*, *9*(12), Article 12. https://doi.org/10.3390/rs9121306

Cooley, S. W., Wang, J., Gao, H., Yao, F., Livneh, B., Li, Y., Hou, J., Hao, Z., Cai, X., & Ling, F. (2025). Global intercomparison of satellite-derived variability in reservoir storage. *Environmental Research Letters*, *20*(8), 084035. https://doi.org/10.1088/1748-9326/ade903

Das, P., & Hossain, F. (2025). Multi-Satellite Tracking of Surface Water Storage Change in the Era of Surface Water and Ocean Topography (SWOT) Satellite Mission. *Earth and Space Science*, *12*(6), e2024EA004178. https://doi.org/10.1029/2024EA004178

Dhote, P. R., Agarwal, A., Paris, A., Singhal, G., Thakur, P. K., Oubanas, H., Moreira, D. M., Gal, L., Garg, V., Kumar, P., Singh, R. P., & Calmant, S. (2025). Unveiling the First Impressions of the Wide-Swath Altimetry SWOT Mission Over the Ganga River, India. *Geophysical Research Letters*, *52*(19), e2025GL115402. https://doi.org/10.1029/2025GL115402

Egido, A. (2023). *The Sentinel-3 Next Generation Topography (S3NG-TOPO) Mission; Enhancing Continuity, Performance and Hydrology Capabilities*. https://doi.org/10.24400/527896/A03-2023.3823

Fergus, C. E., Brooks, J. R., Kaufmann, P. R., Pollard, A. I., Mitchell, R., Geldhof, G. J., Hill, R. A., Paulsen, S. G., Ringold, P., & Weber, M. (2022). Natural and anthropogenic controls on lake water-level decline and evaporation-to-inflow ratio in the conterminous United States. *Limnology and Oceanography*, *67*(7), 1484–1501. https://doi.org/10.1002/lno.12097

Frank Greguska, Nikki Tebaldi, Victoria McDonald, Vanesa, Cassie Nickles, & James Wood. (2025). *podaac/hydrocron: 1.6.5* (Version 1.6.5) [Computer software]. Zenodo. https://doi.org/10.5281/ZENODO.11176233

Fu, L., Pavelsky, T., Cretaux, J., Morrow, R., Farrar, J. T., Vaze, P., Sengenes, P., Vinogradova-Shiffer, N., Sylvestre-Baron, A., Picot, N., & Dibarboure, G. (2024). The Surface Water and Ocean Topography Mission: A Breakthrough in Radar Remote Sensing of the Ocean and Land

Surface Water. *Geophysical Research Letters*, *51*(4), e2023GL107652. https://doi.org/10.1029/2023GL107652

Gao, H., Birkett, C., & Lettenmaier, D. P. (2012). Global monitoring of large reservoir storage from satellite remote sensing. *Water Resources Research*, *48*(9), 2012WR012063. https://doi.org/10.1029/2012WR012063

Girard, F., Kergoat, L., Mainassara, I., Wubda, M., Nikièma, E. D., Touré, A. A., Renou, J., Vayre, M., Taburet, N., Picot, N., & Grippa, M. (2025). Performance of the Surface Water and Ocean Topography (SWOT) Mission for Monitoring Small Lakes in West Africa. *IEEE Journal of Selected Topics in Applied Earth Observations and Remote Sensing*, *18*, 14855–14869. https://doi.org/10.1109/JSTARS.2025.3570859

Hamoudzadeh, A., Ravanelli, R., & Crespi, M. (2024). SWOT Level 2 Lake Single-Pass Product: The L2_HR_LakeSP Data Preliminary Analysis for Water Level Monitoring. *Remote Sensing*, *16*(7), 1244. https://doi.org/10.3390/rs16071244

Hou, J., Van Dijk, A. I. J. M., Renzullo, L. J., & Larraondo, P. R. (2024). GloLakes: Water storage dynamics for 27 000 lakes globally from 1984 to present derived from satellite altimetry and optical imaging. *Earth System Science Data*, *16*(1), 201–218. https://doi.org/10.5194/essd-16-201-2024

Levenson, E. S., Cooley, S., Mullen, A., Webb, E. E., & Watts, J. (2025). Glacial History Modifies Permafrost Controls on the Distribution of Lakes and Ponds. *Geophysical Research Letters*, *52*(4), e2024GL112771. https://doi.org/10.1029/2024GL112771

Levenson, E. S., Cooley, S. W., & Mullen, A. (2025). *Arctic-Boreal Vulnerability Experiment (ABoVE)ABoVE: Alaska Lake and Pond Occurrence* (Version 1, p. 0 MB) [COG, ESRI Shapefile]. ORNL Distributed Active Archive Center. https://doi.org/10.3334/ORNLDAAC/2399

Li, Y., Zhao, G., Allen, G. H., & Gao, H. (2023). Diminishing storage returns of reservoir construction. *Nature Communications*, *14*(1), 3203. https://doi.org/10.1038/s41467-023-38843-5

Maubant, L., Dodd, L., & Tregoning, P. (2025). Assessing the Accuracy of SWOT Measurements of Water Bodies in Australia. *Geophysical Research Letters*, *52*(6), e2024GL114084. https://doi.org/10.1029/2024GL114084

Ming, J., Jiang, L., Ma, D., & Liu, J. (2025). SWOT Unveils the Hidden Hydrodynamics of the Three Gorges Reservoir. *Geophysical Research Letters*, *52*(22), e2025GL118488. https://doi.org/10.1029/2025GL118488

Peral, E., & Esteban-Fernandez, D. (2018). Swot Mission Performance and Error Budget. *IGARSS 2018 - 2018 IEEE International Geoscience and Remote Sensing Symposium*, 8625–8628. https://doi.org/10.1109/IGARSS.2018.8517385

Ryan, J. C., Smith, L. C., Cooley, S. W., Pitcher, L. H., & Pavelsky, T. M. (2020). Global Characterization of Inland Water Reservoirs Using ICESat-2 Altimetry and Climate Reanalysis. *Geophysical Research Letters*, *47*(17), e2020GL088543. https://doi.org/10.1029/2020GL088543

Schwatke, C., Dettmering, D., & Seitz, F. (2020). Volume Variations of Small Inland Water Bodies from a Combination of Satellite Altimetry and Optical Imagery. *Remote Sensing*, *12*(10), 1606. https://doi.org/10.3390/rs12101606

Shannon, C. E. (1948). A mathematical theory of communication. *The Bell System Technical Journal*, *27*(3), 379–423.

Thurman, H. R., Allen, G. H., Williams, B. A., Cerbelaud, A., & David, C. H. (2025). SWOT Captures Hydrologic Waves Traveling Down Rivers. *Geophysical Research Letters*, *52*(10), e2024GL113875. https://doi.org/10.1029/2024GL113875

Tortini, R., Noujdina, N., Yeo, S., Ricko, M., Birkett, C. M., Khandelwal, A., Kumar, V., Marlier, M. E., & Lettenmaier, D. P. (2020). Satellite-based remote sensing data set of global surface water storage change from 1992 to 2018. *Earth System Science Data*, *12*(2), 1141–1151. https://doi.org/10.5194/essd-12-1141-2020

Tranvik, L. J., Downing, J. A., Cotner, J. B., Loiselle, S. A., Striegl, R. G., Ballatore, T. J., Dillon, P., Finlay, K., Fortino, K., Knoll, L. B., Kortelainen, P. L., Kutser, T., Larsen, Soren., Laurion, I., Leech, D. M., McCallister, S. L., McKnight, D. M., Melack, J. M., Overholt, E., … Weyhenmeyer, G. A. (2009). Lakes and reservoirs as regulators of carbon cycling and climate. *Limnology and Oceanography*, *54*(6part2), 2298–2314. https://doi.org/10.4319/lo.2009.54.6_part_2.2298

Vinogradova, N. T., Pavelsky, T. M., Farrar, J. T., Hossain, F., & Fu, L.-L. (2025). A new look at Earth's water and energy with SWOT. *Nature Water*, *3*(1), 27–37. https://doi.org/10.1038/s44221-024-00372-w

Wang, J., Pottier, C., Cazals, C., Battude, M., Sheng, Y., Song, C., Sikder, M. S., Yang, X., Ke, L., Delhoume, M., Gosset, M., Oliveira, R. R. A., Grippa, M., Girard, F., Allen, G. H., Xu, X., Zhu, X., Biancamaria, S., Smith, L. C., … Pavelsky, T. M. (2025). The Surface Water and Ocean Topography Mission (SWOT) Prior Lake Database (PLD): Lake Mask and Operational Auxiliaries. *Water Resources Research*, *61*(3), e2023WR036896. https://doi.org/10.1029/2023WR036896

Yao, F., Livneh, B., Rajagopalan, B., Cretaux, J., Wada, Y., & Berge-Nguyen, M. (2023). Satellites reveal widespread decline in global lake water storage. *Science*, *380*, 743–749.

Yao, F., Livneh, B., Rajagopalan, B., Wang, J., Yang, K., Crétaux, J., Wang, C., & Minear, J. T. (2024). Leveraging ICESat, ICESat-2, and Landsat for Global-Scale, Multi-Decadal Reconstruction of Lake Water Levels. *Water Resources Research*, *60*(2), e2023WR035721. https://doi.org/10.1029/2023WR035721

Yuan, C., Gong, P., & Bai, Y. (2020). Performance Assessment of ICESat-2 Laser Altimeter Data for Water-Level Measurement over Lakes and Reservoirs in China. *Remote Sensing*, *12*(5), 770. https://doi.org/10.3390/rs12050770

Zhong, R., Zhao, T., & Chen, X. (2020). Hydrological Model Calibration for Dammed Basins Using Satellite Altimetry Information. *Water Resources Research*, *56*(8), e2020WR027442. https://doi.org/10.1029/2020WR027442

APPENDIX

APPENDIX A – CHAPTER II SUPPORTING INFORMATION

Text A1. ALPOD Dataset Construction

1.1 Motivation and Characteristics of ALPOD

Improvements to the spatiotemporal resolution of satellite imagery in recent years have enabled researchers to document seasonal fluctuations in Arctic-Boreal waterbody extent (Cooley et al., 2017; 2019; Mullen et al., 2023). Their results demonstrate that the size, number, and total area of lakes and ponds can vary significantly over daily timescales, which limits the utility of static or snapshot-based surface water datasets for accurately characterizing the surface water distribution in high-northern latitudes. To overcome this limitation, we produced a lake and pond open-water occurrence map using every available image during the ice-free months of 2016-2021. This lake and pond occurrence raster is a singleband, 10 m resolution GeoTIFF covering all of Alaska with pixel values recording the percentage of observations in which that location was identified as open water belonging to a lake or pond. We also produced vector-based lake products derived from the occurrence map at multiple occurrence thresholds. This lake dataset accounts for six years of dynamic seasonality and is thus more robust against the effects of degraded individual image quality due to clouds, cloud shadows, or haze. Our aim was to produce a dataset that has utility for understanding lake and pond dynamics at scales ranging from single water bodies to the entire state of Alaska.

1.2 Overarching ALPOD Dataset Engineering Approach

Our dataset construction methodology combines object and pixel-based water classification methods. Deep-learning semantic segmentation models such as U-Nets are useful for mapping lakes and ponds because they can separate these water bodies from features of the landscape – such as rivers, cloud shadows, hillshades, and burn scars – that have similar reflectance properties as lakes (see section 1.4). However, these models are computationally expensive and are not currently compatible with Google Earth Engine (GEE), thus limiting their applicability for occurrence mapping over a large study area. Normalized Difference Water Index (NDWI) (McFeeters, 1996) histogram thresholding is a pixel-based method for mapping open water, and

its computational efficiency promotes the utility of NDWI thresholding algorithms for mapping surface water over large extents and at high frequencies. Our approach (Figure A1) overcomes the relative disadvantages of both the object and pixel-based classification methods by first using a U-Net lake identification model to produce a maximum possible lake extent mask across our study site. This mask filters out the extraneous features of the landscape listed above (e.g., rivers) and serves as the 'region of interest' for an adaptive NDWI thresholding algorithm, which is a binary water classifier applied to every available Sentinel-2 image in Google Earth Engine. The ALPOD lake occurrence raster is a singleband composite built from each of these open-water classifications.

1.3 Sentinel-2 Imagery

Our choice of source imagery is based on tradeoffs between spatial resolution, temporal resolution, data volume, and accessibility. The scope of our study through space and time precludes the use of commercial high-resolution data such as Planet, as the data volumes and accessibility would make the study unfeasible. Part of our motivation for this study was to improve on Landsat-based surface water products by utilizing finer spatiotemporal resolution data that can better capture the open water occurrence dynamics in individual lakes and ponds. Sentinel-2 imagery's 10-m pixels balance our needs for high spatial resolution data that is usable over a large study extent. Additionally, Sentinel-2 provides near-daily temporal resolution across most of our study area due to the polar orbits of the two satellite platforms.

1.4 Maximum Lake Extent Mask Production

To produce a mask of the maximum possible lake extent across Alaska, we first downloaded 1-2 Sentinel-2 images across the study area. The images were selected to capture the maximum surface water extent within a cloud, ice, and haze-free image during 2016-2021. The choice was made based on visual inspection before download, and the dates of each image are recorded in *Sentinel-2_dates.xlxs*. Next, we used a U-Net model to predict the lake extent in each image. U-Nets are a subset of convolutional neural networks, and they are designed to extract target object features from images. A trained U-Net model references representations of features such as edges and frequencies at a range of scales to map the probability that each pixel belongs to the target

class. We used a lake identification U-Net model (Mullen et al., 2023) that was trained on Planet imagery to predict lake extents on the Sentinel-2 images. We merged and vectorized the outputs of the U-Net predictions before buffering by 60 m. The buffer serves two purposes: (1) ensuring that the maximum water extent is included in the mask, and (2) including land pixels thus ensuring that the NDWI histogram will be bimodal (see section 1.5). At this stage, we also merged the U-Net results with the Prior Lake Database (Wang et al., 2024) to ensure that the largest lakes are included in the mask. We manually inspected and edited the U-Net predictions in QGIS by visualizing the shapefile over the previously downloaded Sentinel-2 imagery. At this stage, we fixed both errors of omission and commission by deleting misclassified water bodies and producing polygons to include missed lakes. We conducted this manual edit at a consistent scale of 1:50,000 to finalize the maximum possible lake extent mask before uploading it as an asset to GEE.

1.5 Water Classification in Google Earth Engine

Our lake occurrence dataset is produced using a water classification algorithm based on adaptive NDWI thresholding (Cooley et al., 2017; 2019). We first split our study site into 160 km^2 tiles to run our water classification script. For a given tile, we produced a collection of cloud-masked Sentinel-2 mosaics for every available date during the ice-free months of 2016-2021. We clipped the mosaic to the maximum possible lake extent mask produced in section 1.3 and filtered out mosaics covering less than 70% of the ROI.

Our water classification method is covered in detail in Cooley et al. (2017), but a brief description is provided here. First, we produce an NDWI image by calculating the difference between the green and near-infrared bands divided by the sum of the green and near-infrared bands. Since our maximum lake extent mask is buffered and therefore includes both water and land pixels, the histogram of the NDWI is bimodal with peaks corresponding to land and water. Our algorithm calculates the land and water NDWI thresholds based on these peaks, and the percent of each mixed pixel that is covered by water (water fraction). Here, we defined open water as any pixel that is at least 75% water. We mapped the binary water classification to each pixel using this adaptively calculated NDWI threshold. To determine the day of year (DOY) range for each tile, we manually examined Sentinel-2 images for lake ice and chose a start date following ice-out. We

applied the binary water classification to every Sentinel-2 mosaic within this DOY range across 2016-2021 and recorded the average open water classification value for each pixel. This average represents the percentage of observations that each pixel was identified as open water.

1.5 Postprocessing and Vectorization

After exporting from GEE, we post-processed our lake occurrence image to remove extraneous pixels from the buffered maximum possibility lake occurrence mask. A hard occurrence threshold leaves isolated pixels that should be associated with nearby lakes. To overcome this challenge, we used a watershed segmentation algorithm, which is a region-based technique to separate foreground objects from the background. Using this technique, we produced a binary lake mask to remove background pixels from the lake occurrence mask. Lastly, we vectorized the lake mask at 25%, 50%, and 75% open-water occurrence threshold and exported to shapefiles.

1.6 Uncertainty Assessment

In order to assess the accuracy and precision of ALPOD, we split the study area into 25 km^2 tiles. We randomly sampled 100 tiles and compared our lake dataset to the ESRI base map imagery, which is primarily constructed from very high-resolution aerial and satellite imagery. During this process, we found that while ALPOD was able to capture ponds as small as 0.0001 km^2, water bodies less than 0.001 km^2 were frequently omitted. Therefore, we truncated the dataset at 0.001 km^2 for our uncertainty assessment and the analysis in this paper. After the low-end truncation, we manually measured and recorded the surface area of errors of omission and commission.

Using these results, we calculated the F1 score using the following formula:

$$Precision = \frac{True\ Positive}{True\ Positive + False\ Positive}$$

$$Recall = \frac{True\ Positive}{True\ Positive + False\ Negative}$$

$$F1 = 2 * \frac{(Precision * Recall)}{(Precision + Recall)}$$

Following these equations, ALPOD'S F1 score on the 2500 km^2 quality assessment area was 0.999, which suggests that ALPOD reliably maps lake extents. We also calculated the error metrics listed in Table A1 using the methods included in the supplementary file *uncertaintyAssessment.py*.

Text A2. Spatial analysis

Our spatial analysis utilizes the ancillary datasets in Table A2 to differentiate lakes by permafrost extent, topography, glacial history, geologic substrate, and watershed. First, we sampled each ancillary dataset at the centroid of each lake to assign physiographic characteristics to individual water bodies. We also intersected the datasets to calculate the total land area for each unique combination of glacial history, substrate texture, and permafrost extent. We produced Table A3 using these lake attributes and terrain classifications.

Using Cuzick's test for trend, we test the null hypothesis that there is no trend in lake fraction (percent of area covered by lakes) across the permafrost classes ordered by increasing permafrost extent. Cuzick's test is a non-parametric test to assess the presence of a trend in ordered data. Here, we use it to test for a monotonic trend across permafrost groups, ordered from least permafrost to most. To carry out this statistical analysis, we aggregated the lake dataset into NHD watersheds and calculated lake fraction, density, and mean surface area. We log-transformed these lake statistics to approximate a normal distribution and also classified each watershed by permafrost extent, glacial history, and geologic substrate texture by intersecting with the ancillary datasets above. Any watershed with multiple classes (glaciated and unglaciated) is assigned the class with the largest area. We calculated the mean permafrost probability within each watershed and classified them using the same scheme as Obu et al. (2018).

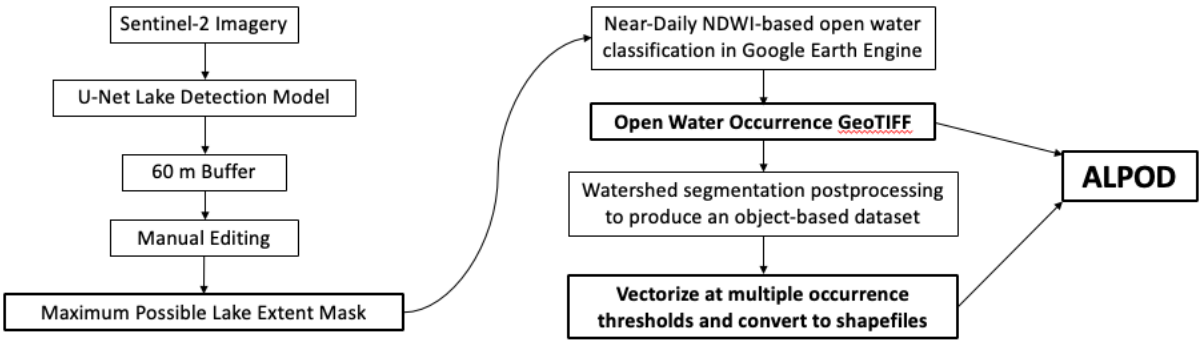

Figure A1: Methodological approach to constructing the ALPOD dataset.

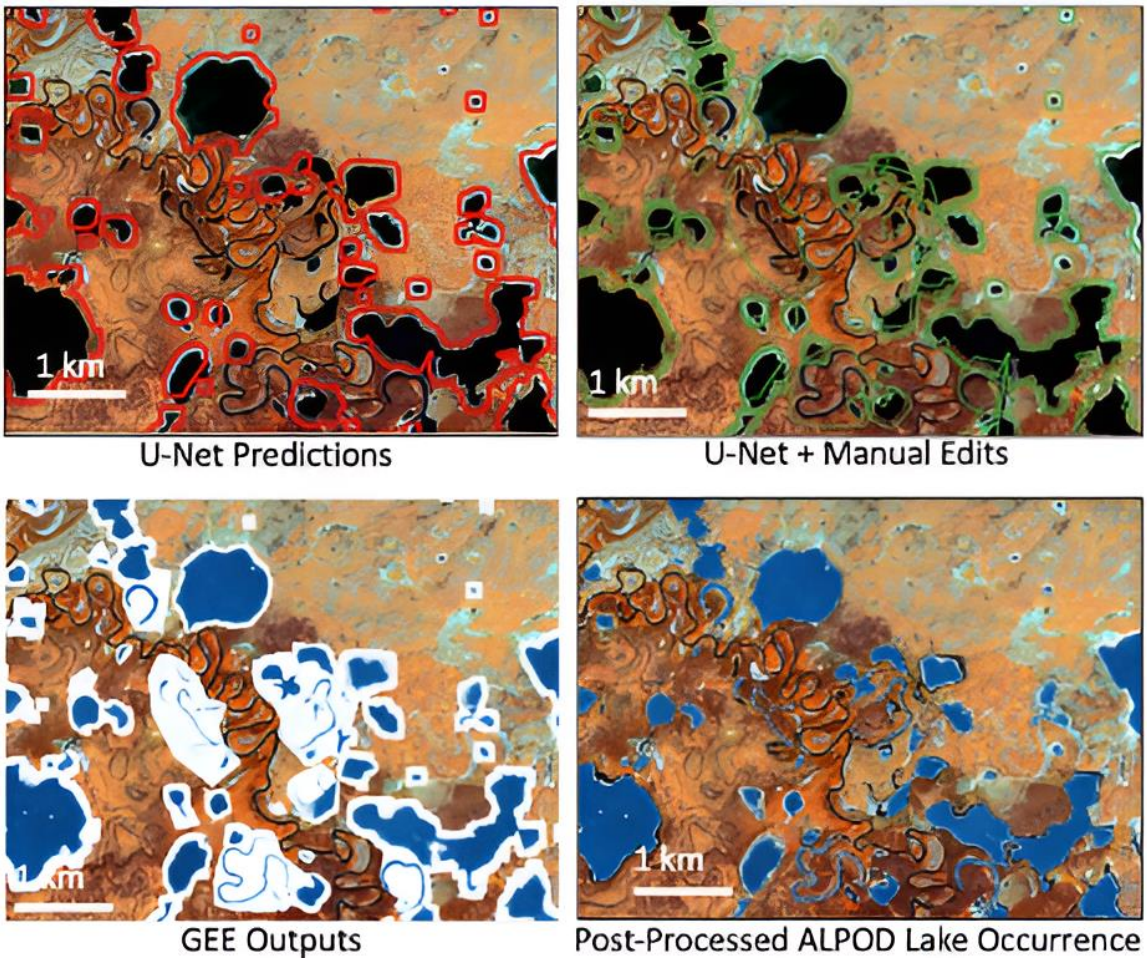

Figure A2: Dataset construction progression starting with the U-Net predictions. Manual edits to the U-Net outputs produce the maximum possible lake extent mask (upper right). The lower left panel shows the output of the GEE processing that classifies open water in every available image within the maximum lake mask. Lastly, the final lake occurrence image is produced by applying a watershed segmentation algorithm to the GEE outputs. Note the areas within the maximum

possible lake extent mask (green) that are excluded from the final lake occurrence dataset. These areas had low open-water occurrence values and were filtered by the watershed segmentation post-processing algorithm.

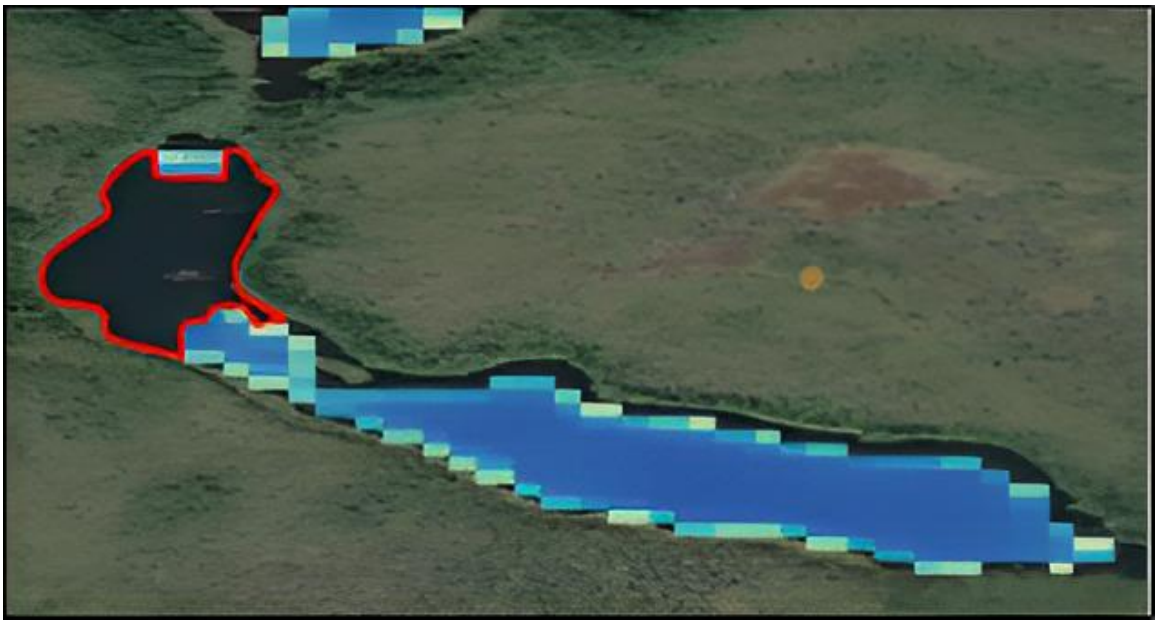

Figure A3: Example of the area measured to calculate errors of omission.

Error Metric	**Score**
F1	0.999
Mean Absolute Error	0.054
Mean Square Error	0.072
Root Mean Square Error	0.269
R^2	0.99

Table A1: ALPOD uncertainty assessment results

Variable	Citation	Access
Permafrost Extent	Obu et al., 2019	https://doi.pangaea.de/10.1594/PANGAEA.888600
Hydrography	National Hydrography Dataset	http://datainventory.doi.gov/id/dataset/1bc18823c4f541231fea4cbeffabb547"
Glacial History	Batchelor et al., 2019	https://doi.10.17605/OSF.IO/7JEN3
Geologic Substrate	Jorgenson et al., 2008	https://catalog.northslopescience.org/dataset/1725

Table A2: Ancillary datasets

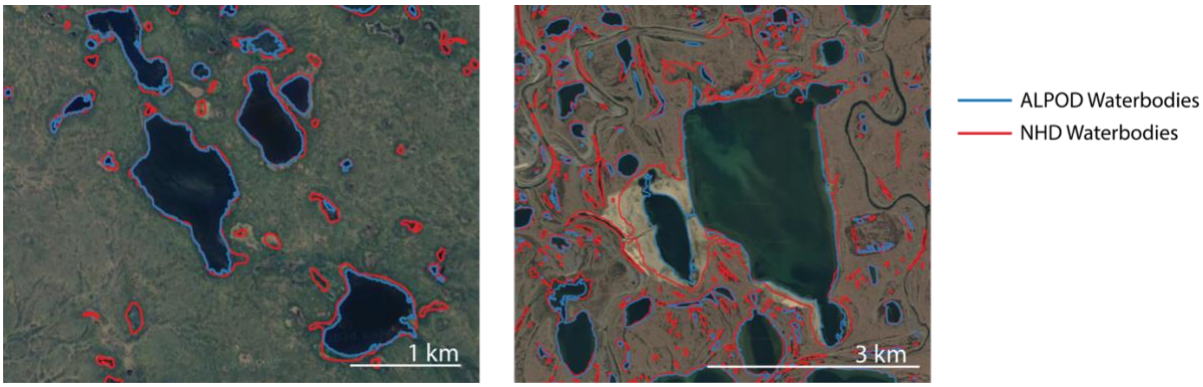

Figure A4: Visual comparison of ALPOD lake and ponds and the NHD water bodies. ALPOD boundaries are the result of open water occurrence for images across 6 ice-free seasons, whereas NHD boundaries are from static imagery sources. The timing of the acquisition of these images varies across Alaska, ranging from 2001-2023 and including some ice-covered dates.

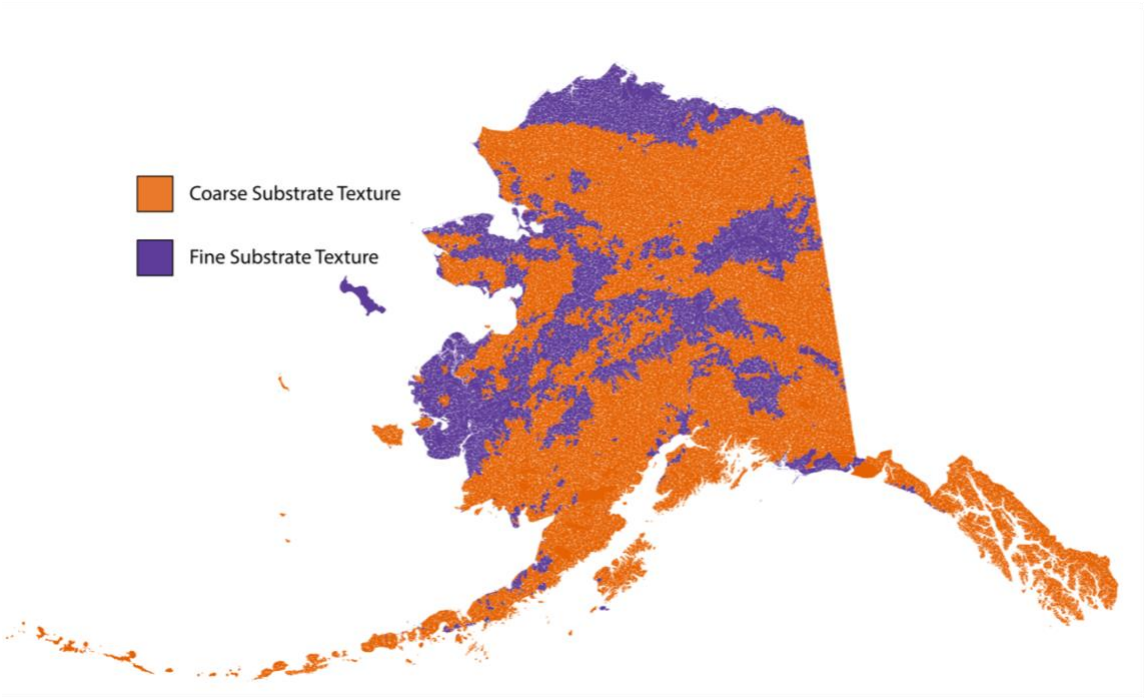

Figure A5: The map of substrate texture across AK based on Jorgsensen et al., 2008. Coarse substrate is from their 'rocky' classification, and fine substrate is a combination of sandy and silty textures.

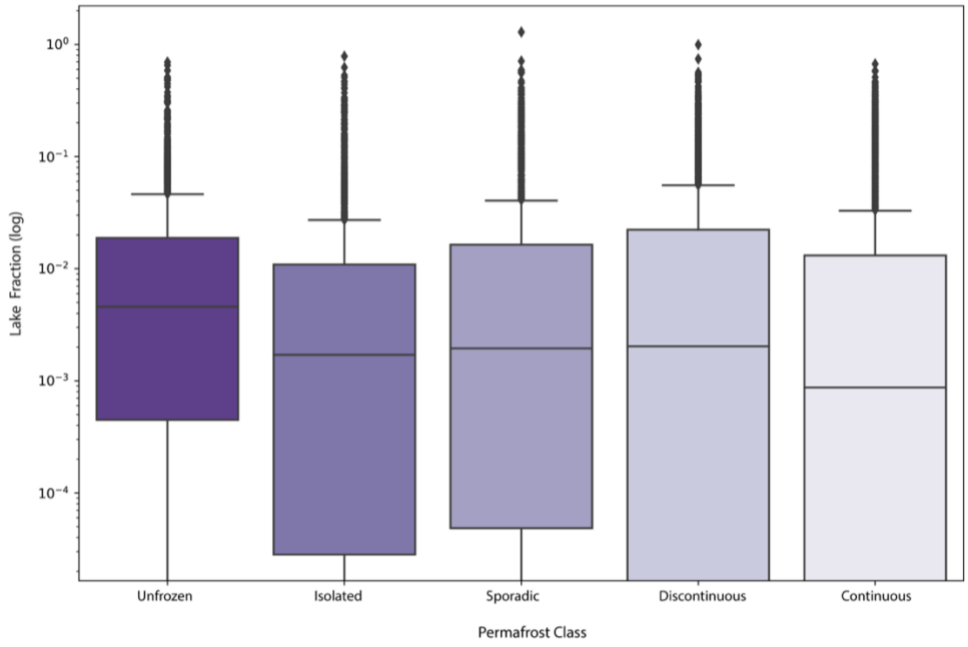

Figure A6: Lake fraction of watersheds differentiated by permafrost class.

Terrain Classification	Permafrost Extent	Land Area (km^2)	Number of Lakes	Lake Area (km^2)	Lake Density (lakes per 100 km^2)	Lake Fraction (%)	Mean Lake Size (km^2)
Unglaciated - Fine	Unfrozen	3399.49	1322	59.35	38.89	1.75	0.04
	Isolated	30872.45	17554	468.75	56.86	1.52	0.03
	Sporadic	125681.03	209153	7817.27	166.42	6.22	0.04
	Discontinuous	156764.62	225170	11090.66	143.64	7.07	0.05
	Continuous	117822.02	136762	10432.71	116.08	8.85	0.08
	Total	434539.61	589961	29868.74	135.77	6.87	0.05
Unglaciated - Coarse	Unfrozen	10141.57	3295	327.79	32.49	3.23	0.10
	Isolated	48048.35	6600	256.55	13.74	0.53	0.04
	Sporadic	127363.73	19007	575.43	14.92	0.45	0.03
	Discontinuous	117761.02	16861	764.13	14.32	0.65	0.05
	Continuous	131416.31	14472	510.35	11.01	0.39	0.04
	Total	434730.98	60235	2434.26	13.86	0.56	0.04
Postglacial - Fine	Unfrozen	31619.66	18057	1027.69	57.11	3.25	0.06
	Isolated	17614.52	11788	596.64	66.92	3.39	0.05
	Sporadic	17485.37	10977	348.18	62.78	1.99	0.03
	Discontinuous	6101.25	4781	185.95	78.36	3.05	0.04
	Continuous	4131.39	3409	169.05	82.51	4.09	0.05
	Total	76952.19	49012	2327.51	63.69	3.02	0.05
Postglacial - Coarse	Unfrozen	259191.09	53454	10587.91	20.62	4.08	0.20
	Isolated	97717.35	26248	2218.96	26.86	2.27	0.08
	Sporadic	48891.43	10101	327.70	20.66	0.67	0.03
	Discontinuous	48440.33	4561	338.43	9.42	0.70	0.07
	Continuous	105586.61	8323	423.23	7.88	0.40	0.05
	Total	559826.81	102687	13896.23	18.34	2.48	0.14

Table A3: Basic lake statistics across our physiographic and permafrost classes.

Permafrost Extent	Land Area (km^2)	Number of Lakes	Lake Area (km^2)	Lake Density (lakes per 100 km^2)	Lake Fraction (%)	Mean Lake Size (km^2)
Unfrozen	306733.58	76128.00	12002.75	24.82	3.91	0.16
Isolated	194279.97	62190.00	3540.91	32.01	1.82	0.06
Sporadic	319447.56	249238.00	9068.58	78.02	2.84	0.04
Discontinuous	329427.82	251373.00	12379.16	76.31	3.76	0.05
Continuous	358962.53	162966.00	11535.34	45.40	3.21	0.07
Total	1508851.45	801895.00	48526.74	53.15	3.22	0.06

Table A4: Lake statistics differentiated by permafrost class.

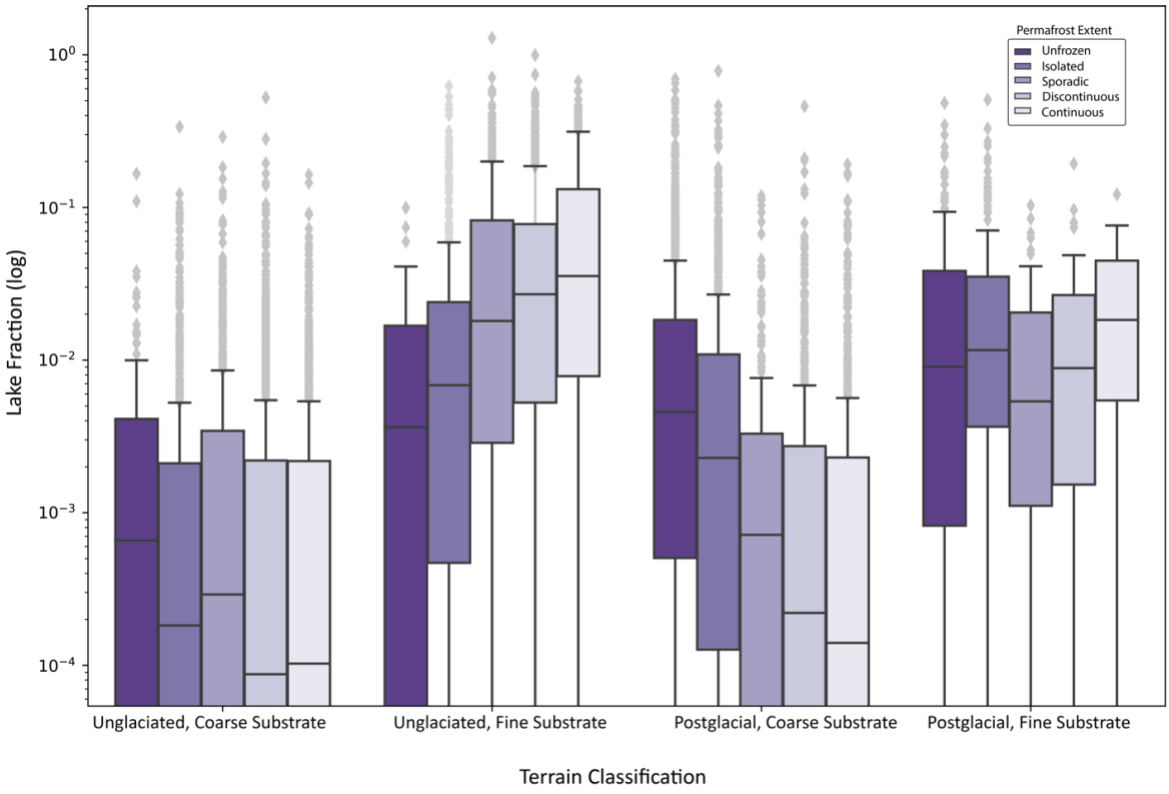

Figure A7: Comparison of the relationship between lake fraction and permafrost extent within distinct physiographic settings.

Glacial History	Substrate Texture	Z Score	p-value	Alternative Hypothesis
Unglaciated	Fine	14.727	< 2.2e-16	increasing lake fraction with permafrost extent
Unglaciated	Coarse	-3.5	0.0003992	decreasing lake fraction with permafrost extent
Postglacial	Fine	-0.07559	0.9397	N/A
Postglacial	Coarse	-24.177	< 2.2e-16	decreasing lake fraction with permafrost extent
Postglacial		-23.897	< 2.2e-16	decreasing lake fraction with permafrost extent
Unglaciated		7.3993	1.37E-13	increasing lake fraction with permafrost extent

Table A5: Results of Cuzick's Tests for Trend between permafrost extent and lake fraction. The null hypothesis is that there is no significant trend in increasing or decreasing lake fraction across groups ordered by permafrost extent.

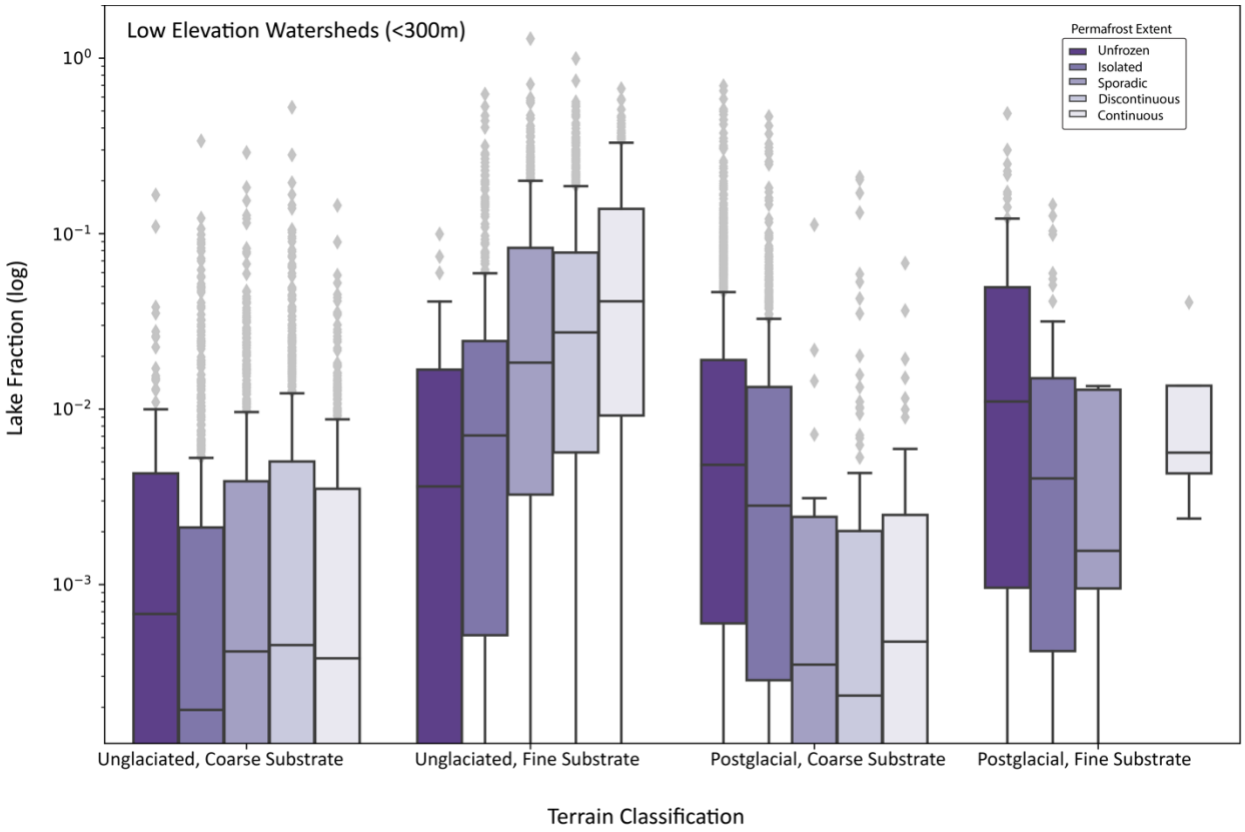

Figure A8: Same comparison as Figure A7, but for low-elevation watersheds (<300 m).

Glacial History	Substrate Texture	Z Score	p-value	Alternative Hypothesis
Unglaciated	Fine	15.31	< 2.2e-16	increasing lake fraction with permafrost extent
Unglaciated	Coarse	2.0595	0.03944	N/A
Postglacial	Fine	-2.5229	0.01164	N/A
Postglacial	Coarse	-10.14	< 2.2e-16	decreasing lake fraction with permafrost extent
Unglaciated		19.08	< 2.2e-16	increasing lake fraction with permafrost extent
Postglacial		-10.154	< 2.2e-16	decreasing lake fraction with permafrost extent

Table A6: Results of Cuzick's Tests for Trend between permafrost extent and lake fraction in low elevation watersheds (<300m). The null hypothesis is that there is no significant trend in increasing or decreasing lake fraction across groups ordered by permafrost extent.

Glacial History	Substrate Texture	Z Score	p-value	Alternative Hypothesis
Unglaciated	Fine	19.147	< 2.2e-16	increasing mean lake size with pf extent
Unglaciated	Coarse	6.2313	4.63E-10	increasing mean lake size with pf extent
Postglacial	Fine	-14.083	< 2.2e-16	decreasing mean lake size with pf extent
Postglacial	Coarse	-2.3822	0.01721	decreasing mean lake size with pf extent
Low Elevation				
Unglaciated	Fine	19.191	< 2.2e-16	increasing mean lake size with pf extent
Unglaciated	Coarse	5.1842	2.17E-07	increasing mean lake size with pf extent
Postglacial	Fine	-2.1417	0.03222	
Postglacial	Coarse	-9.2479	< 2.2e-16	decreasing mean lake size with pf extent

Table A7: Results of Cuzick's Tests for Trend between permafrost extent and mean lake size. The null hypothesis is that there is no significant trend in increasing or decreasing mean lake size across groups ordered by permafrost extent. 'pf' refers to permafrost.

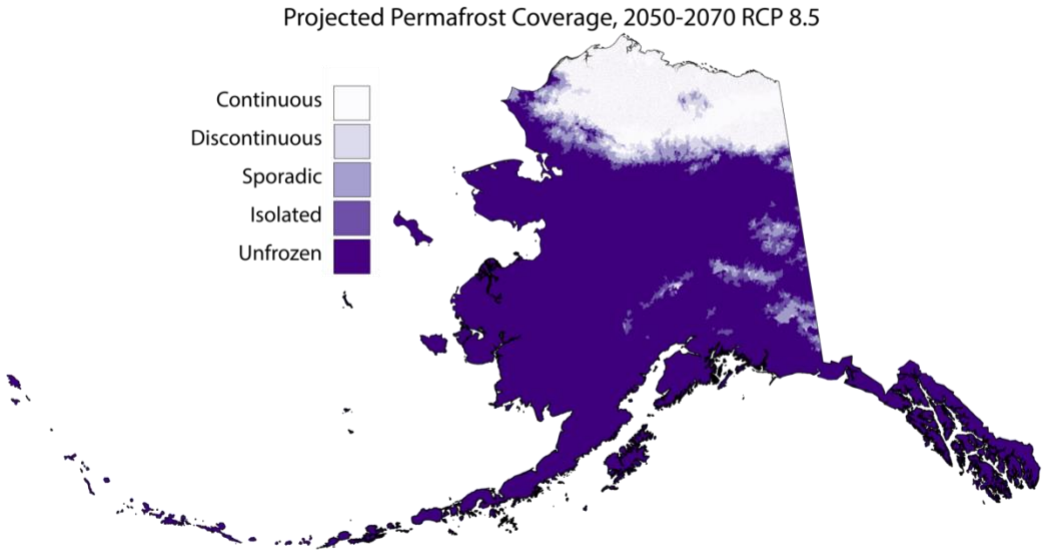

Figure A9: Projected permafrost coverage by Karjalainen et al., 2019 for RCP 8.5. RCPS 2.6 and 4.5 show very similar patterns but with slightly reduced permafrost in central AK.

Metric	Time Scale
Lake Area Metrics	
Mean	Overall, Annual, Seasonal
Median	Overall, Annual, Seasonal
Std	Overall, Annual, Seasonal
Range	Overall, Annual, Seasonal
IQR	Overall, Annual, Seasonal
Maximum	Overall, Annual, Seasonal
Minimum	Overall, Annual, Seasonal
Coefficient of Variation	Overall, Annual, Seasonal
Seasonality Index	Seasonal
Timing Metrics	
Maximum Lake Area	Annual, Seasonal
Snow Disappearance	Annual, Seasonal
Ice Breakup	Annual, Seasonal

Table A8: Lake area time series summary statistics calculated for each individual basin. Overall metrics use the entire filtered nine-year time series. Annual metrics are calculated for individual years (2017-2025). Seasonal metrics are calculated as a basin's average of the annual statistics.

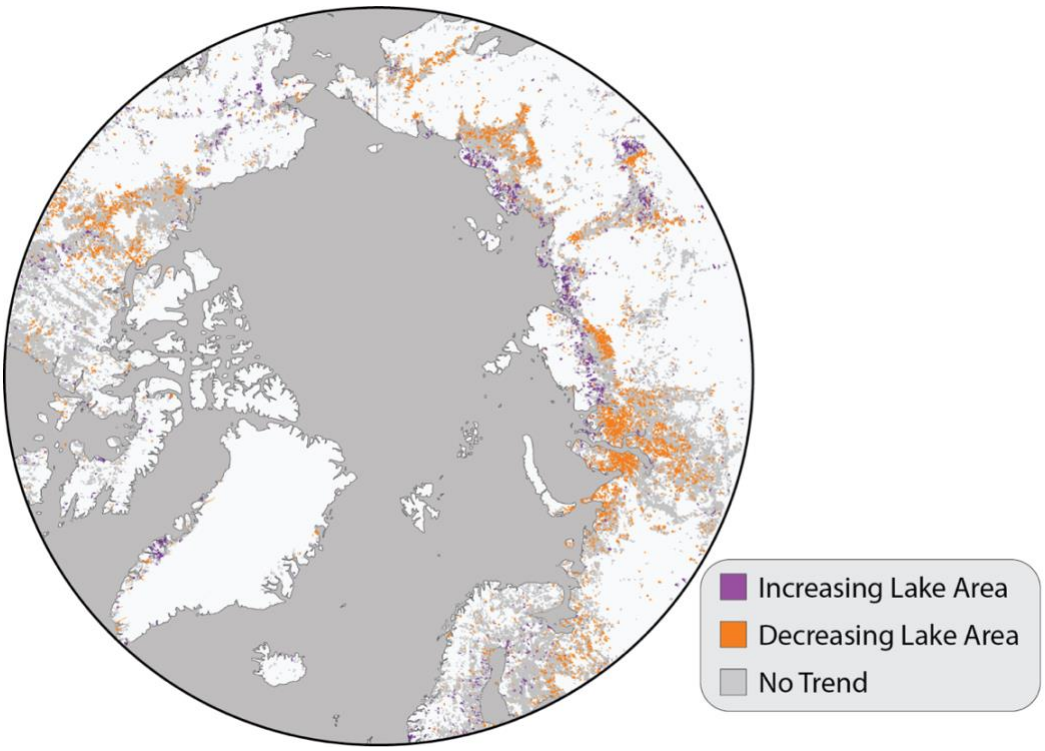

Figure A10: Interannual trends for basins that meet analysis requirements. Orange indicates declining lake area, while purple indicates increasing lake area. Gray shows basins without significant trends.

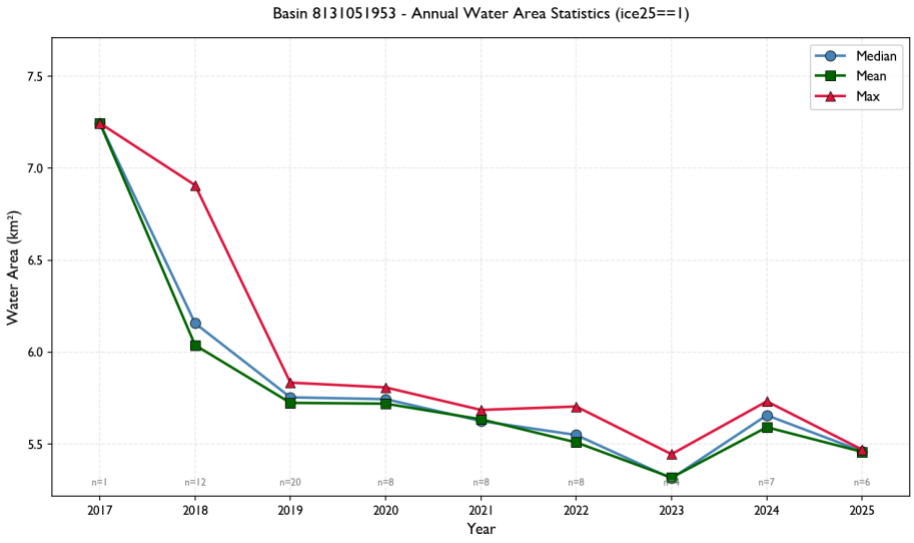

Figure A11: Example time series of a previously documented 2018 lake drainage event on Seward Peninsula, AK (Nitze et al., 2020).

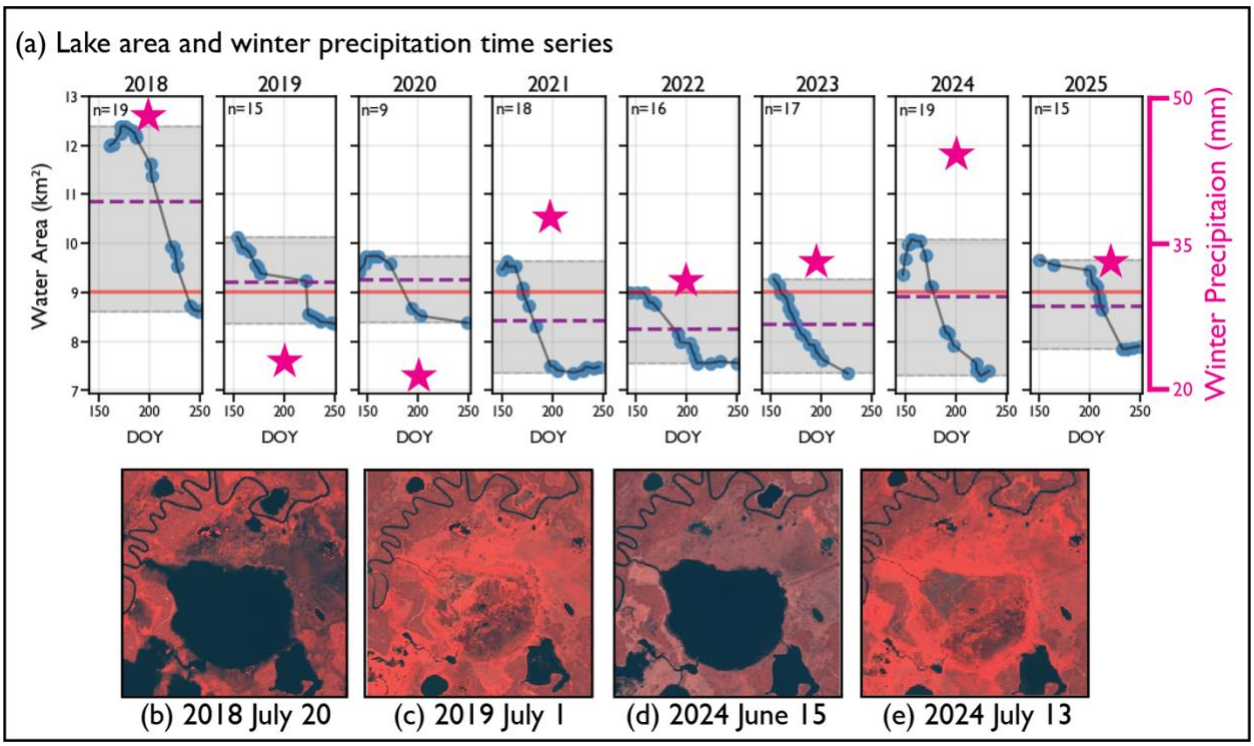

Figure A12: Example time series and imagery of a drained lake basin and nearby ephemeral lakes that can fill and drain seasonally. Winter precipitation values are calculated from ERA5 reanalysis data.

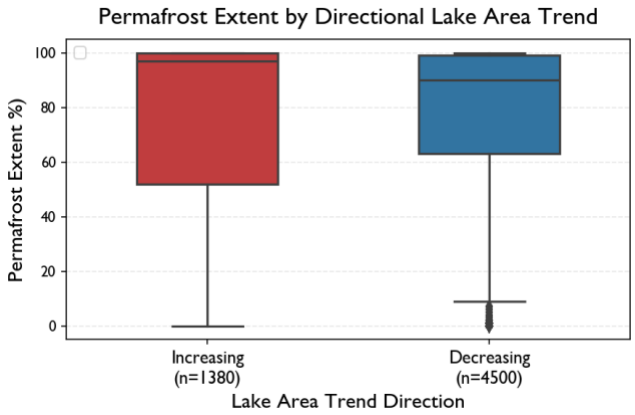

Figure A13: Boxplot comparing the distribution of permafrost extent of basins with significantly increasing or decreasing trends. According to our Mann-Whitney U-Test, mean permafrost extent of decreasing trends is lower than the mean permafrost extent of increasing trends ($p < 0.001$).

Variable	Description	Coefficient	|Coefficient|
pop_ct_usu	Upstream Population Count	0.00787325	0.00787325
snd_pc_sav	Sand %	-0.007045	0.00704501
slt_pc_sav	Silt %	0.00618104	0.00618104
prm_pc_sse	Permafrost %	-0.0059572	0.0059572
ria_ha_ssu	River Area	0.00542178	0.00542178
rev_mc_usu	Reservoir Volume	-0.0044453	0.00444527
ero_kh_sav	Soil Erosion	0.00357464	0.00357464
ari_ix_sav	Aridity Index	0.00285722	0.00285722
ele_mt_sav	Elevation	-0.0026268	0.00262682
riv_tc_ssu	River Volume	-0.0024839	0.00248387
dis_m3_pmn	Natural Discharge (minimum)	0.00172129	0.00172129
gla_pc_sse	Glacier Extent	0.00168689	0.00168689
dis_m3_pyr	Annual Discharge	0.00159574	0.00159574
lit_cl_smj	Lithology Class	-0.0015627	0.0015627
for_pc_sse	Forest Coverage	-0.0015006	0.00150056
riv_tc_usu	River Volume (Upstream)	-0.0013637	0.00136369
pnv_pc_s08	Potential Natural Vegetation (August)	0.00100844	0.00100844
*PET_sum	ERA5 P-ET (summer)	-0.0009976	0.00099761
pac_pc_use	Protected Area % (Upstream)	0.00088172	0.00088172
ero_kh_uav	Soil Erosion (Upstream)	-0.0008679	0.00086792
run_mm_syr	Annual Runoff	0.0007538	0.0007538
hdi_ix_sav	Human Development Index	-0.0005631	0.00056313
pst_pc_sse	Pasture Extent	0.00038418	0.00038418
gwt_cm_sav	Groundwater Table Depth	-0.0002399	0.00023992
ire_pc_use	Irrigation % (Upstream)	0.00022793	0.00022793
pac_pc_sse	Protected Area %	0.00016241	0.00016241
dor_pc_pva	Degree of Regulation	0.00014988	0.00014988
ele_mt_smx	Elevation (minimum)	0.00012884	0.00012884

rdd_mk_uav	Road Density Upstream	-0.0001112	0.00011118
snd_pc_uav	Sand % (Upstream)	0.00010717	0.00010717
urb_pc_sse	Urban %	-0.0001024	0.0001024
dis_m3_pmx	Discharge (minimum)	8.19E-05	8.19E-05
pop_ct_ssu	Population Count	-7.01E-06	7.01E-06
*PET_win	ERA5 P-ET Winter	0	0
y	Latitude	0	0
ppd_pk_sav		0	0
lkv_mc_usu		0	0
urb_pc_use	Urban % (Upstream)	0	0
*PET_spr	ERA5 P-ET Spring	0	0
ppd_pk_uav	Upstream Population Density	0	0
gla_pc_use	Glacier Percent (Upstream)	0	0
ria_ha_usu	River Area (Upstream)	0	0
kar_pc_use	Karst % (Upstream)	0	0
kar_pc_sse	Karst %	0	0
ele_mt_uav	Elevation (Upstream)	0	0
slt_pc_uav	Silt % (Upstream)	0	0
cly_pc_uav	Clay % (Upstream)	0	0
cly_pc_sav	Clay %	0	0
ari_ix_uav	Upstream Aridity	0	0
pst_pc_use	Pasture Extent (Upstream)	0	0
ire_pc_sse	Irrigated Area	0	0
UP_AREA	Upstream Area	0	0

Table A9: Predictors and their coefficients for the LASSO regression modeling basins' lake seasonality index.

Year	Mean Discharge
2017	214980.3
2018	255878.1
2019	235683
2020	292994.8
2021	257772.1
2022	285966.8
2023	289406.8
2024	275948.4
2025	308124.4

Table A10: Annual mean discharge measured at Pilot Station, Yukon River (USGS Site No. 15565447. OLS Linear Regression results show a significant increase in mean discharge over the study period (p-value = 0.016)

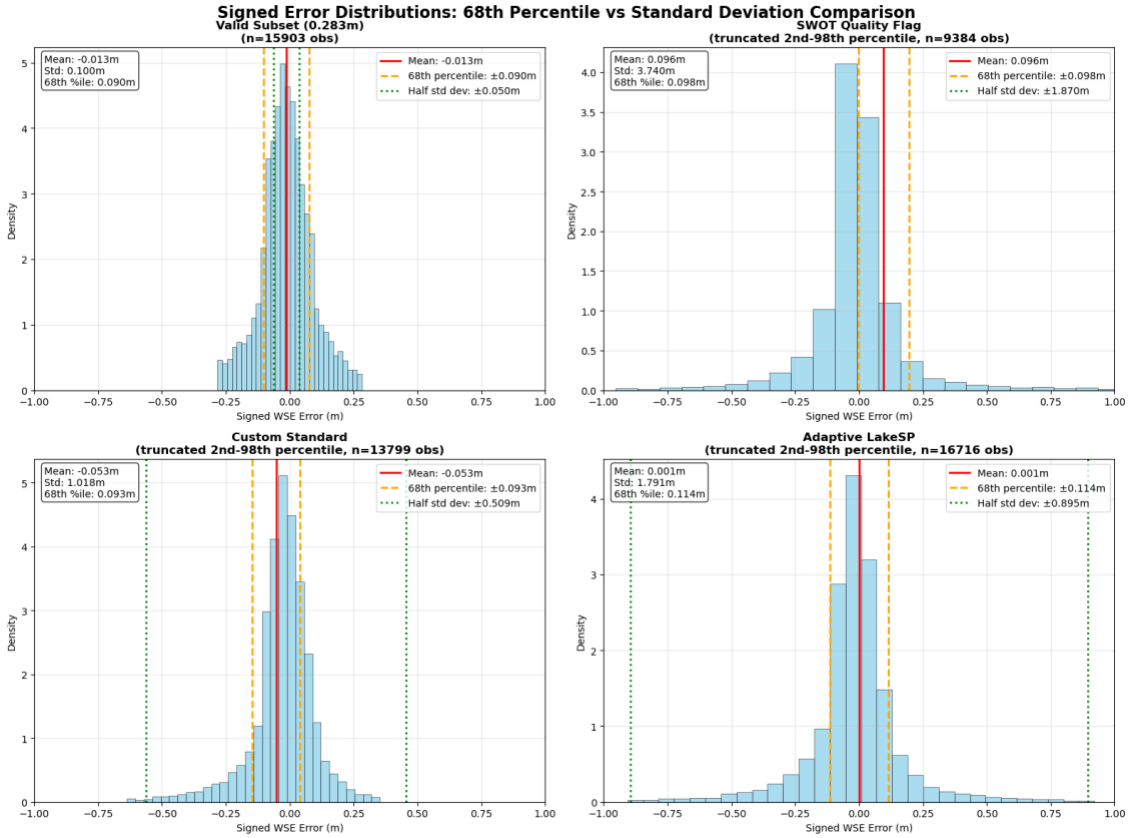

Figure A13: Histograms of WSE errors for each filter.

Data Source	Observations	Lakes	Retention Rate	Bias (km^2)	MAE (km^2)	RMSE (km^2)	P68 (km^2)	Bias (%)	MAE (%)	RMSE (%)	P68 (%)
Static (PLD)	5358	183	62.462	-1.213	2.339	5.662	1.453	-9.851	37.491	70.055	38.098
Sentinel-2	18766	181	18.403	-0.016	0.302	0.876	0.186	0.184	3.819	6.129	3.592
SWOT (Idealized)	1715	112	19.993	-0.144	1.237	2.531	0.884	-0.36	20.163	47.284	16.965
SWOT (Quality Flag)	2839	171	33.096	0.02	1.223	2.838	0.777	1.976	17.608	34.328	14.21
SWOT (Simple)	3985	175	46.456	-0.227	1.185	2.76	0.752	-1.3	18.291	33.849	16.025
SWOT (Adaptive)	4678	179	54.535	-0.051	1.308	3.239	0.824	4.321	25.9	63.18	19.514

Table A11: WSA error metrics by sensor.